Experimental Investigation of Oscillating-Foil Technologies

by

Dylan Iverson
B.Eng., University of Victoria, 2015

A Thesis Submitted in Partial Fulfillment of the
Requirements for the Degree of

Master of Applied Science

in the Department of Mechanical Engineering

Experimental Investigation of Oscillating-Foil Technologies

by

Dylan Iverson
B.Eng., University of Victoria, 2015

Supervisory Committee

Dr. Peter Oshkai, Co-Supervisor
Department of Mechanical Engineering

Dr. Guy Dumas, Co-Supervisor
Department of Mechanical Engineering, Laval University

Supervisory Committee

Dr. Peter Oshkai, Co-Supervisor
Department of Mechanical Engineering

Dr. Guy Dumas, Co-Supervisor
Department of Mechanical Engineering, Laval University

ABSTRACT

This thesis contains an experimental campaign on the practical implementation of oscillating-foil technologies. It explores two possible engineering applications of oscillating-wings: thrust-generation, and energy-extraction. The history of, benefits of, and difficulties involved in the use of oscillating-foils is discussed throughout.

Many existing technologies used for thrust generation and hydrokinetic energy extraction are based on rotating blades or foils, which have evolved over decades of use. In recent years, designs that use oscillating-foils, with motions analogous to the flapping of a fish's tail or a bird's wing, have shown increased hydrodynamic performance compared to the traditional rotary technologies. However, these systems are complex, both in terms of the governing unsteady fluid dynamics, and the methods by which kinematics are prescribed. Simply put, system complexity and cost need to be reduced before these devices see wide-spread use.

For this reason, the work contained within this thesis explores possible methods of reducing the complexity of oscillating-foil systems in an effort to contribute to their development. For thrust-generation applications, this entailed using flexible foils to create passive pitching kinematics. This was parametrically studied by testing foils of different structural properties under a range of kinematics. The results suggested that properly tuning the flexibility of the foil could enhance both the thrust generation, and the efficiency of the propulsive system.

With respect to energy-harvesting applications, the reliability of a novel fully-passive turbine was assessed. The prototype tested had no active control strategy, and the degrees-of-freedom were not mechanically linked, greatly simplifying the design.

The prototype was subjected to real-world conditions, including high turbulence levels and the wake of an upstream turbine, and displayed robust performance in most conditions.

In both applications, the hydrodynamic performance of the oscillating-wings was directly measured, and particle image velocimetry was used to observe the flow topology in the wakes and boundary layers of the foils. The vortex and stall dynamics were highlighted as key flow features, and are studied in detail.

Contents

List of Tables

List of Figures

ACKNOWLEDGEMENTS

Of the many people who have helped me, I would like to thank:

Dr. Peter Oshkai, whose guidance and knowledge made this research a rewarding and successful experience. Your mentorship extended beyond academic pursuits, leading to inspiring thoughts about the everyday.

Dr. Guy Dumas, for graciously sharing your passion and expertise, creating genuine enthusiasm in this research endeavour.

Dr. Boualem Khouider, for kindly offering your time and expertise as an examiner in the thesis defence.

Matthieu Boudreau, Mostafa Rahimpour, and Majid Soleimani nia, for always offering your time and experience to train and guide a junior student. You provided insights I could not have received from any other sources, and the sincerity by which you did so is gratefully acknowledged.

My parents, Susan and Eric, for without your support, encouragement, and kindness, this journey would not have been possible.

Marcelina Lassak, for the motivation to pursue this education, to continually better myself, and for support and patience throughout.

And lastly, the Lads, for the many humbling questions, inspiring conversations, and memories along the way.

Chapter 1

Introduction

1.1 Context

Nature uses oscillating-wings. This simple statement possesses depth beyond the initial thought. The answer to why this natural solution exists requires an interdisciplinary understanding. Indeed, biologists question why evolution converged on oscillating-wings [1], engineers ask how they can replicate the elegance of organic motion [2], and fluid dynamicists strive to understand the unsteady phenomena resulting from these motions [3]. Is the use of flapping-wings the result of biological limitations, or is it truly an optimized solution to complex problems? Perhaps the most relevant question, from this author's perspective, is how can technologies be designed off these principles to benefit society?

In the current context, the terms oscillating-foils, or flapping-wings[1], refer to streamlined bodies that move in combined translating and rotating motions; doing so in a periodic and cyclic manner. Commonly recognized examples include the flapping of a bird's wings in flight [4], and the undulations of a fish's tail [5]. Less-recognizable than these examples of oscillating-wings that add energy to the surrounding fluid, is the tendency for structures to oscillate and remove energy from a fluid, an event which is perhaps equally common. Leaves rustle in the wind [6], a plane's wings may flutter [7], and bridges can gallop under certain circumstances [8]. In such instances, the fluid can transfer energy to the structure. If the energy imparted on the structure is not removed at sufficient levels, the motion amplitudes may grow unbounded, and

[1]The terms wing and foil, as well as oscillating and flapping, are used interchangeably throughout this writing. The same ambiguity applies to the terms aerodynamic and hydrodynamic, where the technologies in question are applicable to both gas and liquid environments.

results can be catastrophic. Researchers in recent years have, however, realized the potential for energy extraction from these oscillating systems.

In either application, whether the wings add energy to the flow or extract it, this fluid-structure interaction shows promise in exceeding the performance of comparative rotary technologies used to achieve the same goals. The oscillating-foil systems benefit from unsteady flow features that can generate high instantaneous forces. However, these same flow features can be fundamentally complex to model and are dependent upon many parameters. While early efforts to provide insight into the unsteady aerodynamics can be traced back to at least the works of Garrick [9] and Theodorson [10], no generalized analytical solutions currently exist. Rather, the state of the art has been developed incrementally, through combinations of theoretical, numerical, and experimental studies. These difficulties in modelling the hydrodynamic forces on oscillating bodies, in combination with the complexity in designing the mechanical systems used to achieve desirable kinematics, have hampered the development of many practical efforts.

The present work provides an overview of an engineering perspective on the use and exploitation of oscillating-foils. Distinct applications of propulsion and energy-extraction are studied, although in principle they rely on similar operation fundamentals. Chapter 2 reviews a brief history of oscillating-foil propulsion devices, and progresses to the enclosed study on the effect of foil flexibility on the propulsive characteristics of moderate scale oscillating thrust generators. Chapter 4 contains an experimental study assessing the reliability of a novel, fully-passive oscillating-foil hydrokinetic turbine. The evolution of the state of the art leading to the motivation for the so-called fully-passive design is reviewed in detail. But before this is completed, Chapter 3 provides a fidelity assessment of the experimental methods used in the hydrokinetic turbine campaign.

The thesis is structured as a compilation of paper drafts intended to be submitted for archival journal publication. Each of Chapters 2, 3, and 4 are written as stand-alone papers. Some modifications, such a formatting changes, have been implemented for consistency throughout this thesis.

1.2 Propulsion vs. energy-extraction regimes

While the full theory appropriate to the individual applications of oscillating-foil propulsion and energy-extraction is presented in the relevant chapters, it is worthwhile

to explicitly demarcate the two subjects here. The unifying similarity across the two oscillating-foil applications is the synchronous heaving (translating) and pitching (rotating) motions of the streamlined body[2]. However, the trajectory of the foil through the fluid medium differs between the two regimes.

In a general oscillating-foil case, assuming sinusoidal motion profiles in each degree-of-freedom, the equations of heave ($h(t)$) and pitch ($\theta(t)$) positions are provided in 1.1 and 1.2.

$$h(t) = H_0 \sin(\gamma t + \phi) \tag{1.1}$$

$$\theta(t) = \theta_0 \sin(\gamma t) \tag{1.2}$$

Here, H_0 is the heave amplitude, θ_0 is the pitch amplitude, γ is the angular frequency of both motions, ϕ is the phase difference between profiles, and t is time.

Strictly speaking, sinusoidal motion profiles applied to the individual motion profiles do not guarantee optimal performance, nor are they necessarily the standard motions observed in nature. However, for the purposes of the current conceptual analysis sinusoidal pitch and heave profiles are considered. It is often argued that the effective angle of attack (α) that the foil experiences as a result of the combined heave motion, pitch motion, and freestream velocity (U_∞), is the more fundamental parameter, and prescribing its evolution throughout a cycle may be more beneficial. The effective angle of attack is defined by Equation 1.3, as:

$$\alpha(t) = \arctan[-\dot{h}(t)/U_\infty] - \theta(t)\,, \tag{1.3}$$

where the superscript ($\dot{}$) signifies terms differentiated with respect to time, t.

Kinsey and Dumas [11] proposed that propulsion and energy-extraction regimes could be delimited by a feathering parameter, χ, defined in Equation 1.4.

$$\chi = \frac{\theta_0}{\arctan(H_0\gamma/U_\infty)} \tag{1.4}$$

This quasi-static parameter provides a metric for the foil's motion relative to its path

[2]Some propulsion technologies exist where either only heave or only pitch motions are used, but the same oscillatory principles remain.

through the fluid, in a cycle-averaged sense. An example of generic kinematics for each regime are illustrated in Fig. 1.1. The schematic also shows typical force vectors resulting from the interaction with the fluid. The total resultant force on the foil, R, is the summation of either the streamwise force component (X) and the lateral component (Y), or the lift force (L) and the drag force (D), both of which are pairs of orthogonal vectors.

At a value $\chi = 1$, which is referred to as the feathering limit, the foil maintains a near-zero effective angle of attack throughout a motion cycle and acts as neither a propulsor or a turbine. While a true 0° angle of attack is only guaranteed to occur every quarter-period in a cycle if sinusoidal pitch and heave motions are used, corresponding to the phases shown in Fig. 1.1, lift forces on the foil elsewhere in the cycle are small.

The foil acts as a thrust generator when $\chi < 1$. Here, the foil is oriented with respect to its trajectory through the fluid in a manner that the resultant force opposes the foil's heave motion. Energy must therefore be put into the system to drive the motion. Provided a suitable foil shape and a reasonable pitch amplitude, this results in a thrust force that propels the foil. Conservation of momentum requires that this thrust exerted on the foil be balanced by a momentum transfer to the fluid, which produces a time-averaged wake similar to that shown on the right of Fig. 1.1. While the wake has a simple jet structure in a time-averaged sense, the instantaneous dynamics are more complicated. Instabilities in the shear layer of the wake allow vorticity shed from the foil to concentrate, resulting in a reverse von Kármán vortex street comprised of counter-rotating vortices [12].

When $\chi > 1$ the foil functions as an energy-harvester. The lateral component of generated force aids the motion of the foil, which may be used to provide useful power take-off. The streamwise component of the generated force does no work on the foil, as the turbines is not free to move in the x-direction.

The high pitch amplitudes involved in energy-extraction applications results in robust stall dynamics. The flow may be roughly categorized into motions that develop deep dynamic stall [13], which produce a large leading edge vortex that convects into the wake, and motions where the boundary layer remains attached to the foil throughout a cycle. In the latter, the shear layer from the foil rolls-up into a von Kármán vortex street; a wake signature inverse from that in the propulsion regime. Contrary to propulsion applications, this leaves a momentum deficit in the flow.

While this quasi-static approach supplied by the feathering parameter is valuable

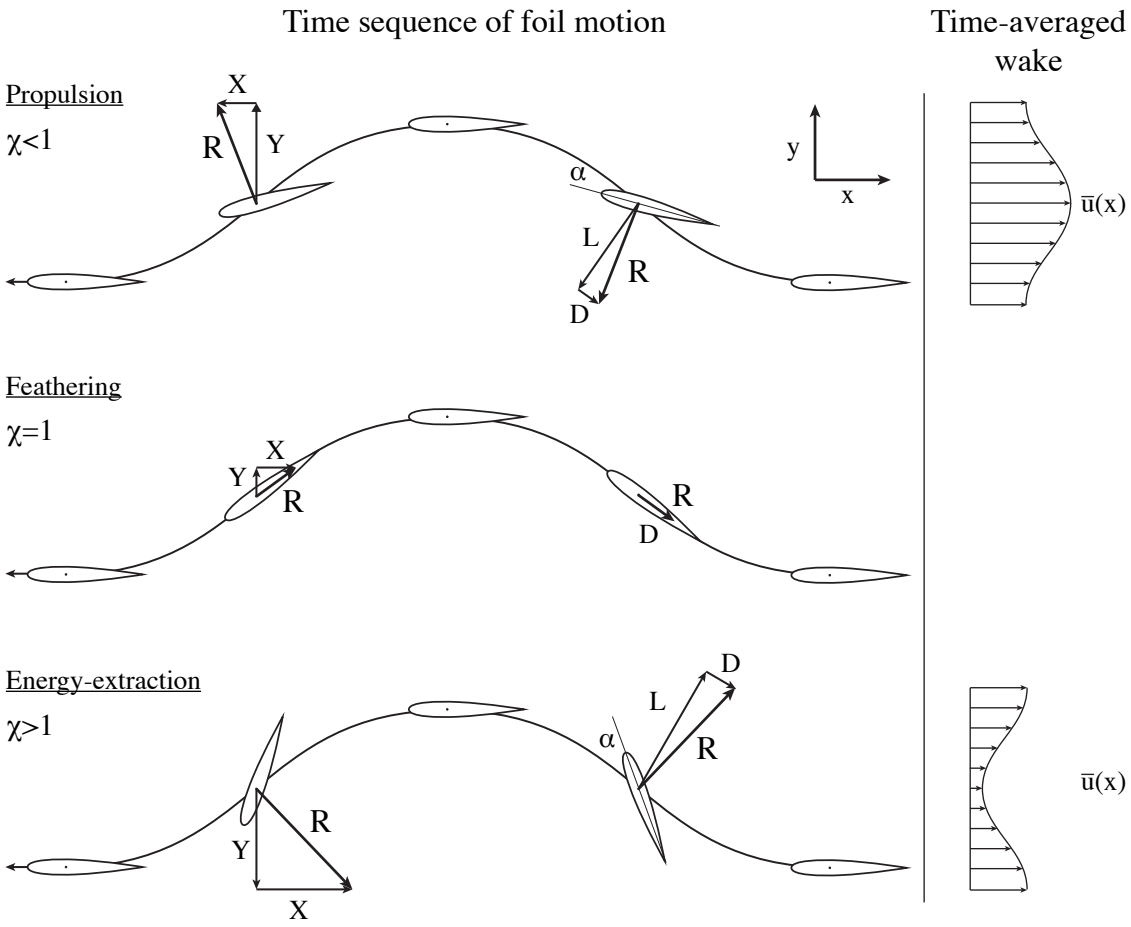

Figure 1.1: Force orientations and time-averaged wakes for generic propulsion and energy-extraction kinematics. The trajectory of the foil, travelling from right to left, is shown from a reference frame fixed to the undisturbed freestream. Adapted from [11].

in delimiting the regime of operation, it does not provide insight into the performance of the system. Other variables, such as the amplitudes of motion, the location of the pitch axis, the rate of pitching, the foil shape, the Reynolds number, and the wake history, to name a few, can be highly influential on system performance. While one of the advantages of oscillating-foil systems is the unsteady fluid-structure interaction, resulting in high instantaneous forces, this same fact causes great difficulty in predicting and understanding the performance of these systems.

1.2.1 Dimensional analysis

The chord-based Reynolds number, defined in Equation 1.5, is applied to both propulsion and energy-extraction regimes. This fundamental relation can have a large impact on the boundary layer dynamics of both systems, discussed at length in Chapter 3.

$$Re_c = \frac{U_\infty c}{\nu} \tag{1.5}$$

Here, c is the chord length of the foil, and ν is the kinematic viscosity of the fluid.

The oscillation frequency, $f = \gamma/2\pi$, is an important governing parameter in the operation of all oscillating-foils, but is non-dimensionalized differently for propulsion and energy-extraction regimes. For propulsive cases, the Strouhal number, St, is used, as defined in Equation 1.6.

$$St = \frac{fA}{U_\infty} \tag{1.6}$$

The wake width, A, which corresponds to the full extent of the heave motion, is used as the characteristic length scale. The Strouhal number provides suitable scaling for propulsive cases, where it has been observed that the oscillation frequency for fins and tails in nature nearly universally collapse into a range of Strouhal numbers between $0.2 < St < 0.4$ [14], [15]. At these frequencies the oscillating-foil applies periodic disturbances to the fluid corresponding to dominant frequency of the most unstable mode of the wake, leading to an amplification of unsteady forces [16].

Although the Strouhal number could also be applied to energy-extraction applications, better scaling has been found with the reduced frequency, f^*, defined in Equation 1.7.

$$f^* = \frac{fc}{U_\infty} \tag{1.7}$$

Here, the the chord length of the foil is used as the characteristic length scale. Research by Simpson [17] found that similitude in vortex modes and efficiency for energy-extraction was possible with the use of reduced frequency, but this scaling failed when the Strouhal number was used. It has become standard in the context of energy-extraction applications to therefore use the reduced frequency.

The performance of each regime is also assessed slightly differently. The definition

of efficiency for each operation regime is provided in Equations 1.8 and 1.9.

$$\text{Propulsion :} \qquad \eta_{\text{prop}} = \frac{\overline{C_T}}{\overline{C_P}} = \frac{\text{Thrust x Velocity}}{\text{Power input}} \tag{1.8}$$

$$\text{Energy-extraction :} \qquad \eta_{\text{extract}} = \frac{\overline{P}}{P_a} = \frac{\text{Power output}}{\text{Power available}} \tag{1.9}$$

For propulsion systems, efficiency is defined as generated thrustand velocity relative to the power input to the system. Further definitions are provided in Section 2.1.1. For energy-extraction systems, efficiency is defined as the power extracted by the system relative to the hydrokinetic energy flux through the swept area of the turbine. Further details are provided in Section 3.1.2. In either case, the efficiency provides an assessment of how well the system performs its function. Because the quantities used in the efficiency definitions vary over an oscillation-cycle, they are commonly presented as cycle-averaged values, denoted by an overbar ($\bar{}$).

1.3 Motivation

The present work is motivated by the desire to reduce the system complexity of oscillating-foil technologies in an effort to contribute to the development and practicality of these devices, and to increase the understanding of the unsteady fluid dynamics governing system performance. In both operation regimes, the hydrodynamic performance of oscillating-foils has been sufficiently proven; turbines have been designed to extract up to 43% of the available energy [18], and oscillating propulsors have exceeded the efficiencies of traditional rotary propellers [2]. Yet wide-scale adoption outside of academia has been low and largely unsuccessful. It is reasonable to partially attribute this to the complexities and inefficiencies involved in prescribing suitable heave and pitch kinematics to the system, as well as the fundamental difficulties associated with understanding the unsteady fluid-structure interactions.

It can be argued that the success of oscillating-foil technologies must be assessed from a systems standpoint [1]. As a practical example of how mechanical complexities may overwhelm the benefits of increases in hydrodynamic performance, it is useful to consider the results of an experimental campaign by Kinsey et al. [19], who developed and tested a dual oscillating-foil turbine. In the design of the prototype, the heave and pitch motions were coupled by mechanical means to achieve the desired synchronization. A duplicated four-bar mechanism was also used to convert the heave

motion of the foils to a rotational motion suitable for power take-off. As a result of these mechanical complexities, mechanical losses involved in the system were on the order of 25% of the total power extracted. These mechanical complexities also lead to increased maintenance and lower reliability. It is noted that while the intent of this study was to test the concept in a real-world environment, and not to design an optimal mechanical system, the results are representative of other designed systems and are somewhat sobering.

While a general analysis of system dynamics is not the focus of the current work, this realization motivates two of the enclosed studies. The parametric study in Chapter 2 explores the concept of using passive foil flexibility to replicate actively prescribed pitching motions. The results show that by properly designing the structural parameters of the foil, the need for actively prescribing the pitch degree-of-freedom can be eliminated. Chapter 4 studies a fully-passive oscillating-foil turbine technology. While the full details of the concept are described in greater detail in the chapter, it is mentioned here that the term 'fully-passive' refers to a system where the oscillations are not directly prescribed or constrained in any sense, with the exception of guides preventing motion outside the desired pitch and heave degrees-of-freedom. The turbine develops flow-induced, self-sustained motions as the result of a stall flutter phenomenon. This presents an opportunity to greatly reduce mechanical losses in the system. While the fully-passive technology was originally proven by Boudreau [20], the present work assesses the robustness of the concept by subjecting it to sets of real-world conditions, such as high turbulence intensities, and sustained perturbations.

The topics studied within this thesis would be difficult and expensive to model numerically with high fidelity. For the study of the flexible foil propulsors, these difficulties include finite aspect ratio effects, resulting in strong spanwise and chordwise vortex interactions, and the coupled fluid-structure interaction between the unsteady flow and the body of the structure with non-linear stiffness. For the study of the fully-passive turbine prototype, this includes high levels of freestream turbulence, transition to turbulence within the boundary layer, wake dissipation or recovery several chord lengths downstream of the foil, and the influence of mechanical frictions on the system. To numerically resolve these unsteady events in 3-dimensional space would become prohibitively expensive. Considering the potential sensitivity of the design to these real-world effects, and that the intent of the study is to showcase the prototype as an effective proof of concept, it is important to account for these details.

For these reasons, it was decided that these studies are best performed experimentally.

1.4 Details of the author's contributions

The remainder of this thesis is divided into three main chapters, each drafted with the intent of submission for archival journal publication. The purpose of this subsection is to explicitly state the contributions of the author of this thesis, and the contributions of the listed co-authors in each respective paper.

Paper 1

D. Iverson, M. Rahimpour, T. Kiwata, P. Oshkai, (2018). **"Effect of Chordwise Flexibility on Propulsive Performance of High Inertia Oscillating-Foils"**. In: Submitted for review to the Journal of Fluids and Structures.

This paper summarizes an experimental campaign on flexible oscillating-foils acting as a thrust generation device. The experiments, including data collection and analysis, and first writing of the paper were performed by myself. The original paper draft was then revised with the assistance of the co-authors. M. Rahimpour also assisted in preliminary configuration of the flow imaging systems, and P. Oshkai provided guidance in terms of research direction.

A version of the research was also presented by myself at the 9^{th} International Symposium of Fluid-Structure Interactions, Flow-Sound Interactions, Flow-Induced Vibration & Noise, on July 9^{th}, 2018.

Paper 2

D. Iverson, M. Boudreau, G. Dumas, P. Oshkai, (2018). **"A Fidelity Assessment of Experimental Scale Oscillating-Foil Turbines"**. In: To be submitted to the Journal of Fluids and Structures.

This paper contains experimental work on the performance of oscillating-foil turbines operated in transitional Reynolds number flows. The experiments and the first writing of this paper were performed by myself. M. Boudreau, G. Dumas, and P.

Oshkai provided valuable guidance on the research direction and comments on the first draft.

A preliminary version of the work was presented by myself at the 9^{th} International Symposium of Fluid-Structure Interactions, Flow-Sound Interactions, Flow-Induced Vibration & Noise, on July 10^{th}, 2018, there titled "*Experimental Investigation of Boundary Layer Tripping on Oscillating-Foil Turbines*". M. Boudreau, G. Dumas, and P. Oshkai provided assistance in revising the original draft of this conference paper.

Paper 3

D. Iverson, M. Boudreau, G. Dumas, P. Oshkai, (2018). **"Reliability Study of a Fully-Passive Oscillating-Foil Turbine Concept"**. In: To be submitted to the Journal of Fluids and Structures.

This paper covers the experimental testing of a novel fully-passive oscillating-foil turbine. The campaign focused on assessing the performance of a physical prototype under varied sets of disturbances, to gain an understanding of its reliability. The experiments, paper drafting, and editing were performed by myself.

M. Boudreau was instrumental in the initial set-up of the fully-passive device. This is gratefully acknowledged. As well, M. Boudreau, G. Dumas, and P. Oshkai provided guidance into the direction of the research.

Chapter 2

Effect of Chordwise Flexibility on Propulsive Performance of High-Inertia Oscillating-Foils

Abstract

A parametric experimental study was performed to quantify the effects of structural properties and kinematic parameters on the propulsive performance of a low-aspect ratio oscillating-foil at a chord-based Reynolds number of $80,000$. Multiple foils of the same shape but varied construction allowed explicit comparison of the effect of stiffness and inertia. Forces exerted on the foil were directly measured using a load cell and decomposed into thrust and efficiency values. Quantitative patterns of phase-averaged flow velocity and out-of-plane vorticity in the near-wake of the foil were obtained using particle image velocimetry (PIV). Flexibility was shown to improve the thrust generation and efficiency of the oscillating-foils in comparison to a rigid foil baseline, particularly in heave-only kinematics. The trailing edge angle of the foils was observed to have the highest influence on thrust production, and the thrust results were insensitive to whether this was achieved by passive deformation of the foil or through a prescribed pitching motion.

2.1 Introduction

The prevalence of oscillating wings found in nature warrants research into the associated biomimetic technologies that could be developed from these principles. This mandates a need for a deep understanding of the fundamental fluid-structure interactions involved. The study of foils oscillating in pitch and heave has been increasing in recent years, where flapping-wing technologies have proven successful in a range of applications, including clean energy extraction in tidal and wind flows, lift generation in micro-aerial vehicles, and thrust generation for aquatic locomotion. The works of Young et al. [21], Shyy et al. [22], and Bandyopadhyay [1], provide comprehensive reviews of these subjects.

When acting as a thrust generator, oscillating-foil designs propose an elegant alternative to traditional rotary propellers, which have limited ranges of operational speeds where efficiency is maximum [23]. Persons in doubt of the performance of oscillating-foil propulsors are surely convinced by examples existing in nature, where dolphins travel at speeds in excess of 10 m/s, and 30-ton whales can fully breach the ocean's surface [24], [25].

Oscillating-foils present a potential to mitigate some issues with conventional rotary propellers such as poor scaling (known as the tip-speed problem) and high-noise pollution from cavitation sources [26]. Marine vessels propelled by oscillating-foils could also achieve increased manoeuvrability, where unsteady flow dynamics can provide the high instantaneous forces needed for rapid directional changes. Bandyopadhyay [27] observed that the turning radius of a traditional propeller craft is at least an order of magnitude higher than the corresponding value for a fish. Indeed, these benefits are achieved while matching, or in some cases exceeding, efficiencies of rotary propulsion devices. Triantafyllou and Triantafyllou [2] have predicted propulsion efficiencies from oscillating-foil systems as high as 87%, while Fish et al. [28] have estimated that flukes of marine fauna can reach efficiencies of 90%. However, despite growing research interest, wide-spread adoption of oscillating-foil systems by industry has been slow due to the inherently complex fluid-structure interactions and the intricacies of mechanical systems needed to provide appropriate kinematics.

The performance of oscillating-foil systems is strongly influenced by the foils shape, structural properties, operating kinematics, and operating environment, which altogether yield a significant governing parametric space in which such systems could be designed [29]. As an example of how formidable a challenge this can pose, Barrett et

al. [30] sought to design a robotic tuna replica from a set of 14 discretized governing parameters and estimated that more than 10^{11} discrete design combinations could be achieved. Of course, sampling each design point would be astronomical in expense, so the authors used a genetic algorithm to converge upon high performance combinations of the parameters. The parametric space can instead be reduced in size by analyzing the solutions that nature has slowly converged to. Important information on the subject has been learned by examining biological designs. For instance, reviews on the many studies of marine swimmers has shown that, in terms of optimal efficiency, the oscillating frequencies for efficiency of fins and tails nearly universally collapse into a range of Strouhal numbers between $0.2 < St < 0.4$ [14], [15]. This range corresponds to the frequency of the most unstable eigenmode of the jet generated by the oscillating fin or tail [31]. Other valuable insights have ranged from efficient wing cross sections [32], to how fish exploit vorticity in the wakes to minimize the cost of locomotion [33], to the effects of bumps on whale flukes [34]. Although such knowledge helps refine potential design parameters, it helps remind one of the many factors and conditions influencing system performance.

The subject of oscillating-foil propulsion has also been approached from engineering perspectives. Development of oscillating-foil or -wing systems dates back to the early eras of flight attempts, where crude wings were fashioned to the arms of hopeful inventors. More scientific methods were historically applied in early studies by Garrick [9], Lighthill [35], and Wu [36], which outlined the potential for oscillating-wing systems to achieve high propulsive efficiencies. These numerical studies were based on small-amplitude potential theory, which was unable to account for unsteady flow phenomena such as flow separation. The significance of unsteady flow dynamics on oscillating-foil performance, both for propulsion and lift-generation applications, has since been understood. An often cited example is that of insect flight, which if based off steady potential theory should theoretically not be possible [37]. Clearly, insects do fly, which is attributed to the high instantaneous lift values generated by dynamic stall phenomena as confirmed by flow visualization experiments and computational fluid dynamics (CFD) models [38].

Advances in numerical and experimental capabilities in recent years has renewed interest in the subject, and facilitated many novel studies including those on flexible foils. It was highlighted, at least as early as in the works of Katz and Weihs [26], that passive chordwise flexibility of the wing or foil can improve propulsive efficiency at the expense of small decreases in net thrust. This result has been confirmed by other

researchers, including in the literature of Prempraneerach et al. [39], Miao and Ho [40], Dai et al. [41], and Egan et al. [42].

Although numerical campaigns provide insight into the parameters not easily measured experimentally, the existing studies have often relied on simplifications that have been restricting. For example, Liu and Bose [43] performed a comprehensive study on foil flexibility using panel methods, but such an approach was unable to capture important flow dynamics including separation. In other works, such as that by Lin et al. [44], oscillating-foils are analyzed as two-dimensional flows or at low Reynolds numbers, neglecting the effects of finite aspect ratios and turbulence.

Of the fewer experimental works that have tested the impact of flexibility on oscillating propulsors, many considered low Reynolds number, laminar flow conditions (for example, Park et al. [45]). In reality, even practical small-scale aquatic devices are likely to operate at least at Re $\mathcal{O}$ (10^4) or greater, while fish and marine mammals may operate at as high as Re $\mathcal{O}$ (10^8) [46]. The physics observed in laminar regimes may differ from cases with turbulent flow and similarity cannot be generally assumed. In particular, the boundary layers of oscillating-foils are sensitive to transition from laminar flow to turbulence, the latter resulting in boundary layers that are less likely to separate. This issue has been addressed in the context of energy harvesting oscillating-foils, where CFD simulations predicted peak energy extraction efficiencies of 34% for laminar flows ($Re = 1100$), but 43% for turbulent flows ($Re = 500,000$) [11], [18]. In the higher Reynolds number cases, development of leading edge vortices was delayed to higher effective angles of attack, contributing to the differences in recorded efficiencies.

Research into the effect of inertial properties and its relation to performance of flexible foils has again been mainly limited to numerical campaigns, in which this structural property may be varied readily [47], [48]. These studies have found inertia to be an important parameter, having an influence on the passive deformation of the flexible foils. Daniel and Combes [49] analyzed the forces causing the deformation, differentiating between inertial-elastic mechanisms and pressure-based fluid loading. They suggested that, as a general guideline, flexible wings in air deform predominantly due to inertial terms, whereas deformations in oscillating fins and tails in aquatic environments are primarily due to pressure forces. This effect was further analyzed in recent work by Olivier and Dumas [50], who used a partitioned fluid-structure interaction algorithm to study propulsive performance of inertia-driven and pressure-driven wings at low Reynolds numbers.

Nearly all experimental studies on flexibility at moderate Reynolds numbers (i.e., aimed at swimming devices) have not studied the influence of inertia. An exception is the work of Richards and Oshkai [51], who designed a system to test both flexibility and inertia of oscillating propulsors. The authors investigated several flexible foils with variations in inertial moments and chordwise stiffness. This was achieved by embedding lead weights very near to the foils trailing edges to increase inertia, and using thin steel sheets along the foils chord lengths to increase stiffness. The foils themselves were otherwise constructed from a flexible rubber. Two of these foils are used in the current study, and are described further in Section 2.2.1. Richards and Oshkai [51] directly measured the forces exerted on the foils under a range of heave-only conditions, and concluded that of the foils tested, the heavier and stiffer foils produced the highest efficiencies.

The current experimental campaign considered various combinations of chordwise flexibility, inertia, and pitching kinematics on propulsive performance of an oscillating-foil, at a chord-based Reynolds number of $Re_c = 80,000$. The work is novel in analyzing flexible foils with high inertia values in water environments and testing a wide parametric space of pitch-frequency combinations

2.1.1 Oscillating-foil nomenclature

Non-dimensional thrust coefficient C_T, power coefficient C_P, and efficiency η are applied as performance metrics for oscillating-foil systems, defined as:

$$C_T = \frac{F}{0.5\rho U^2 bc}\,, \tag{2.1}$$

$$C_P = \frac{P}{0.5\rho U^3 bc}\,, \tag{2.2}$$

$$\eta = \frac{\overline{C_T}}{\overline{C_P}}, \tag{2.3}$$

where F is thrust force in the direction of travel, ρ is fluid density, U is the streamwise velocity of fluid relative to the foil, b is the span length, c is the chord length, and P is power input. Terms presented with overbars ($\bar{}$) represent cycle-averaged quantities.

The thrust force and the power input were calculated as:

$$F = \frac{1}{nT}\int_0^{nT} \mathrm{F}(t)dt \ , \tag{2.4}$$

$$P = \frac{1}{nT}\left[-\int_0^{nT} Y(t)\frac{dh}{dt}dt - \int_0^{nT} Q(t)\frac{d\theta}{dt}dt\right], \tag{2.5}$$

where F is the streamwise force, Y is the lateral force, and Q is the torque about the pitching axis. The terms h and θ are the heaving and pitching positions, T is the oscillation period, and n is the number of cycles over which the average is computed. The flow regime is classified by the chord-based Reynolds number (Re_c), while the Strouhal number (St) is a measure of oscillation frequency f, normalized by the wake width A and the freestream velocity as follows:

$$Re_c = \frac{Uc}{\nu} \ , \tag{2.6}$$

$$St = \frac{fA}{U} \ , \tag{2.7}$$

Here, ν is the kinematic viscosity of the fluid. The wake width, $A = 2H_0$, is conventionally taken as twice the heave amplitude. The quantities of time, heave position, and the out-of-plane vorticity component, have been non-dimensionalized according to their appropriate scales as:

$$t^* = t/T \qquad H^* = H/H_0 \qquad \omega^* = \omega c/U, \tag{2.8}$$

where t is time, T is the oscillation period, H is the heave position, H_0 is the heave amplitude, and ω is the out-of-plane vorticity component.

2.2 Experimental system and techniques

Experiments were performed in a recirculating water channel with a working cross section of 45 cm x 45 cm and a length of the test section of 250 cm. The test section of the flow channel was closed with a lid to mitigate the effect of the free surface. A slot was cut into the lid to allow the mounting shaft of the test foil to pass through, and the water level was filled slightly above the top of the slot such that no air interface was present within the test section. The uniform inflow was controlled to $\pm 0.004\, m/s$,

and was measured using particle image velocimetry (PIV) at the entrance of the test section. The turbulence intensity of the inflow was $< 0.9\%$ of the mean velocity value for the range of the inflow velocities used.

A schematic of the experimental apparatus is shown in Fig. 2.1. The foil was centered in the cross section of the flow channel. The blockage ratio, defined here as the ratio of the frontal area swept by the leading edge of the foil relative to the cross-sectional area of the test section of the flow channel, was on the order of 5%. If the swept area of the trailing edge is used instead to define the blockage ratio, the ratio increases to up to 8% for cases with high pitch and low stiffness. The complexity of blockage corrections for oscillating-bodies operating in confined environments is highlighted by Gauthier et al. [52], where it was observed that common correction methods, such as the BW blockage correction [53], may be inaccurate if large-scale vortices are present. For the purposes of this study the effect of the channel confinement was neglected, as the use of unverified blockage correction models increases uncertainty. An assumption was made that the influence of confinement would be sufficiently uniform across all data points and would not produce artificial trends in the data.

Heave and pitch motions were controlled independently by separate servo motors. The heave motor was rigidly mounted onto the water channel frame and connected to a linear carriage that generated the heave motion. The pitch motor was mounted onto the heave carriage, to which a load cell and the test foil were attached. A proportional-integral-derivative (PID) control system was used to prescribe the desired motion profiles, with position feedback supplied by motor encoders. The peak error between true heave position and the applied heave position was under 1.1% of the heave amplitude, where the largest deviations occurred at the higher motion frequencies. The peak following error on the pitch axis was less than 0.5%. The effect of these errors on the results was low, as the forces were recorded and integrated over the actual motion profile, rather than the prescribed motion profile. The complete quantification of uncertainties related to the motion system and the force recordings is provided in the thesis of Richards [16].

Both heave and pitch motion profiles were sinusoidal, with a phase difference of 90° between them, as shown in Fig. 2.2. This motion was based on the results of Hover et al. [54], who concluded that sinusoidal profiles generally yield the highest performances, in contrast to other motions such as symmetrical sawtooth wave and square wave profiles. A positive pitch angle is defined here as the direction of rotation

that would allow the foil to align towards the motion path, as shown by the solid lined foils in Fig. 2.2. Some of the experiments used a negative pitch angle, which has the opposite orientation, as shown by the dashed foil shape in Fig. 2.2.

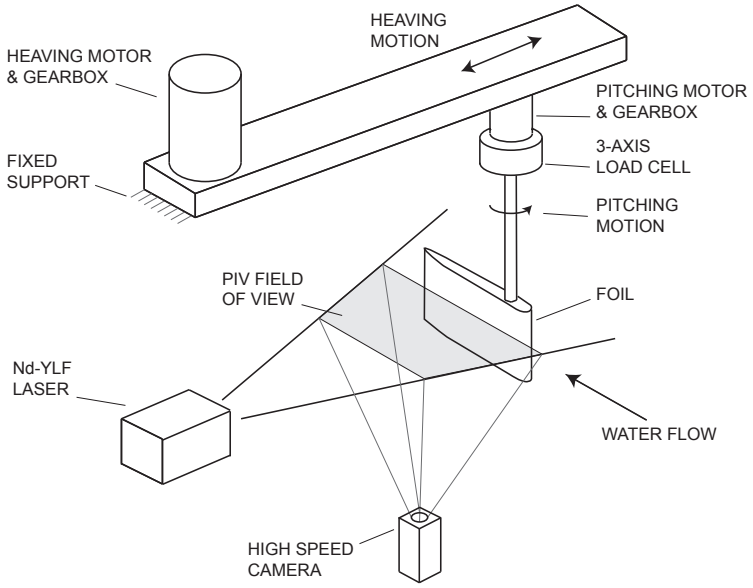

Figure 2.1: Schematic of the experimental configuration, showing the motion control, force measurement and flow imaging systems.

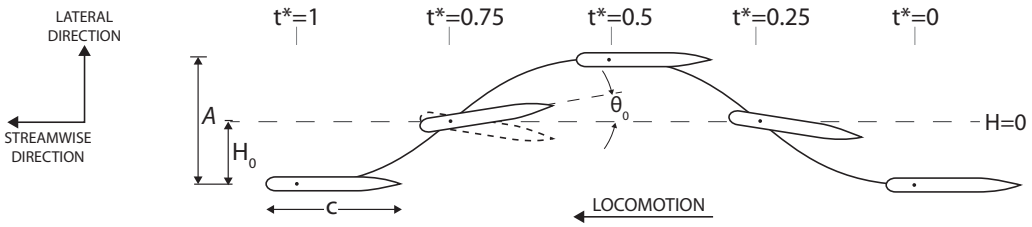

Figure 2.2: Kinematic diagram of the sinusoidal motion of the foil.

2.2.1 Foil construction

Three foils of identical shape, but with different structural parameters, were used in experiments. All foils had a chord length of $c = 200\,mm$ and a span length of $b = 140\,mm$, yielding a low aspect ratio of $AR = 0.7$. The cross-section of the foils is shown in Fig. 2.3. This geometry was created to allow a weight to be embedded near

the trailing edge of one of the foils, positioned at a distance $0.8\,c$ from the leading edge. The location of the mass far from the pitch axis generated a higher moment of inertia than would otherwise be possible. The choice of a cross-section that is flat along most of its chord length was also applied by Olivier and Dumas [50], who noted that such a geometry emphasizes the ability of flexibility effects to shape the wing. For all foils, the pitching motion was about the axis of the aluminum shaft shown in Fig. 2.3, located a distance of $0.17\,c$ from the leading edge.

Of the three used foils, one, referred to here as foil 'R', was constructed of plastic that is from a practical standpoint assumed to be fully rigid. Foil 'R' did not have an additional embedded mass. The other two foils were constructed of a flexible silicon rubber. Flexible foil 'A' had a mass of 140 g embedded at the trailing edge location, and was reinforced in the chordwise direction by a stainless steel sheet. Richards and Oshkai [51] observed that, for heave-only oscillation, this foil achieved the highest thrust and efficiency metrics under most conditions. The second flexible foil, 'B', was constructed without the steel sheet or lead mass, and consequently was 34% less stiff than foil 'A'. The structural values of the three foils are presented in Table 2.1.

Table 2.1: Structural properties of the three foil designs.

Foil Name	Total Mass (g)	Embedded Mass (g)	Moment of Inertia (g m^2)	Stiffness (N/m)	Resonant Frequency (Hz)
R	513	0	2.81	—	—
A	730	140	4.69	168	2.77
B	572	0	3.16	131	2.57

The moment of inertia about the pitching axis of each foil was computed based off the construction and materials of the foils, assuming a rigid structure. This approach was used to avoid the uncertainties involved in directly measuring the inertial moment of a flexible body. The stiffness of each foil was determined by displacing the trailing edge of the foil a known amount in the direction of rotation, while preventing the pitching axis of the foil from rotating. The moment required to bend the foil was then computed by the force measured with the load cell. The resonant frequency was measured by subjecting each foil to a sudden rotation while submerged in water. The resulting oscillation decay following the motion was recorded with the torque-axis of the load cell, and filtered to determine the dominant oscillation frequency.

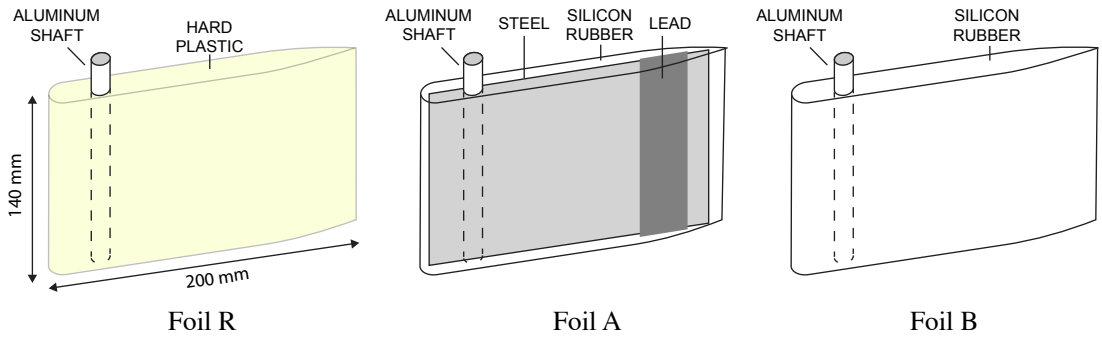

Figure 2.3: Construction of the three tested foils.

2.2.2 Force measurements

A three-axis load cell recorded torque about the pitching axis, and forces normal to and tangent to the chord direction. The load cell was rigidly connected to the foil and therefore its coordinate system was fixed to the pitch motion. Measured force vectors were thus decomposed into streamwise and lateral force components based on the recorded pitch angle. The streamwise and lateral directions were associated with the directions of thrust and power input, respectively, as was shown in Fig. 2.2. Forces were sampled at a frequency of 10 kHz, and filtered values were averaged over 20 oscillation cycles, which was sufficient for producing statistically converged results to under 1% uncertainty. Cycle-averaged metrics were computed with a central difference integration scheme. The load cell was factory-calibrated, and the calibration was verified with precision weights representing known loads prior to each experiment.

The experimental configuration resulted in unwanted forces being recorded by the load cell. These included inertial forces associated with mounting equipment located below the load cell's measurement plane, and hydrodynamic forces exerted on the submerged portion of the mounting shaft. These undesired forces were quantified by running a second experiment for each kinematic case, where the foil was removed but the system was otherwise unchanged. The recorded noise forces were then subtracted from trail data, yielding the results presented hereafter. Inertial forces felt by the foil itself were conservative in nature, and yielded no contribution to cycle-averaged performance metrics.

2.2.3 Quantitative flow imaging

Fluid velocity at the midspan of the foil was measured using high-speed particle image velocimetry. The flow was seeded with tracer particles with a mean diameter of $10\mu m$ that were illuminated by a pulsed Nd:YLF dual diode-pumped laser. Only one side of the foil was illuminated by the laser sheet. The symmetrical nature of the foils motion allowed the flow structure on the dark side of the foil to be measured by inverting the appropriate phase on the bright side. For example, images recorded on the illuminated side at a period $t^* = 0.75$ were inverted and used to represent the flow on the dark side of $t^* = 0.25$. Light scattered by the particles was captured by a high-speed digital camera operating at the sampling rate of 120 Hz. The instantaneous velocity fields were calculated by cross-correlating the patterns of tracer particles in consecutive images [55]. The field of view of images was $346mm$ x $346mm$, and the resolution of the image capture was 1024 x 1024 pixels. The final PIV measurements had the spatial resolution of 0.26 vector/mm using the camera lens with the focal length of 24 mm. Phase-averaged distributions of the flow velocity were calculated by averaging 250 instantaneous velocity fields corresponding to the same phase of the foil's oscillation.

2.3 Results and discussion

2.3.1 Foil deformations

The relative importance of inertial and pressure forces experienced by the foils was assessed by comparing deformations occurring when the foils operated in water, experiencing inertial and pressure forces, against deformations occurring when the foils operated in air, where pressure forces were assumed negligible. The observed deflection of the trailing edge of the flexible foils, which is used to represent the extent of the foils' deformation, is provided in Table 2.2 for a representative case. In this case, the foil moved only in heave to avoid trailing edge translation due to pitching motions, and oscillated at $St = 0.35$. The deflection of the trailing edge of the foils was measured within images recorded at the desired phase, and the imaging had a resolution of $0.3\,mm$.

The inertial forces exerted on the foil are proportional to the magnitude of the foil's heave acceleration, which was maximum at positions $H^* = \pm 1$ when the foil reversed its heave direction. Therefore, it was at these locations that the deformation

due to inertial mechanisms was greatest. Here, the deformation of foil 'A' in the air test was 82.5% the value of the deformation in the water test. Foil 'B', which had a lower moment of inertia, showed less deflection at this phase. Still, the inertial forces of foil 'B' were still significant, where the deflection in the air case reached 76% that of the water case.

The inertial forces were minimum when the foil was at midstroke ($H^* = 0$), with zero heave acceleration. As a result, both foils 'A' and 'B' showed no deflection at the midstroke when operating in air. However, at this location the heave velocity was maximum, generating large pressure forces. The effect of pressure forces is apparent in the data of Table 2.2, where large deformations occurred in the water test of both foils. Foil 'B', which was less stiff than foil 'A', deformed more under the pressure load. It is concluded that inertial and pressure forces both had significant influences on the deformation of the flexible foils, but acted at different phases of the foils' motions. Foil 'A' was somewhat more influenced by inertial forces than foil 'B', while 'B' deformed more under pressure loads.

Table 2.2: Recorded trailing edge deflection of foils 'A' and 'B' under the conditions $\theta_0 = 0°$ and $St = 0.35$

Position	Condition		Trailing edge deflection (mm)
$H^* = \pm 1$	Foil 'A'	Air	14.2
		Water	17.3
	Foil 'B'	Air	10.5
		Water	13.5
$H^* = 0$	Foil 'A'	Air	0
		Water	38.8
	Foil 'B'	Air	0
		Water	44.0

2.3.2 Unsteady forces

All experiments were performed at $Re_c = 80,000$ and with a heave amplitude of $H_0 = 0.1875c$, representing a regime of practical interest as outlined by Richards and Oshkai (2015). Pitch amplitudes were varied from $-10°$ to $20°$, and Strouhal numbers were varied from 0.15 to 0.45. The recorded measurements for cycle-averaged thrust production ($\overline{C_T}$), power consumption ($\overline{C_P}$), and efficiency (η) of this parametric range

are presented in Fig. 2.4 for each of the three foils. The black dots in Fig. 2.4 represent conditions where data was recorded, and isocontours are interpolated between the obtained results to produce the visual maps.

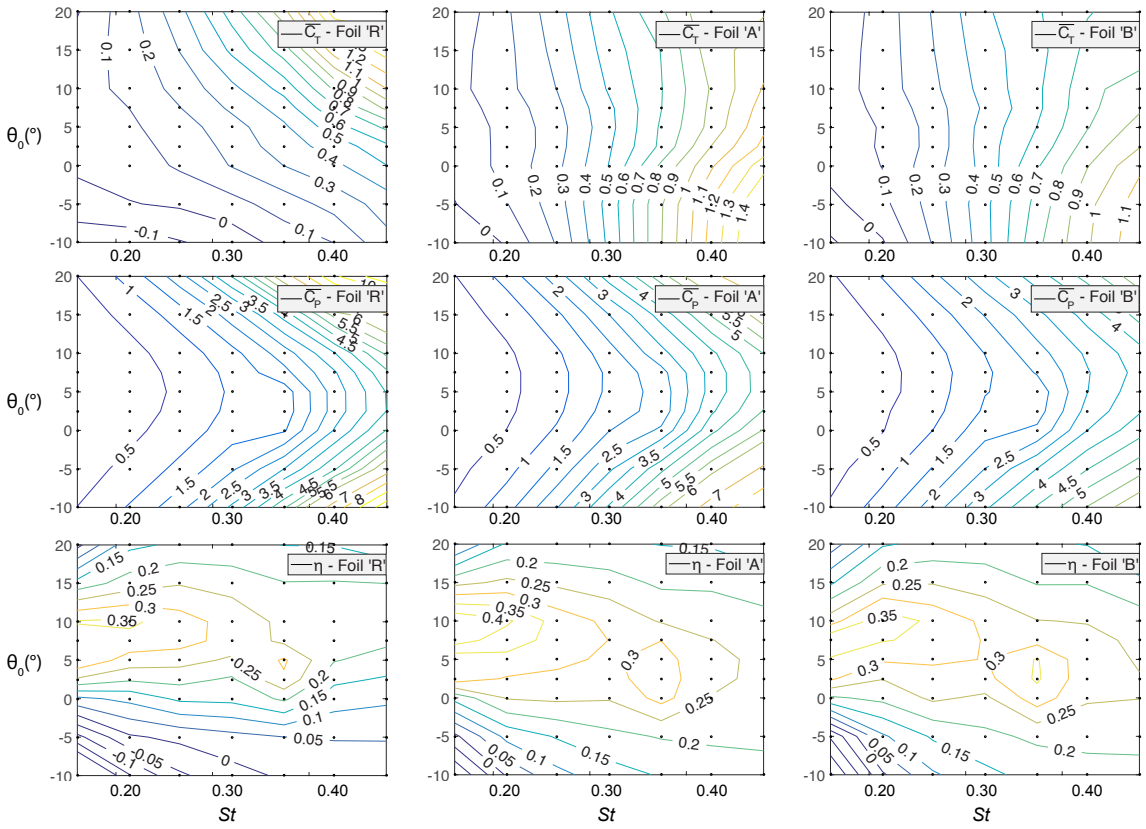

Figure 2.4: Thrust coefficient (top row), power coefficient (middle row), and efficiency (bottom row) as function of pitch amplitude and Strouhal number for foil 'R' (left column), foil 'A' (middle column) and foil 'B' (right column).

As shown in Fig. 2.4, the generated thrust values monotonically increased as a function of Strouhal number for any given pitch angle, for all foils. The trends observed for rigid and flexible foils differed in terms of response to pitch amplitudes. The rigid foil R produced comparatively low thrust during heave-only motions $\theta_0 = 0°$, especially at low Strouhal numbers. Large positive pitch amplitudes were necessary for high thrust production, where the highest values were recorded at the largest tested pitch amplitudes and oscillation frequencies. In contrast, large pitch values were not needed for thrust production on both flexible foils. Rather, in a large region below $St = 0.35$, thrust generation was approximately independent of pitch amplitude and only dependent on the Strouhal number. Above $St = 0.35$, the highest thrust occurred

at negative prescribed pitch amplitudes, whereas the generated thrust diminished at higher pitch angles. Flexible foil 'A', which had a higher inertial moment than the foil 'B', generated thrust values consistently higher than foil 'B'. This difference was most notable at larger Strouhal numbers, where inertial forces were increasingly influential on foil deformation. The increased deformation resulted in an increased the wake width and thus the amount of fluid directly available for thrust production.

The contours of the power coefficient were qualitatively similar for all foils. At each Strouhal number, the lowest power input occurred at low to moderate pitch values, ranging between 2.5° to 7.5°. Here, the rotation of the foils reduced their angles of attack, but the pitch amplitudes were small enough that high power inputs were not required to counter the torque forces associated with large rotations. For all foils, power requirements increased sharply above $St = 0.35$, which is related to poor synchronization of the foil's oscillation frequency with the eigenmodes of the unsteady wake [31].

The flexible foils showed increases in efficiency compared to their rigid counterpart. As an example, under the operating conditions of $\theta_0 = 0°$ and $St = 0.35$, foils 'R', 'A', and 'B' had respective efficiency values of 0.21, 0.32, and 0.33. Further, high efficiency values occupied a larger region of the parametric space for the flexible foils, signifying a larger practical operating range (consider, for example, the contour region of $\eta > 25\%$ in Fig. 2.4). However, in general, the observed efficiency values were lower than the peak efficiencies of oscillating foils reported in literature. This observation is attributed to the low aspect ratio and heave amplitude of the oscillating foil used in the present study, both of which were limited by experimental constraints, and are known to impair efficiency [1].

These results come in contrast to some previous research campaigns, which have noted that the increases in efficiency for flexible foils are typically associated with a slight reduction in thrust [39]. The current investigation suggests that there are exceptions to this generality, where it is apparent that combinations of governing parameters exist that result in flexible foils outperforming rigid foils in both thrust generation and efficiency. These trends are partially attributed to the shape of the foil, which had no camber along most of its length and therefore required other mechanisms to produce thrust force. Presently, the deformation of the flexible foil's trailing edge directly increased the proportion of the foil's surface area normal to the direction of thrust, increasing the available surface area for pressure based forces to propel the foil. This effect is known as force-redirection, and explains the low thrust

production of the rigid foil in heave-only conditions [26].

The select conditions of $\theta_0 = 0°$ and $St = 0.35$, which corresponded to high efficiencies and high thrust values without an imposed pitch motion, are analyzed further in Fig. 2.5 to observe the development of the thrust force throughout the foil oscillation cycle. Instantaneous force measurements, averaged over 20 oscillation cycles, were decomposed into streamwise and lateral directions, as shown in Fig. 2.5. Forces vectors are shown positioned along the sinusoidal motion path of the foil as observed from a frame of reference fixed to the freestream flow. The streamwise direction represents force acting in the direction of locomotion, while the lateral direction corresponds to forces that aid or oppose the heave motion. It is noted that the time axis progresses from right to left, following the convention of the kinematic diagram in Fig. 2.2.

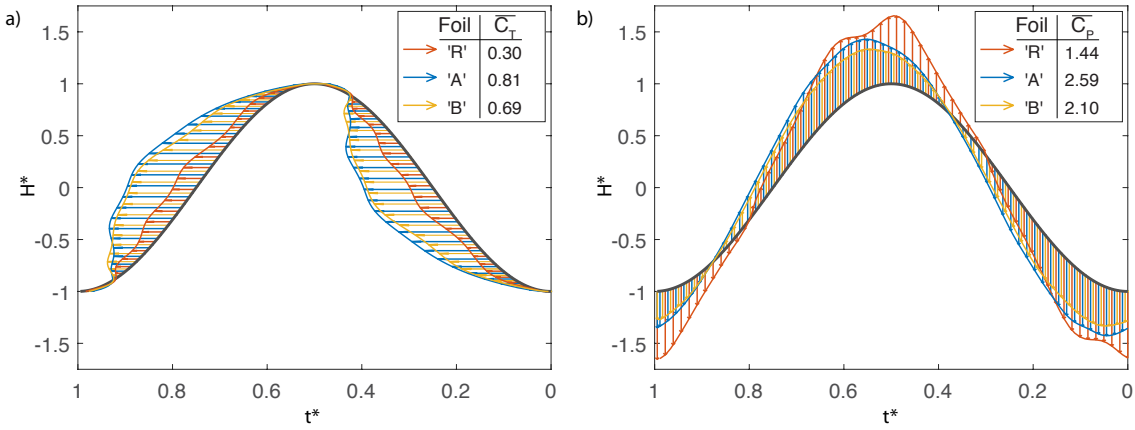

Figure 2.5: Instantaneous force components as functions of time for the case of $\theta_0 = 0°$ and $St = 0.35$. The foils travel from right to left. (a) Streamwise force components. (b) Lateral force components.

Positive thrust production occurred throughout the majority of the cycle, and it was the largest when the foil was near mid-stroke, as shown in Fig. 2.5a. A small net drag force occurred as each foil reversed heave direction, but the net thrust quickly developed and persisted until the opposite heave limit, when the foils changed direction again. The increase in thrust production generated by the flexible foils is apparent in Fig. 2.5a, which shows that the corresponding thrust vectors were consistently larger in amplitude than those corresponding to the rigid foil. The force profile corresponding to the stiffer foil 'A' was similar to that of the foil 'B', but it was marginally higher in magnitude than the latter. When the force profiles were

averaged over a cycle of the foil oscillation, $\overline{C_T}$ values of 0.81 and 0.69 for foils 'A' and 'B', and 0.30 for foil 'R' were obtained.

The lateral force, which is associated with power input to and its recovery from the heave motion, is shown in Fig. 2.5b. The lateral force is only one component of the required input power, while torque, which is not shown, also contributes to the power requirement as per Eq. 1.5. At the beginning of an oscillation cycle, the lateral force opposed the motion of the foil, which resulted in a requirement of an energy input into the system. The direction of the force reversed slightly after the mid-stroke of the foil ($H^* = 0$). Beyond this point, the net lateral forces acted in the direction of motion and the system was able to recover energy. Foils 'A' and 'B' had the zero-crossing points of the lateral force component occurring later in the cycle than foil 'R', signifying differences in the hydrodynamic forces, where in a purely inertial system the zero-crossing point would occur exactly at the mid-stroke when the foil begins to decelerate.

The rigid foil had lower magnitude lateral force throughout most of the oscillation cycle, but very high loadings as the foil reversed direction. It is likely that the ability of the flexible foils to deform under fluid loading lessened the power input required to reverse the heave direction, shown by the lower forces occurring near $H^* = 1$. The plots of Fig. 2.5 demonstrate that the relatively low thrust generated by the rigid foil in these conditions is related to poor alignment of the pressure forces with respect to the direction of locomotion.

Recalling the parametric plots of Fig. 2.5 and the case St = 0.35, the measurements showed that the rigid foil 'R' at $\theta_0 = 15°$ had a cycle-averaged thrust coefficient of $\overline{C_T}$, while the flexible foil 'B' at $\theta_0 = -10°$ yielded a similar thrust coefficient of $\overline{C_T} = 0.76$. The similarity in results is quite remarkable considering the 25° difference in prescribed pitch angle. However, it was observed that the trailing edge of the flexible foil deformed significantly, and was actually oriented to within $\pm 1°$ of the trailing edge of the rigid foil under these conditions. This observation suggests that an optimal angle for the trailing edge exists, but whether the angle is achieved by active pitch control or passive flexibility is of less importance.

Figure 2.6 shows the instantaneous streamwise and lateral force profiles of these two conditions: foil 'R' at $\theta_0 = 15°$ and $St = 0.35$, and foils 'A' and 'B' at $\theta_0 = -10°$ and $St = 0.35$. Despite having similar cycle-averaged thrust values, the actual force generation process for the rigid and the flexible foils was very different. Notably, the streamwise force profiles of all cases in Fig. 2.6 were considerably less smooth than

those of the heave-only cases in Fig. 2.5, showing multiple peaks throughout the oscillation cycle. Both flexible foils generated large forces early in the heave motion, while the rigid foil developed higher forces towards the end of the cycle.

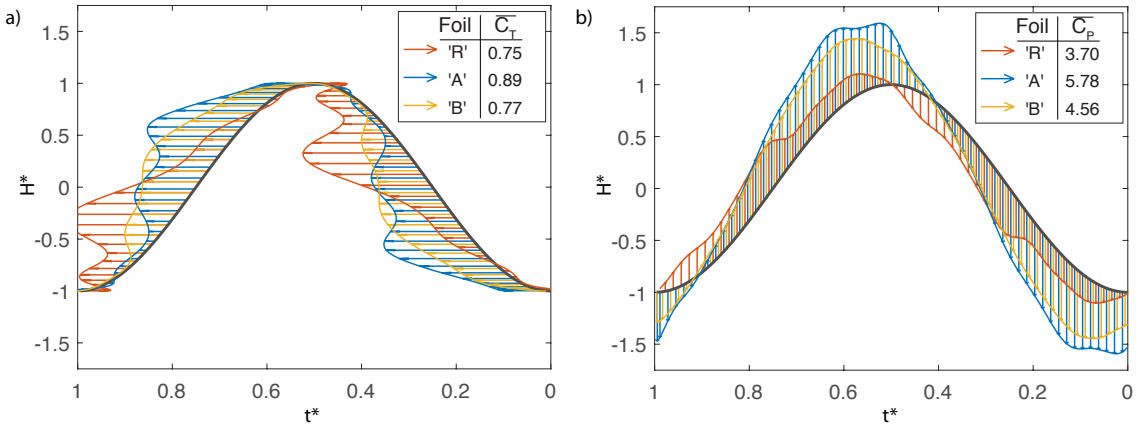

Figure 2.6: Instantaneous force components as functions of time for the cases of $\theta_0 = 15°$ and $St = 0.35$ (foil 'R'), and $\theta_0 = 15°$ and $St = 0.76$ (foils 'A' and 'B'). (a) Streamwise force components. (b) Lateral force components.

2.3.3 Quantitative flow patterns

The PIV technique was applied to acquire quantitative flow images around the foils in order to provide insight into the mechanisms of generation of the unsteady forces discussed in Section 2.3.2. Fig. 2.7 provides phase-averaged contours of the out-of-plane vorticity for foils 'R' and 'B' under the conditions of $\theta_0 = 0°$ and $St = 0.35$. The development of the vortical flow structures is shown at sequential phases $t^* = 0/8$, $1/8$, $2/8$, and $3/8$, representing the evolution of the first half of the symmetrical wake structure. The symmetrical motion of the foil allows information of the second half of the motion cycle to be inferred from the first half. For example, phase $t^* = 4/8$ is simply an inverted image of phase $t^* = 0/8$, and therefore it is not shown herein.

Hereafter, the terms upper surface and lower surface are used to refer to the upper and the lower sides of the foil in the frame of reference provided in Fig. 2.7. For the phases shown, the upper surface acts as the pressure side of the foil, and the lower surface acts as the suction side, but this relationship is opposite for the second half of the foil oscillation cycle.

At phase $t^* = 0$ in Fig. 2.7a, corresponding to the bottom of the heave cycle of the rigid foil, the flow was attached to the lower surface of the foil, except near the leading

edge, where a weak leading edge vortex (LEV) persisted from the previous oscillation cycle. As the heave motion continued, the boundary layer on the lower side began to roll up into a new LEV, but the vortex did not convect downstream significantly before the foil reversed the heave direction. The LEV further dissipated before it could directly influence the trailing edge vortex (TEV) development. On the upper surface of the foil at phase $t^* = 0$, the negative vorticity had begun shedding from the trailing edge. The shear layer characterized by the negative vorticity continued to shed from the trailing edge during the first half of the oscillation cycle, and it progressively rolled up into a large-scale TEV that became the dominant flow structure in the wake.

The flow dynamics around the leading edge for foil 'B', shown in Fig. 2.7b, were very similar to that of the rigid foil 'R', in terms of the LEV's timing, peak vorticity level, and size. This similarity was a consequence of the pitching axis being positioned close to the leading edge, such that the leading edge was too short to deform considerably, thereby maintaining a near 0° angle with respect to the freestream throughout the cycle for both the rigid and the flexible foils.

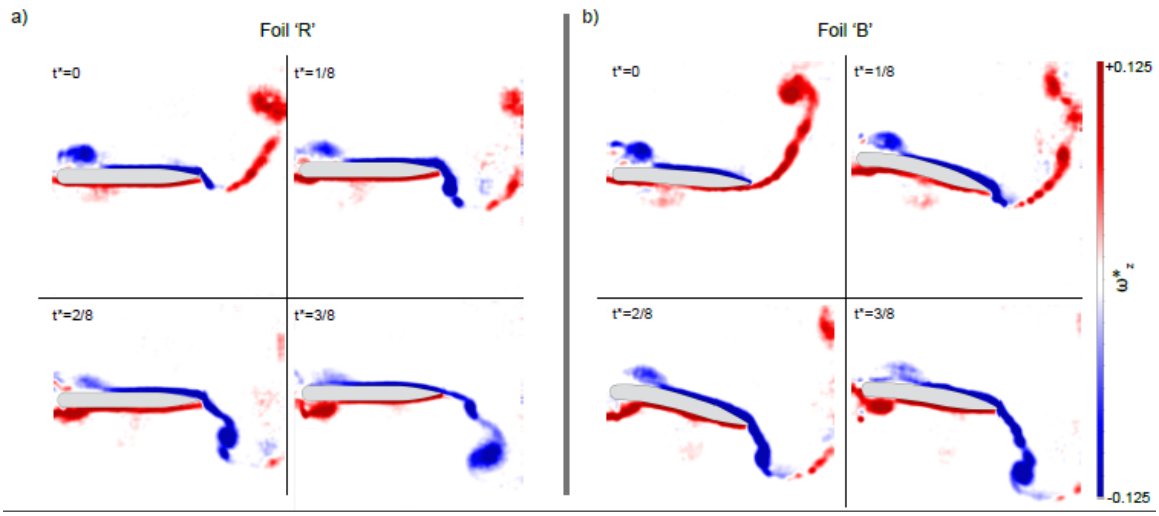

Figure 2.7: Patterns of phase-averaged out-of-plane vorticity for the case of $\theta_0 = 0°$ and $St = 0.35$. Flow direction is from the left, and heave motion is upwards. (a) Foil 'R'. (b) Foil 'B'

The flexibility of the foil showed a larger influence on the vortex dynamics in the vicinity of the trailing edge. The onset of the shedding of the negative vorticity from the upper surface of the foil was not observed until the phase $t^* = 1/8$ on foil 'B'. The resulting difference manifested itself in a more concentrated TEV than that observed on the rigid foil. Additionally, the wake generated by the flexible foil was considerably

wider than that of the rigid foil, which was attributed to the larger area swept by the trailing edge of the flexible foil.

The effect of the pitching motion on the flow dynamics is illustrated in Fig. 2.8, which provides contours of the out-of-plane vorticity for foils 'R' and 'B' for the cases of $\theta_0 = -10°$, 5°, and 15°. All images correspond to the same phase $t^* = 2/8$, and constant Strouhal number $St = 0.35$. Neither the pitch amplitude nor the trailing edge flexibility had significant influence on the dynamics of the LEV. The LEVs had relatively low peak vorticity levels and spatial extent in all considered cases.

In contrast, the maximum pitch amplitude had a more pronounced effect on the separated flow structure in the vicinity of the trailing edge of the foil. In general, increasing the pitch amplitude had an effect of delaying the development of the TEV. This effect can be observed by comparing the cases of $\theta_0 = 15°$ with the cases of $\theta_0 = -10°$, the latter resulting in a more developed large-scale vortex in the wake at the same phase in the cycle.

The cases of foil 'R' at $\theta_0 = 15°$, and foil $\theta_0 = -10°$, had similar cycle-averaged thrust values despite the different pitch angles, as previously noted. The PIV images of Fig. 2.8 show that the flexible foil deformed significantly; at mid-stroke developing a +15° angle with respect to the freestream. This observation suggests that the effective angle of the trailing edge with respect to the freestream is a key parameter in thrust production. It should be noted that continually increasing the flexibility of the foil does not lead to a sustained increase in propulsive performance. For foil 'B', the conditions $\theta_0 = 5°$ and $\theta_0 = 15°$ both lead to reductions in thrust. The prescribed pitch and flexibility of these conditions caused the trailing edge to deform beyond the optimal value of the effective angle of attack. Considering the previous observations that power input for all foils at all Strouhal numbers was minimum between $\theta_0 = 2.5°$ and $\theta_0 = 7.5°$, it is proposed that there exists an optimal stiffness level that would result in maximum thrust also occurring in this interval. In this scenario, the trailing edge would deform to $\sim 15°$ when prescribed a pitch amplitude of $\sim 5°$. Such a foil would have minimum power input, maximum thrust generation and, therefore, peak efficiency.

The angle of the trailing edge leading to highest thrust generation is a function of Strouhal number, a relation that should not be overlooked. The oscillation frequency is directly linked to the heave velocity of the foil, thus affecting its effective angle of attack. The heave velocity also influences the loading exerted on the foil, in turn affecting the propulsive performance. The influence of the Strouhal number is

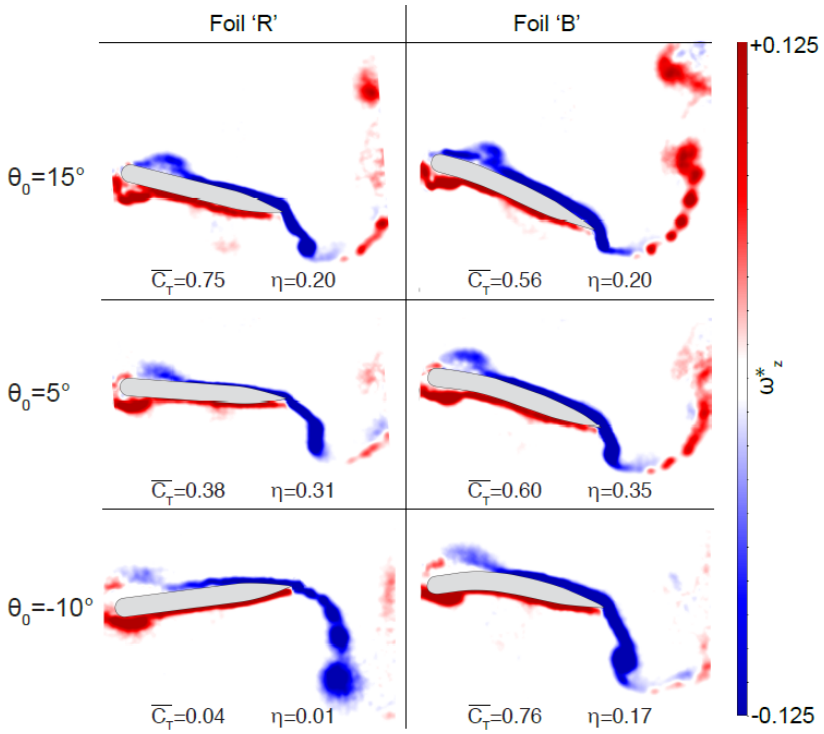

Figure 2.8: Patterns of phase-averaged out-of-plane vorticity for the case of $St = 0.35$ and phase $t^* = 0.25$ for foils 'R' (left column) and 'B' (right column) at various maximum pitch amplitudes.

illustrated in Fig. 2.9, which shows distributions of the out-of-plane vorticity at the phase $t^* = 2/8$ for the rigid foil 'R' and the flexible foil 'B', both of which were undergoing heave-only motion. The flexible foil 'B' deformed to greater extent at higher Strouhal numbers, leading to the increased thrust and efficiency at both considered Strouhal numbers. The cycle-averaged thrust coefficient generated by the flexible foil was approximately twice as high as the corresponding thrust coefficient of the rigid foil for both $St = 0.25$ and $St = 0.45$. However, as the Strouhal number increased, the ratio of efficiencies of the flexible foil over that of the rigid foil increased from 1.6 at $St = 0.25$ to 2.3 at $St = 0.45$. The vorticity plots of Fig. 2.9 show that this increase in efficiency is linked to the delayed development of the TEV in the case of the flexible foil 'B' at the higher Strouhal number.

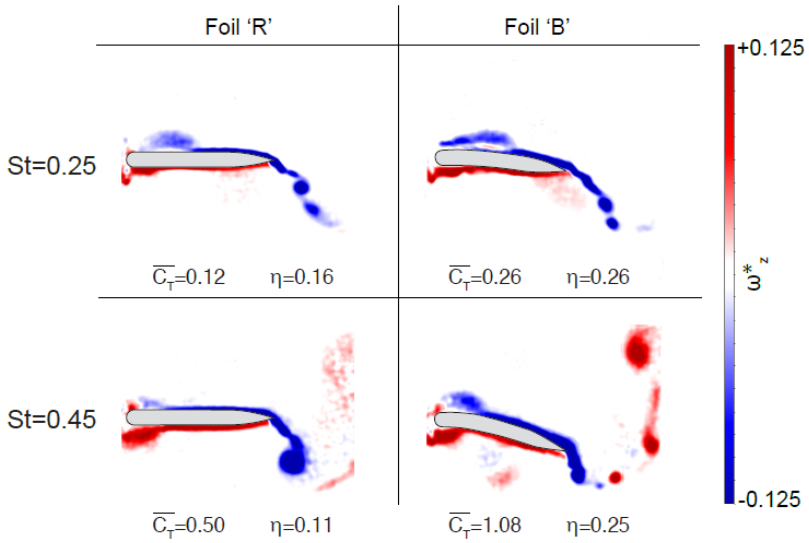

Figure 2.9: Patterns of phase-averaged out-of-plane vorticity for the case of foils 'R' and 'B' at different Strouhal numbers at phase $t^* = 0.25$, and $\theta_0 = 0°$.

2.4 Conclusions

An experimental campaign was conducted to study the effects of chordwise flexibility and pitching kinematics on the performance of oscillating-foils acting as propulsion devices. Two flexible foils, with different moments of inertia and stiffness, were compared against a baseline foil that was fully rigid. The amplitude of prescribed pitch motion was varied from $-10°$ to $20°$, and Strouhal numbers were varied from 0.15 to 0.45. Although this experimental range represents a small portion of the formidable parametric space that governs oscillating-foil propulsion, some notable underlying trends were observed. In general, the flexible foils produced higher thrust values than their rigid counterpart, as well as higher propulsive efficiencies.

Inertial forces were the dominant mechanism producing foil deformation at the beginning and end of a heave cycle, where heave acceleration was highest. This also corresponded to a point in the oscillation cycle that deformation due to pressure forces was low. These inertial forces promoted beneficial curvature early in the cycle which would otherwise be absent. At the midstroke of the foil's motion, pressure forces were responsible for the majority of deformation.

Trailing edge flow dynamics were observed to have a strong influence on performance. Specifically, an appropriate level of pitch applied to the trailing edge was seen necessary for high thrust generation. The results were insensitive to the mecha-

nism producing the pitch, whether being actively prescribed to the rigid foil or being allowed to develop passively via flexible foil deformation. It was proposed that an optimal level of foil stiffness could be predicted such that at low prescribed pitch angles, where power input was minimum, the foil's trailing edge would deform an optimal amount. A foil that deformed more than or less than such a value would experience a degradation in performance.

As a result of the necessity for trailing edge pitch, it was noted that the rigid foil operating in heave-only motions performed poorly. Under the same operating conditions, the flexible foils produced thrust values larger than twice the value of the rigid foil.

Chapter 3

A Fidelity Assessment of Experimental Scale Oscillating-Foil Turbines

Abstract

The current work assesses the fidelity at which scaled oscillating-foil turbine experiments can represent higher Reynolds number, more practical conditions. The work is motivated by previous observations of the distinct difference in turbine performance between laminar and turbulent flow regimes, coupled with the reality that the scale of many experimental systems leads to transitional Reynolds numbers. The issues of dynamic stall, forced transition, and channel confinement are addressed. Experiments were performed in a recirculating water channel in a Reynolds number range from $20,000$ - $50,000$, on a NACA 0015 foil of aspect ratio 7.5. Direct force measurements were used to quantify turbine performance, and particle image velocimetry techniques were used to analyze flow dynamics. Despite the low Reynolds numbers of the study, turbulent boundary layers were observed for many cases when the foil dynamically oscillated. This allowed results, especially those with a roughened surface, to tend towards baseline cases at $Re = 500,000$.

3.1 Introduction

A wing shape that oscillates in pitch and heave can, under proper kinematics, be used to harvest energy from a flow [56]. The pitch and heave amplitudes of oscillating-foil energy harvesters typically exceeds those studied in other applications, such as helicopters [57] and micro-aerial vehicles/insect flight [22], leading to unique flow dynamics. These motions result in a delay of flow separation to angles of attack higher than would occur in static conditions, and in many cases cause the oscillating-foils to develop deep dynamic stall that is closely linked with turbine performance. The stall events are complex and a function of many parameters, which has made the scaling of laboratory-sized experiments fundamentally uncertain.

The history of oscillating-foils as energy extraction devices from steady flow began with the pioneering work of McKinney and DeLaurier [58] and their so-called Wingmill, which served as an effective proof of concept. The concept has since been studied by several research groups, with interest increasing in recent years. Early numerical studies were performed at low Reynolds number flow regimes, typically in the range of Re $\mathcal{O}(10^3 - 10^4)$, as limited by practical computational expense. Kinsey and Dumas [11] performed a parametric study in this regime ($Re = 1100$), quantifying the influence of pitch and heave amplitudes, and oscillation frequency. The study highlighted the importance of well-defined kinematics on system performance, while other parameters such as foil shape were less influential. The prescribed pitch, heave, and frequency combined to define the effective angle of attack that the foil experienced throughout an oscillation cycle. When the effective angle of attack was prescribed such that a large leading edge vortex (LEV) was shed in proper phase with the periodic motion, the low pressure core of the LEV beneficially contributed to power extraction. The significant influence of the LEV on system performance is reviewed by Young et al. [21]. It is worth noting though, that Reynolds number has an impact on the generation and stability of the LEVs, and different turbine performances have been noted at higher Reynolds numbers.

The boundary layer dynamics, and therefore the mechanisms leading to the development of the LEV, are affected by the order of magnitude of the Reynolds number; in particular, the transition from laminar flow to turbulence. As noted by Peng and Zhu [59], there is an underlying need to understand oscillating-foil systems at high Reynolds numbers, which better match the conditions that practically sized turbines would encounter. Numerical work in this area began with Lindsey [60] and Jones et

al. [61] when they performed studies first at $Re = 20,000$ (assuming fully laminar flow), and then at $Re = 100,000$ (assuming fully turbulent flow) and found considerable increases in power efficiency for the latter. Additionally, Campobasso et al. [62] extended their previous laminar study [63] to find an increase in maximum efficiency from 34% at $Re = 1100$, to 40% at $Re = 1,500,000$. All-else-equal, the LEV that developed under many kinematics in the laminar study was suppressed in the turbulent regime due to the increased robustness in the turbulent boundary layer.

Kinsey and Dumas [18], [64], [65] also extended their previous laminar studies to turbulent cases at $Re = 500,000$ using an unsteady Reynolds-averaged Navier-Stokes (uRANS) approach, citing significant improvements in peak efficiency, from 34% to 43%. In the particular study of Kinsey and Dumas [18], a large parametric space was tested in these turbulent flow conditions, showing that dynamic stall was not required for optimal performance, as was the case in laminar tests. Rather, with optimal kinematics, the turbulent boundary layer remained attached to the foil throughout the oscillation cycle providing large instantaneous lift coefficients.

Some experimental prototypes have been tested at moderate or high Reynolds numbers, such as Kinsey et al. at $Re = 480,000$ [19], Poirel et al. at $Re = 130,000$ [66], Abiru and Yoshitake at $Re = 120,000$ [67], McKinney and DeLaurier at $Re = 110,000$ [58], and Sitorus et al. at $Re = 100,000$ [68]. But this represents the minority, and experiments on this scale carry higher expense than their smaller counterparts. More common are experiments with Reynolds numbers on the order of 10^4, often limited by the size of the air or water channels in which they operate. Examples include the campaigns of Lindsey [60], Jones et al. [61], Simpson et al. [69], and Boudreau et al. [20]. These mentioned experimental studies focused primarily on the performance metrics of the turbine systems, without much insight into flow dynamics.

Quantitative flow analysis techniques, such as particle image velocimetry (PIV), have been employed in some other works. Lu et al. [70] studied the formation of the LEV on an oscillating-foil at $Re = 3500$ with PIV, confirming the existence of dynamic stall events experimentally. The shed vortex in the experimental case was somewhat less coherent than in their complimentary two-Dimensional numerical study due to spanwise instabilities, but nonetheless was found critical in achieving high levels of energy extraction. A similar conclusion was reached in the experimental PIV study by Fenercioglu et al. [71] at $Re = 1100$. Siala et al. [72] used PIV to study the effect of flexibility on the dynamic stall of an oscillating foil at $Re = 25,000$. They found that the LEV was the dominant mechanism for lift generation, and that a flexible leading

edge effectively promoted the LEVs formation. Kim et al. [73] used PIV techniques on an oscillating-foil turbine at $Re = 50,000$, finding that finite-aspect ratio effects delayed the formation of the LEV near the foil tips, causing a performance drop. These transitional scale turbine studies have led to many insights, however it has not been explicitly determined if these studies are representative of the flow dynamics and performance of higher Reynolds number, more practical operating conditions, where numerical studies have predicted changes in flow dynamics and turbine performance.

The applicability of laboratory scale experiments is further limited by channel confinement effects, a factor that has been given little attention in previous campaigns. Gauthier et al. [52] assessed the impact of channel confinement effects on turbine performance with a numerical uRANS approach at $Re = 3,000,000$, finding that the establish BW blockage correction [53] was applicable to oscillating-foil turbines under some kinematics, while it was inaccurate in others. The authors found that even at modest blockage ratios of 25%, a relative increase in cycle-averaged efficiency up to 40% could occur. At blockage ratios of 50%, efficiency doubled in some cases. The changes in performance due to confinement were nonlinear. If the intent of an experimental study is to replicate open water, unconfined conditions, the blockage effects may therefore produce artefacts in the data, and misleading trends, if they are not appropriately corrected for.

The current study contributes in assessing the fidelity of moderate scale oscillating-foil turbine experiments, and compares their similarity with lower and higher flow regime studies available in published literature. The effects of transition from laminar to turbulent flow are explicitly addressed. A practical method to force transition with surface roughness elements is proposed, allowing the direct comparison of tripped and untripped boundary layers. Blockage corrections are applied to a parametric experimental dataset and compared against uRANS simulations to evaluate their accuracy. Experiments were performed in a recirculating water channel in a Reynolds number range between $20,000$ and $50,000$. Turbine performance was measured by direct force measurements, and topology of the flow in the boundary layer and near wake of the hydrofoils was recorded with PIV imaging.

3.1.1 Boundary layer dynamics

Stall delay (or separation delay) is a common and fundamental characteristic of oscillating-foil turbines. Stall delay occurs when the boundary layer on a streamlined

body is dynamically kept attached by some means temporarily allowing higher-than-usual angles of attack to be achieved before flow separation. Such a process may or may not end in the shedding of a LEV, depending on several factors. Ericsson [74] proposed that in the context of a rapidly pitching airfoil, separation delay is associated with a Magnus effect [75] on the leading edge. The motion of the leading edge of the foil reduces momentum loss in the boundary layer delaying the onset of separation. Turbulence, if present, also adds momentum to the boundary layer through momentum exchange with the external flow allowing stall separation to be further delayed. This may explain the increases in performances observed in the turbulent numerical oscillating-foil studies over their respective laminar counterparts, where turbulence allowed the foils to reach higher angles of attack and thus generate higher lift coefficients before stalling.

The shedding of a LEV after some stall delay is referred to as dynamic stall. To quote Corke and Thomas [13], "dynamic stall is an incredibly rich fluid dynamics problem that manifests itself on an airfoil during rapid, transient motion in which the angle of incidence surpasses the static stall limit." The event is further characterized by build-up and ejection of concentrated vorticity in the form of a coherent vortex, often of comparable length scale to the wing or structure that it is formed upon, which convects downstream. The delay in stall generates lift and moment coefficients in excess of their static counterparts, and leads to significant cycle hysteresis after the flow separates and the angle of attack is reduced.

It is well documented that the conditions preceding boundary layer separation strongly influence the inception and strength of the dynamic stall vortex (see McCroskey [76]). This causes the exact process to be largely stochastic. McAlister et al. [77] found that up to 50 cycles may be needed to yield converged statistics. Indeed, the dynamic stall event is highly sensitive to surface roughness and its influence on transition to turbulence, and effort has been given to quantifying this relation. For example, Bowles [78] concluded that sand paper strips were sufficient in eliminating the separation bubble on helicopter blades at Reynolds numbers up to $3,500,000$. As well, Carr and Chandrasekhara [79] forced transition on one-seventh scale helicopter blade models. Although the last study was largely focused on compressibility effects, the authors concluded that appropriate trip selection caused a delay of dynamic stall onset to higher angles of attack when compared to untripped foils, along with higher suction pressure coefficients. Contrary, incorrect choice of transition-induced trip led to significant degradation of airfoil dynamic stall performance. Still, a study on

the effect of boundary layer tripping at the current Reynolds numbers has not been completed to the current author's knowledge.

3.1.2 Oscillating-foil theory

While the governing theory of oscillating-foil turbines is presented thoroughly elsewhere (see references [18], [21]), a brief review is included here for discussion. The metrics used to assess turbine performance are the power coefficient, C_P, and the efficiency, η, defined as:

$$C_P = \frac{P}{(0.5\rho U_\infty^3 bc)}, \tag{3.1}$$

$$\eta = \frac{\bar{P}}{P_a}, \tag{3.2}$$

where P is the instantaneous power extracted, ρ is the fluid density, U_∞ is the freestream velocity, b is the foil span, and c is the foil chord length. Terms presented with overbars ($^-$) represent cycle-averaged quantities. The power available, P_a, is defined here as:

$$P_a = 0.5\rho U_\infty^3 bd, \tag{3.3}$$

representing the kinetic energy flux through the maximum extent of the window swept by all components of the oscillating-foil ($b \cdot d$), which is slightly larger than the full heave stroke of the foil as shown in Fig. 3.1. The reader should be cautious in comparing efficiency values found across literature, where other definitions may be used.

The prescribed pitch and heave motions of the foil are provided in equations (3.4) and (3.5), respectively.

$$\theta(t) = \theta_0 \sin(\gamma t), \tag{3.4}$$

$$H(t) = H_0 \sin(\gamma t + \phi). \tag{3.5}$$

Here, θ is the pitch position, θ_0 is the pitch amplitude, γ is the angular frequency,

t is time, H is the heave position, H_0 is the heave amplitude, and ϕ is the phase offset between pitch and heave motions. The instantaneous heave position is presented non-dimensionalized by its amplitude, as $H^* = H/H_0$. Similarly, the phase of the foil is presented relative to its position in the cycle as $t^* = t/T$, where T is the oscillation period. The oscillation frequency, f, is characterized by the reduced frequency, f^*, in equation (3.6).

$$f^* = fc/U_\infty \tag{3.6}$$

The motion of the foil in combination with the freestream flow impose an effective angle of attack on the foil, α, expressed here at the pitching center as:

$$\alpha(t) = \arctan[-V_y(t)/U_\infty] - \theta(t) \tag{3.7}$$

Here, V_y is the heave velocity. The effective angle of attack in Eq. 3.7 relies on a quasi-steady assumption to make predictions about the foil's relation to the flow. The effect of pitching velocity is neglected in this simple model, as well as any changes in angle of attack due to confinement effects and induction velocity associated with the turbine thrust on the incoming flow. However, this concept of effective angle of attack is useful in defining rough regimes of operation. In particular, the effective angle of attack is closely linked to the dynamic stall events, with larger effective angles being more likely to develop flow separation. The rate of change of angle of attack (defined in [18]), also influences stall dynamics, with higher rates having a larger Magnus effect and thus a higher tendency to suppress separation.

3.2 Methodology

3.2.1 Experimental system and techniques

The test apparatus consisted of five components: the water channel, the hydrofoil, the motion system, the force measurement system, and the PIV system. A schematic of the overall experimental system is provided in Fig. 3.2.

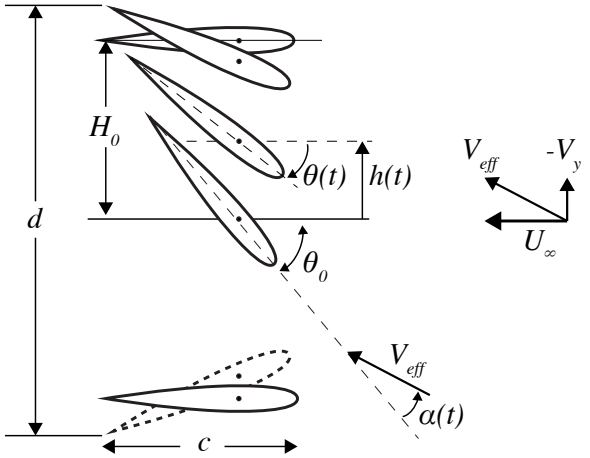

Figure 3.1: Diagram of heaving $h(t)$ and pitching $\theta(t)$ motions of an oscillating-foil turbine.

Water channel

The set of experiments was performed in a recirculating water channel with a test area cross section of 45 x 45 cm and a length of 250 cm. The test section of the flow channel was closed with a lid to eliminate unknown free surface effects and reduce surface reflections during the PIV image acquisition. The foil was rigidly mounted to a motion system with a straight shaft, which passed through a slot cut through the upper surface lid similar to the set-up by Heathcote and Gursul [80]. The water in the flow channel was filled 1 cm above the top of the slot to reduce air entrainment into the closed channel. The flow velocity was controlled to a resolution of $0.004\,m/s$, and was measured by PIV techniques. The ambient turbulence intensity of the flow was measured at $< 1\%$ for the range of velocities used.

The efficiency metrics, which are proportional to the cube of the freestream velocity, are sensitive to small changes in the measured inflow. The flow velocity was therefore measured for each condition ten chord lengths upstream of the foil, where the freestream was assumed not to be influence by the turbine. This was done to account for the changes in flow velocity within the water channel due to the resistance provided by the turbine, which varied with each case.

Foil parameters

A NACA 0015 foil section was used, with a chord length of $c = 50\,mm$ and a span of $b = 375\,mm$, yielding an aspect ratio (AR) of 7.5. The foil was positioned vertically in

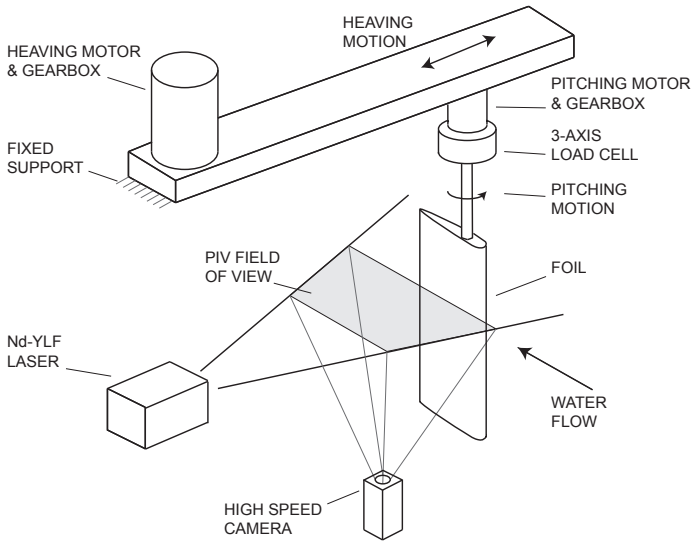

Figure 3.2: Schematic of the experimental configuration, showing the motion control, force measurement, and flow imaging systems.

the middle of the water channel. The pitching axis of the foil was 1/3 its chord length from the leading edge. The foil was constructed as a series of machined aluminum blocks, aligned with precision stainless steel pins and compressed by a central threaded steel shaft, as shown in Fig. 3.3. The aluminum pieces were anodized black to prevent corrosion and reduced reflections in PIV imaging. Endplates were sized such that the edges of the endplates were approximately 1/2 chord length outside from the edge of the foil, a sizing that Kim et al. [73] found to be suitable for minimizing tip losses.

Experiments were performed on both smooth, untripped foils, as well as foils where the boundary layer was tripped with surface roughness. Distributed surface roughness elements with a nominal height of $0.425\,mm$ were applied as a 3-mm-wide sandpaper strip at the location of the maximum thickness on both sides of the foil, along the entire span. The methods of Braslow and Knox [81] were used to quantify the roughness height required to promote transition under steady flow conditions under the lowest Reynolds number tested. However, this method did not address the unsteady motion of a flapping-foil, and the validity of its application was not known a priori; especially in the circumstance of an oscillating-foil that operates in deep dynamic stall throughout the bulk of a kinematic cycle.

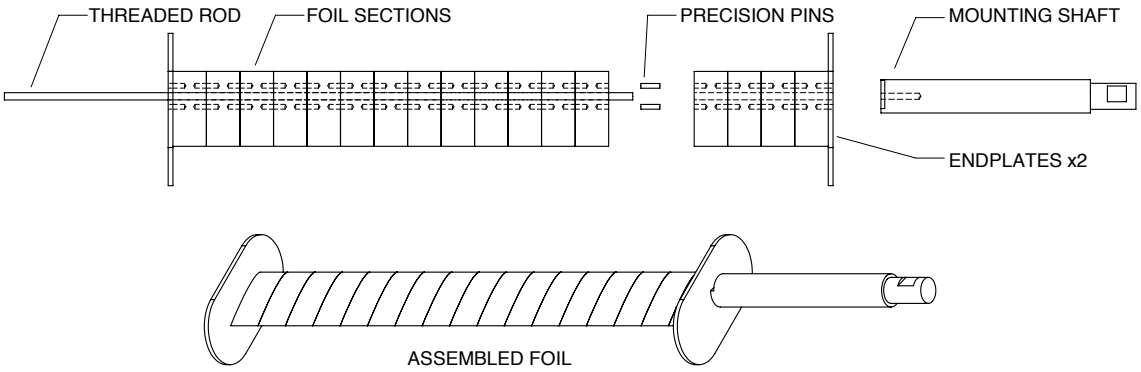

Figure 3.3: Assembly drawing showing the foil's construction.

Force measurements

Forces exerted on the foil were measured by a 3-axis load cell, which was positioned between the foil and the motion system, as was shown in Fig. 3.2. Torque about the pitching axis was measured, as well as forces normal and tangential to the chord direction which were decomposed into lift and drag forces with respect to the freestream direction. Forces were sampled at a frequency of 10kHz over the course of 20 oscillation cycles, and were filtered and averaged to produce a single mean cycle with an uncertainty below 0.8%. The factory load cell calibration was verified by applying known static loads to the sensor.

A suite of calibration experiments was performed for each kinematic condition that was tested to isolate the desired hydrodynamic forces required to assess turbine performance. Inertial forces were quantified by running the experimental motion profile in still air and assuming negligible fluid resistance. Hydrodynamic forces on the submerged mounting equipment were quantified by running the experiments with the foil removed, but the mounting shaft submerged to the correct depth. These measured forces were subsequently subtracted from the recorded test data, which allowed the hydrodynamic forces exerted only on the foil to be isolated. This approach allowed proper comparison with published numerical studies that did not consider the mass of the foil.

Quantitative flow imaging

Fluid velocity at the midspan of the foil was measured using high-speed particle image velocimetry. The flow was seeded with tracer particles with a mean diameter of $10\mu m$

that were illuminated by a pulsed Nd:YLF dual diode-pumped laser. Only one side of the foil was illuminated by the laser sheet. The images were processed with Davis LaVision 8.3 software using a multipass cross correlation technique [55]. The field of view of images was 113 mm x 113 mm, and the resolution of the image capture was 1024 x 1024 pixels. The smallest interrogation windows used were 12 x 12 pixels, yielding a resolution of 0.75 vectors/mm. As a result, the smallest structures that could be resolved from a grid of four vectors was 2.6 mm [82]. Phase-averaged images were calculated by averaging 150 instantaneous velocity fields corresponding to the same phase of the foil's oscillation.

The foil's endplates were removed during PIV image recordings to facilitate unobstructed image capture. An assumption was made that the flow structures at the midspan of the foil were not affected by removal of the endplates. This was justified by previous experimental work by Fenercioglu [83] and numerical work by Kinsey and Dumas [84] that indicated that end effects of foils of this aspect ratio do not significantly influence the midspan region, and that vortical structures are symmetric about the midspan.

3.2.2 Numerical techniques

XFOIL

The 2-dimensional viscid-inviscid panel method code XFOIL [85] was used to calculate hydrofoil lift values at static angles of attack. The NACA 0015 hydrofoil shape was discretized within the software into 150 panels, with refinement concentrated at the high curvature on the leading edge. This panel density and spacing also provided sufficient resolution in the regions of separation bubbles. The flow dynamics of a smooth, untripped foil were modelled by allowing the software to compute free transition via the envelope e^n transition criterion [86]. The n value needed to be empirically tuned to achieve similarity with the experimental results, where values from $n = 6$ to 9 were used. Rough, tripped foils were modelled within the software by forcing transition at the location of roughness.

3.3 Results

3.3.1 Static lift polars

The hydrofoil was initially tested at static angles of attack to observe the influence of the roughness elements on flow transition. The measured and the calculated values of the lift coefficient, C_L, as a function of the angle of attack, α, are provided in Fig. 3.4a and Fig. 3.4b for tests at $Re = 20,000$ and $Re = 30,000$. Data was sampled at 0.5° resolution near the stall point, and 1° elsewhere. Additionally, the angle of attack axes of the plots were adjusted up to ±0.25° to correct for misalignments in the system, such that zero angle of attack corresponded to zero lift.

The smooth foil in the experiments and the simulations showed negative values of lift coefficient at low angles of attack. This result may be attributed to the existence of a laminar separation bubble (LSB), which is discussed by Tank et al. [87]. The LSB was confirmed by dye visualizations in the experiments, and was also apparent in the XFOIL results as indicated by separation and reattachment points along the foils surfaces. At these low angles of attack, the LSB existed on upper and lower surfaces of the foil. At positive angles of attack, the separation point on the lower surface moved slightly rearward, while the separation point on the upper surface shifted forward. The net result was an effective camber yielding the peculiar negative lift. This effect has been seen in literature, for example in the work of Mueller and Batil [88], but in relatively few cases as historically this flow regime hasn't been a subject of interest. The increase in lift for the smooth foil above expected values in the range $3° < \alpha < 6°$ is also attributed to the movement of the LSB.

The numerical data for the smooth foil was highly sensitive to the choice of n value. It was possible to tune the numerical results to be similar to experiment results, however as shown in Fig. 3.4a, different n values yielded significantly different lift values. Further, the most suitable n value varied with Reynolds numbers. These trends highlight the sensitivity of foil performance to boundary layer transition in these moderate Reynolds numbers, and the associated difficulties in modelling transition events. The transition to turbulence at this Reynolds number is highly sensitive to external disturbances, including turbulence intensity, surface finish, and system vibrations [89]. It is thus non-trivial to make baseline comparisons between experiments and computations, where a variety of responses can be expected.

The coherence between experimental and numerical data was increased in the

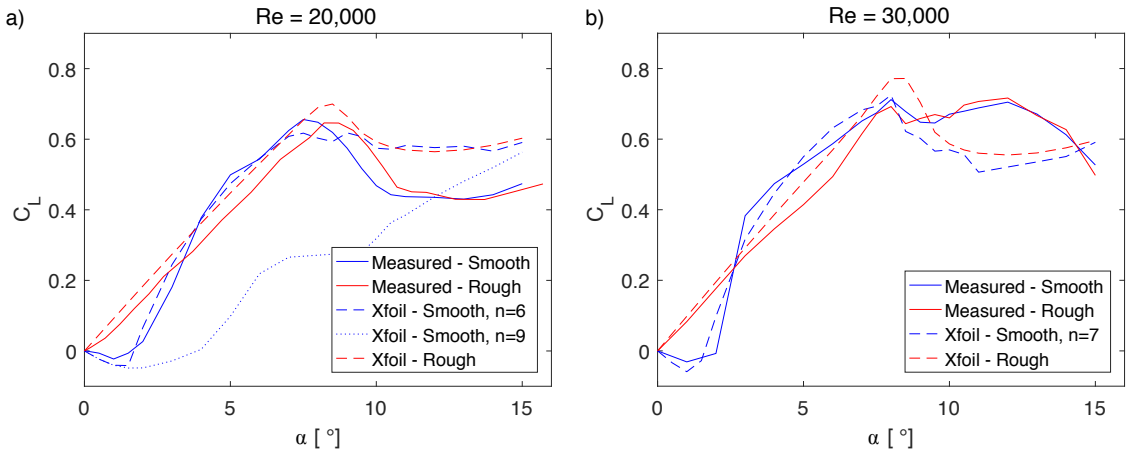

Figure 3.4: Static lift polars as a function of angle of attack. (a) at $Re = 20,000$. (b) at $Re = 30,000$.

cases of the tripped hydrofoils, where the numerical results were insensitive to the choice of n value. The development of a LSB was suppressed in both the experiments and the simulations, and the two approaches yielded good general agreement up to the stall point. A slight reduction in lift between the experimental (3D) and the numerical (2D) values was attributed to tip losses. At these Reynolds number the roughness elements did not increase the stall angle.

In Fig. 3.5a, showing tests at $Re = 35,000$, the signatures of the LSB were still apparent in the smooth cases, and agreement between smooth experimental and numerical results was still poor. For the experimental rough foil, the stall angle was increased by 3°, which indicated a transition to turbulence. This trend was confirmed at all Reynolds numbers above this value, as shown in Fig. 3.5b which provides experimental polars for rough foils at several Reynolds numbers. Even though a turbulent boundary was apparent at the higher tested Reynolds numbers, lift coefficients were lower than inviscid predictions for the same foil shape, which is used to approximate very large Reynolds number flows.

These results suggest that, by a quasi-static analysis, oscillating-foil turbines with untripped boundary layers at these Reynolds numbers would operate with laminar or transitional flow, while turbines with roughness elements of this size would develop turbulence if above $Re = 35,000$. In all Reynolds number tested, roughness elements eliminated the LSB, and are expected to improve accuracy of numerical simulations trying to represent these scales. Further, a reduction in lift is seen compared to an inviscid analysis, suggesting lower lift values than a high Reynolds number turbine.

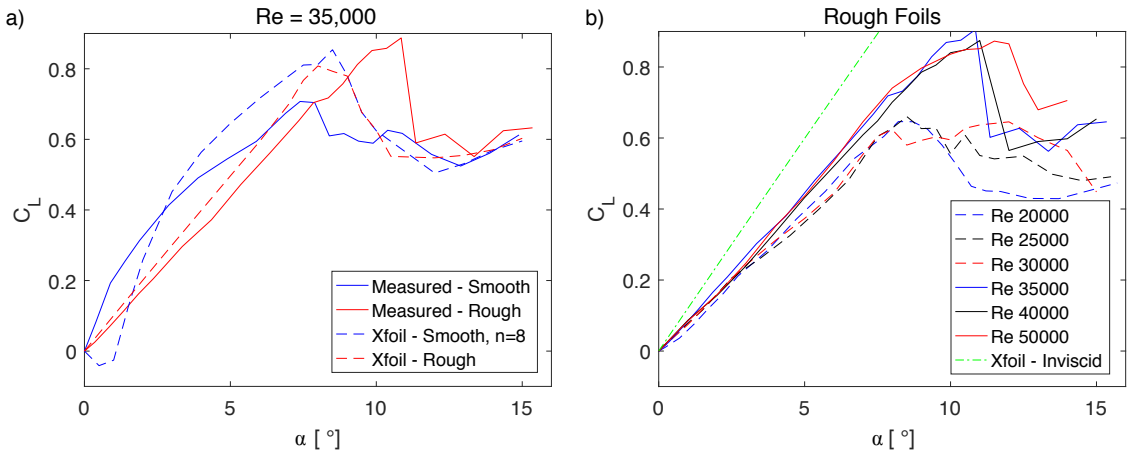

Figure 3.5: Static lift polars as a function of angle of attack. (a) at Re = 35,000. (b) at multiple Reynolds numbers, for experimental tripped foils only.

It is therefore unclear whether such turbines would have performance more similar to fully laminar conditions, or high Reynolds number turbulent conditions.

3.3.2 Turbine operation

Force measurements

The measured performance of the experimental oscillating-foil turbine, tested with motion amplitudes of $\theta_0 = 75°$ and $H_0/c = 1$, is presented Fig. 3.6. Efficiency, η, is provided as a function of the reduced frequency, f^*, for several tested Reynolds numbers of $Re = 20,000$, $30,000$, and $35,000$. The data showed no dependence on Reynolds number, although the difference between smooth and rough foils was notable. The presence of surface roughness resulted in an increase in efficiency of up to a 2.5% absolute, compared to the case of the smooth foil, with larger differences occurring at higher oscillation frequencies. The case of the rough foil at $Re = 35,000$, which previously showed a well-defined delay in static stall angle indicating a distinct turbulent boundary layer, surprisingly displayed no noticeable difference from the lower Reynolds number conditions. Rather, all Reynolds number cases performed similarly when oscillating; a consequence of the oscillating-foils operating at angles of attack well above static stall limits for the majority of a cycle.

The instantaneous power coefficient curve of the case $f^* = 0.14$ throughout the first half of a symmetrical oscillation cycle is provided in Fig. 3.6b. The exact topology of the power coefficient curves throughout a cycle varied for each reduced

frequency tested, in some cases significantly. However, the same dominant trends occurred in all cases. At the beginning of a cycle, power extraction increased approximately linearly with the increase in effective angle of attack while flow remained attached to the foil, as is characteristic of the dynamic stall process. Power extraction reached a maximum when the foil reached its peak effective angle of attack at the foil's midstroke, or near when the flow began to separate from the foil, whichever occurred first. The differences in data between smooth and rough foils in these portions of the cycle were minimal. However, this similarity diminished towards the end of each half cycle, at effective angles of attack near the static stall angle. It is believed that the dissimilarity occurred as a result of the roughness elements hastening the reattachment of flow to the foil by tripping the boundary layer and bypassing slow transitional effects occurring at these low angles of attack. However, this theory is not easily confirmed.

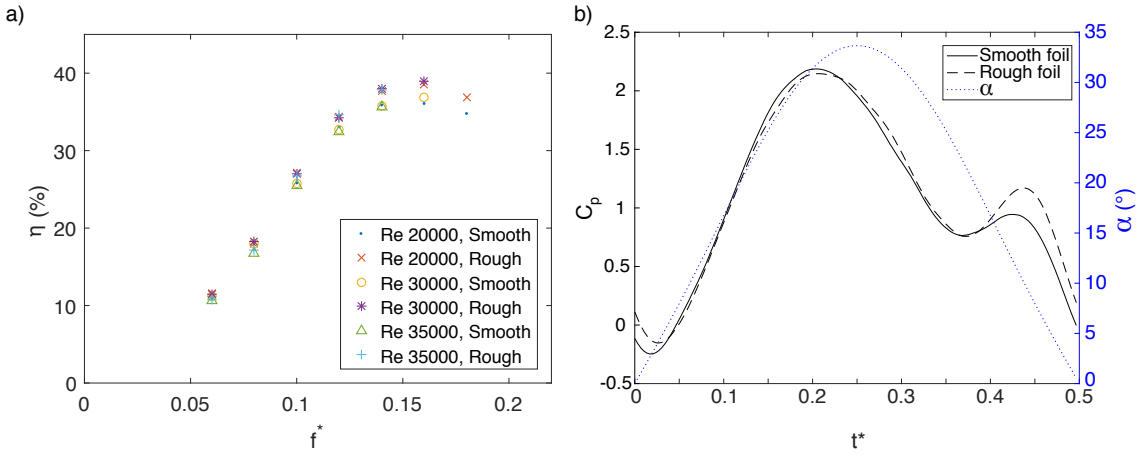

Figure 3.6: (a) Turbine efficiency as a function of reduced frequency for $\theta_0 = 75°$ and $H_0/c = 1$. (b) Instantaneous power extraction for the case $f^* = 0.14$.

It was hypothesized that flow separation was occurring upstream of the trip location, thereby circumventing its effect on transition. Additional experiments were therefore performed with roughness elements placed undoubtedly upstream of the separation point; one set of experiments with a thin strip of roughness at the leading edge, and a second set of experiments with a large strip extending from the leading edge back to the point of maximum thickness. These tests showed indiscernible differences from the standard roughness location choice, both in terms of the force measurements and the flow structures.

Quantitative flow imaging

PIV images of the flow field near the foil at different phases and operating conditions are provided in Fig. 3.7. The images show instantaneous velocity fields, selected arbitrarily from the larger image dataset collected for phase-averaging. The velocity fields have been processed with a high-pass Large-Eddy Simulation (LES) filter to aid in eddy-visualization [90], in which the translation of the larger-scale field have been removed while the small-scale turbulent eddies remain. During sections of the cycle where flow remained attached, the boundary layers were too thin to be fully resolved to determine if flow was laminar or turbulent, due to limitations in the PIV resolution and uncertainties from reflections at the foil's wall, and motion of the wall occurring between PIV image pairs. In separated regions, coherent structures were observed in the boundary layer and near wake of the foils [91]. This occurred for both smooth and rough foils, and even at the lower Reynolds number of 20,000.

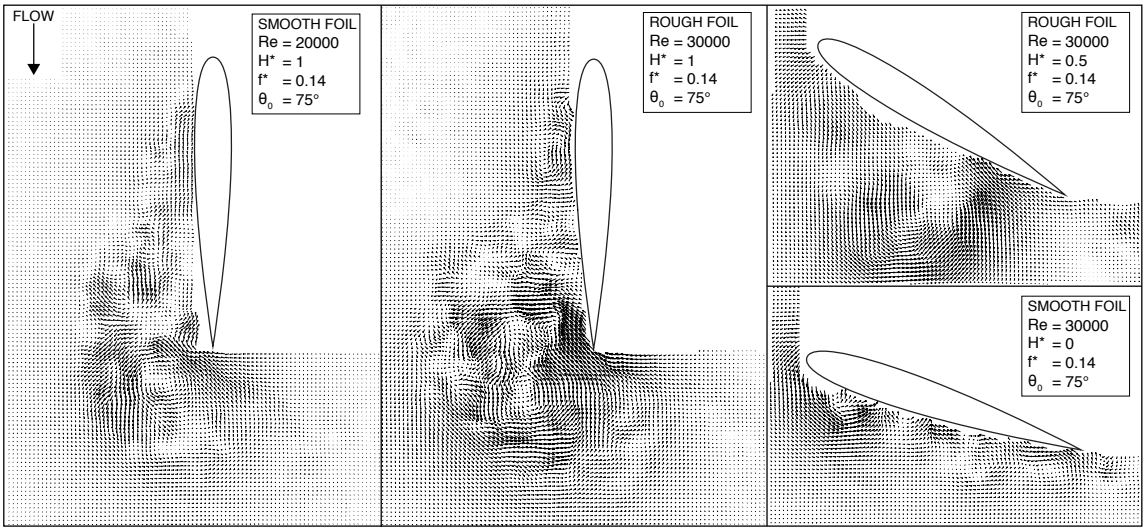

Figure 3.7: Instantaneous PIV images of the foil under four conditions, showing a LES-decomposed velocity field.

The exact separation dynamics and flow structures varied between cycles, so generalized trends should not be drawn from these images. Rather, they are used to observe and confirm the turbulent nature of the separated flow, which is an expected result. The primary leading edge vortex that developed ranged from a single tidy vortex to a more chaotic structure, depending on the cycle. Although the attached boundary layers were too thin to be optically resolved, the following can be inferred about the expected boundary layer dynamics. Static tests performed in Section 3.3.1

showed that at $Re = 35,000$ tripping the boundary layer produced turbulent flow, which would also be expected to occur when the foil oscillated. When the turbine was oscillating at the tested Reynolds numbers, force measurements showed negligible difference between smooth and rough foils during portions of the cycle when the boundary layer was known to be attached. It is reasonable to therefore suggest, with some certainty, that the attached boundary layers were turbulent regardless of the presence of an artificial trip throughout most of the cycle. The exception to this occurring near when the flow was reattaching after the stall event, as previously suggested.

Phase-averaged PIV images showing vorticity are provided in Fig. 3.8, recorded at $Re = 30,000$ for smooth and rough foils at $f^* = 0.08$ and $f^* = 0.14$. The figure also provides a kinematic diagram for phasing reference, showing the foil's motion through the freestream (not to scale). Development of dynamic stall is shown sequentially at instants $t^* = 2/8$, $3/8$, and $4/8$. At both frequencies, limited differences existed between flow structures of smooth and rough foils throughout the majority of the cycle, except near when the foil reached the extent of its heaving motion ($t^* = 0$ and 0.5). These observations were consistent with the instantaneous force profiles of the foil, where the only considerable differences occurred near when the flow reattached to the foils.

At the lower reduced frequency of $f^* = 0.08$, a LEV on the scale of the foils chord length had developed by phase $t^* = 2/8$. The LEV subsequently convected past the foils trailing edge and deep stall occurred before the foil reversed direction. In fact, a strong trailing edge vortex (TEV) was able to develop by phase $t^* = 3/8$.

The case of $f^* = 0.14$ exhibited a delayed onset of the dynamic stall due to the reduced effective angle of attack and the higher pitch rate stabilizing the boundary layer. By mid-stroke, the onset of dynamic stall had begun, but the LEV was at the initial stage of formation. The vortex continued to convect downstream, and its shedding was well timed with the reversal of the foil. Similar to the case of $f^* = 0.08$, the roughness elements had minimal influence except when the foil was reversing heave direction.

Comparison with numerical work

Experimental measurements were compared to the uRANS computational results available in published literature. Namely, comparisons were made against a study

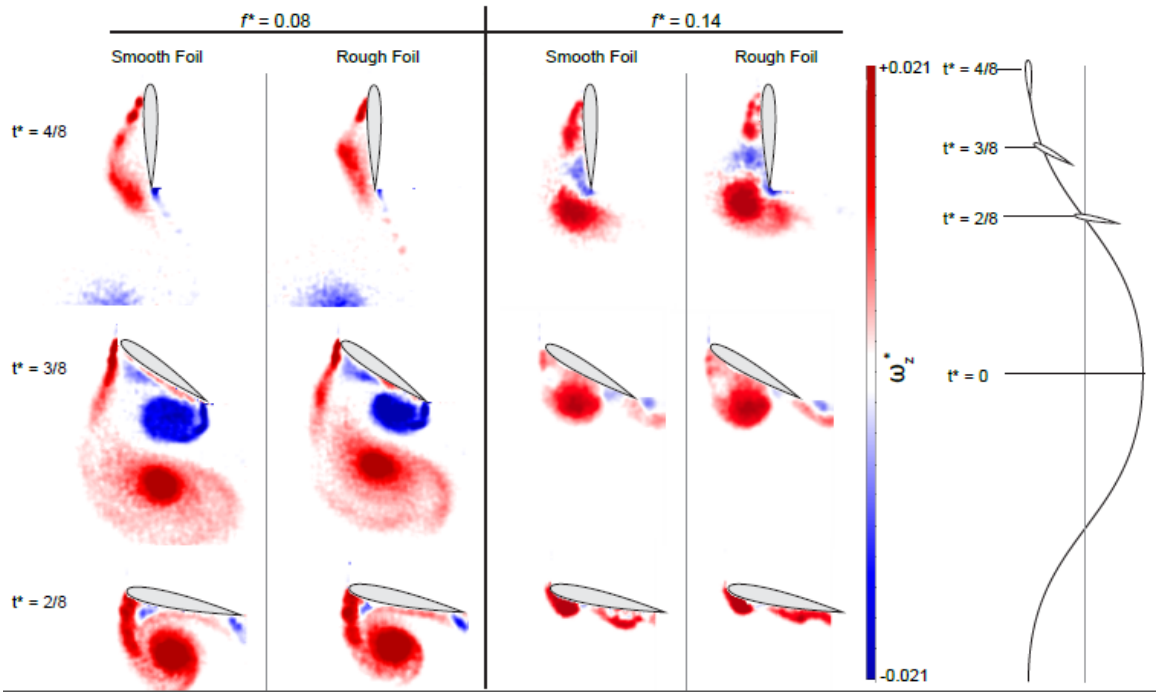

Figure 3.8: Phase-averaged out-of-plane vorticity in the near wake of the foil. Smooth and rough foils were tested at $f^* = 0.08$ and $f^* = 0.14$, under the conditions $\theta_0 = 75°$, $H_0/c = 1$, and $Re = 30,000$

at $Re = 1100$ by Kinsey and Dumas [11] representing purely laminar flow, and a study performed at $Re = 500,000$ by Kinsey and Dumas [18] representing a more practical operating regime with turbulent flow. The latter used the one-equation Spalart-Allmaras turbulence model with a modified strain/vorticity-based production term. Both cited works were performed with the same NACA 0015 foil shape and kinematics as the current study, although they were 2D in nature. The intent of the comparison was to see which flow conditions (lower Re or higher Re), the current experimental results were more similar to, for the purposes of assessing which flow regime the current transitional Reynolds number study aligned with.

Corrections were applied to the experimental force measurements to facilitate comparison with the published results of infinite aspect ratio, unconfined simulations. A correction for finite aspect ratio tip losses was drawn from the study of Kinsey and Dumas [84], who explicitly studied finite aspect ratio effects on oscillating-foil turbine systems. The nearest equivalent case tested by Kinsey and Dumas was a NACA 0015 foil with $AR = 7$ (current, $AR = 7.5$) and similar endplates, which had an efficiency equal to 86% of its 2D counterpart. This was therefore used to scale the experimental

results to an equivalent approximate '2D' result. In the following data sets, it is referred to as the '3D correction'.

A dissimilarity of channel confinement existed between numerical and experimental datasets. To facilitate a comparison between the two sets, blockage corrections were applied to the experimental work. The corrections followed the work of Gauthier et al. [52], who showed that the established BW blockage correction [53] is appropriate for oscillating-foil turbines under most conditions, and up to blockage ratios of $\sim 50\%$. The current experiments have blockage ratios, defined as the ratio of the turbine frontal swept area to the cross-sectional area of the channel, in the range of 22% to 32%, well within the proposed limits of the correction model. The blockage correction is derived from the conservation of mass, energy, and momentum on a control volume around the turbine. That is, it is not an empirical formulation, but rather one based in first principles. The value by which each experimental data point is scaled is determined from an iterative process which uses the measured drag on the turbine as an input. The full theory may be found in Appendix A of Ref. [52]

However, Gauthier et al. had observed that the correction was only applicable for oscillating-foil cases with $f^* > 0.10$. At lower reduced frequencies, the corrections became inaccurate. This suggested limit of applicability for the correction was empirically based on the existence of and the strength of a large-scale leading edge vortex that developed in these kinematic conditions. The authors proposed that conflicting confinement effects approximately cancelled each other for cases with massive separation. In these conditions, the channel confinement improved power extraction by increasing the available dynamic pressure, but the confinement also decreased performance by increasing perceived angles of attack and hastening flow separation. The matter of whether this was an artefact of the dataset, or a fundamental observation, is discussed shortly.

Fig. 3.9 compares the results of experimental tests of the rough, tripped foil at $Re = 20,000$ with the numerical works of Kinsey and Dumas [11],[18]. To show the relative influence of each correction method, each experimental data point is shown as only the raw data, with only the blockage correction applied, with only the 3d correction applied, and with both corrections applied. The desired comparison between experimental data and numerical data is found when the the 3d correction is applied for all data points, while the blockage correction is only applied when $f^* > 0.10$, as suggested by Gauthier et al. [52]. A trendline connecting these points, referred to hereafter as the 'delimited correction', is shown by the dashed black line

in the figures.

The experimental results with the delimited corrections yielded generally good agreement with the numerical results at $Re = 500,000$. In fact, these experimental values were in much closer alignment with the higher Reynolds number numerical study than they were in the lower Reynolds number study. The raw, uncorrected experimental data did not align directly with either numerical study, although a similar trend in terms of a rising then plateauing efficiency as a function of reduced frequency was maintained.

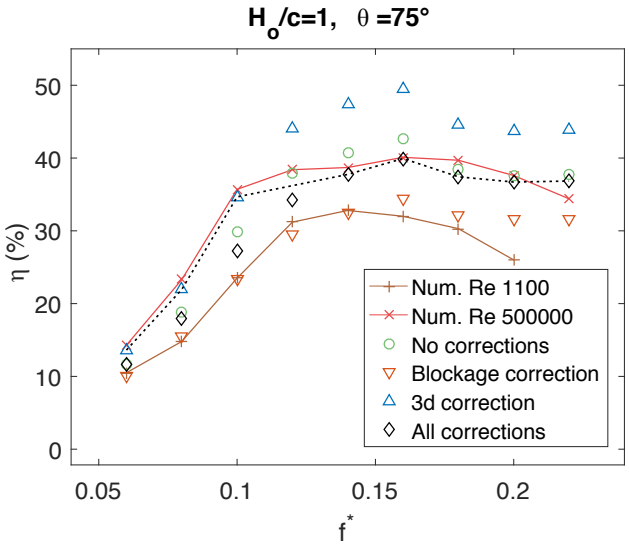

Figure 3.9: Turbine efficiency as a function of reduced frequency: experimental measurements at $Re = 20,000$ (rough foil) and numerical simulations at $Re = 1100$ [11] and $Re = 500,000$ [18]. The delimited correction is shown as the dashed line.

Similar conclusions were found when the heave amplitude was increased to $H_0 = 1.5c$, as shown in the plot of Fig. 3.10a. The line for the delimited corrections provided very close agreement with the matching high Reynolds number study, while the raw experimental data departed from this similarity. Fig. 3.10b provides a third dataset, this time recorded in a parametric space where $H_0 = 1c$, $f^* = 0.16$, and the pitch amplitude was varied from 60° to 90°. The corrected experiments and the numerical data were similar up to $\theta_0 = 80°$, but above this diverged somewhat. The divergence could be attributed to inaccuracies in the blockage correction model as a result of the deep dynamic stall at these high angles, inaccuracies in the numerical simulation, or perhaps another source of error not quantified in the experiments. At the higher range of pitch amplitudes in Fig. 3.10b, each experimental point showed a

large difference in efficiency when various corrections were applied. This was a direct result of very high drag values measured in these kinematics, which resulted in large blockage correction values.

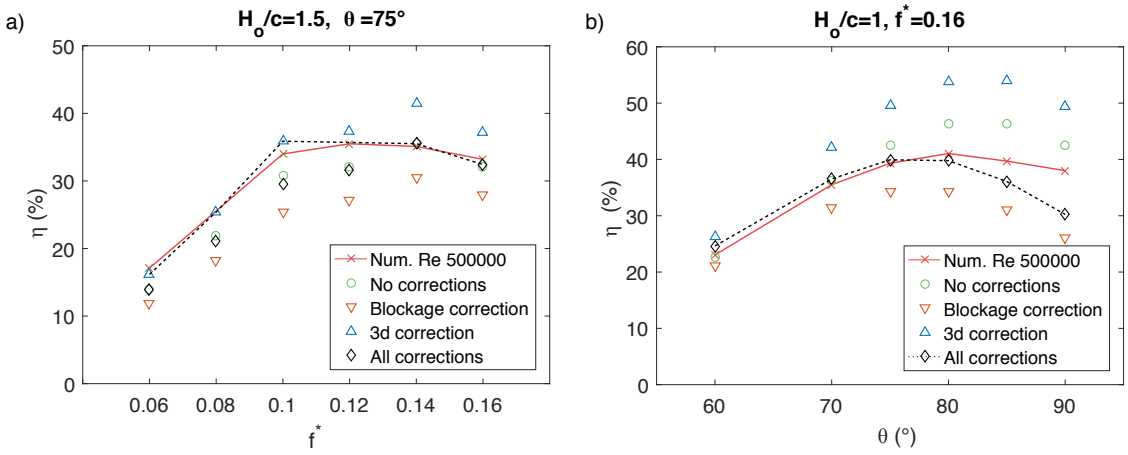

Figure 3.10: Turbine efficiency from experiments at $Re = 20,000$ on the rough foil. Numerical data is from [18]. The delimited correction is shown as the dashed line.

The current experiments have been promising in showing that there exists a similarity between moderate scale experiments and higher Reynolds number operating environments. However, it is worth briefly discussing the uncertainties associated with the blockage correction method. Particularly, the range of applicability used in the present work, and that of Gauthier et al. [52], is vaguely defined and should currently be applied in future work with caution. The hypothesis that the dynamic stall vortex, or lack thereof, plays a prominent role in the fidelity of the correction is likely true. However, while it is likely that the dynamic stall vortex is an indicator of performance changes, the changes themselves could be the result of something more fundamental.

It is worth recalling that the reduced frequency, in combination with the heave amplitude and pitch amplitude, define the effective angle of attack of the foil (at least in a quasi-static sense). The proximity of the channel walls to the turbine's foil also changes the effective angle of attack; a result of alterations to the immediate flow field due to the confinement. In this sense, these changes in angle of attack due to channel confinement would need to be reflected in the parametric space of η vs. f^* by correcting the reduced frequency. In the present work, correcting the reduced frequency by the methods suggested by Gauthier et al. [52] did not improve the correlation of data in the troublesome $f^* < 0.10$ range (it is noted that the

data previously shown was without reduced frequency corrections). However, it is suggested here that scaling a non-dimensional effective angle of attack would be more fundamental and could lead to more accurate results, but the approach to do this is unclear.

While the inaccuracies of the blockage corrections are most influential in off-design conditions, which are not necessarily of high interest or consequence, understanding the fundamental mechanisms changing the performance could aid in understanding and improving the performance of these turbines. Further, as the oscillating-foil turbine research community is showing interest in designing fully-passive systems, where the turbine's dynamics are unconstrained and develop freely from the fluid-structure interaction of the flow and the foil, it may become important to understand these fundamental blockage effects. An example of this type of turbine is found in the recent work by Boudreau [20].

3.4 Conclusion

The nuances associated with transitional Reynolds number flow situations are well known, but not fully understood. The particular application of transitional Reynolds number oscillating-foil turbines has been explored within the present work. The study was motivated by physical scale limitations associated with typical experimental facilities, coupled with the previous observation that oscillating-foil turbines exhibit different performances under laminar and turbulent conditions. The current experiments have been promising in showing that there exists a similarity between moderate scale experiments, and higher Reynolds number scenarios.

A NACA 0015 hydrofoil with an aspect ratio of 7.5 was first tested at static angles of attack in the Reynolds number range of 20,000 to 50,000. There, the foils were highly sensitive to both Reynolds number and surface roughness. Smooth foils developed a laminar separation bubble on both suction and pressure surfaces, leading to irregularities and non-linearities in generated lift values. Numerically reproducing these events was possible, but required empirically tuning modelling constants. Tripping the boundary layers with distributed surface roughness elements located at the position of maximum foil thickness proved to be sufficient in eliminating these transitional effects, and made the agreement between experimental and numerical values more reliable. Above $Re = 35,000$, the roughness elements delayed the static stall angles by several degrees, indicating successful turbulence generation.

When the foil dynamically oscillated, with kinematics appropriate for energy-extraction, its efficiency was independent to the Reynolds number range tested but had light sensitivity to boundary layer tripping. This contradicted the previous quasi-static predictions, reiterating the complexity of the dynamic system. Tripping the boundary layers had only a small impact on cycle averaged efficiency, showing up to a 2% increase in energy-extraction efficiency, but this increased the similarity with higher Reynolds number studies ($Re = 500,000$).

Experiments with confined turbines can be made representative of turbines in generalized, unconfined environments with the use of appropriate correction techniques. The common BW blockage correction model was used within. This approach, although seemingly accurate in some instances, does not have a conclusive range of applicability. It proposed that in future work, this range of applicability be studied from a fundamental perspective.

Chapter 4

Reliability Study of a Fully-Passive Oscillating-Foil Turbine Concept

Abstract

A fully-passive oscillating-foil hydrokinetic turbine was experimentally tested with the intent of assessing its sensitivity to various disturbances. The physical prototype consisted of a two degree of freedom elastically-mounted wing which developed useful, self-sustained, and flow-induced oscillations capable of good power extraction. The turbine did not have an active control strategy, and the pitch and heave motions were not constrained or mechanically linked. Rather, stall flutter was the driving mechanism leading to stable limit-cycle oscillations. While this benefits the system in terms of reductions in cost and mechanical energy loss, it potentially reduces reliability of the device when operating in environments outside of the uniform steady flow for which it was designed. The enclosed campaign therefore subjected the prototype to disturbances in the form of high freestream turbulence intensities, artificial boundary layer tripping via surface roughness, and periodic perturbations from an upstream oscillating-foil turbine. Good performance was maintained in most situations, while energy extraction surprisingly increased in some instances. These results help confirm the potential of the new technology.

4.1 Introduction

The need for renewable energy sources to offset or replace fossil-fuel sources is now generally recognized. However, in an economic-based society, renewable energies often struggle to be cost-competitive, and in some cases suffer from unreliable and intermittent energy supplies [92]. The use of oscillating-foils for hydrokinetic energy harvesting has been receiving interest in recent years, promising to overcome some of these setbacks and supplement other energy supplies. These systems consist of a foil, or wing, that translates and rotates in a cyclic and periodic manner. These lift-based devices have been shown to reach energy extraction efficiencies matching or exceeding their traditional rotary counterparts. An additional benefit worthy of note is the untwisted foil geometries which are not subject to centrifugal stresses, allowing simple construction. Further, oscillating-foil turbines are particularly well-suited for shallow and wide flow channels, where their rectangular cross-sections can capture large portions of the flow, and they can operate efficiently in slower flows than conventional rotary designs [93] [94]. Thorough examinations of the oscillating-foil turbine concept have been presented in reviews by Young et al. [21] and Xiao and Zhu [56].

Although oscillating-foil systems have shown great potential in laboratory settings and numerical campaigns, industrial adoption of such technologies has been low and largely unsuccessful. Examples include the Stingray turbine, designed by the Engineering Business Ltd. [95], which was deemed economically non-viable after preliminary testing, and a prototype by Pulse Tidal Ltd., which also performed poorly. These unsuccessful results follow from the necessity to provide the system with appropriate kinematics, which at the time, were not adequately understood or characterized. The state of the art in the subject has developed considerably since these early designs, following the works of multiple research groups internationally, which encourages renewed efforts.

An additional underlying impairment of many existing efforts to design oscillating-foil turbines is the mechanical complexities associated with prescribing the suitable pitch and heave kinematics, where typically some mechanical means has been used to control or constrain the motion of the foil. As well, many early designs have suffered from complex or crude power transmission mechanisms, leading to high energy losses. For example, Kinsey et al. [19] developed a tandem foil prototype, where the pitch and heave motions were mechanically coupled to create a one degree of freedom system, and a four-bar linkage system was used to convert the heave motion to rotary

motion for the power take-off. The authors found that approximately 25% of the power harvested by the wings, in some cases more, was lost to friction within the system. This complexity also leads to a lack of robustness and high maintenance, which is a significant issue in terms of practical implementation. Some researchers have thus turned to systems that do not rely on complex mechanisms to kinematically constrain or prescribe the motion of the foil, creating so-called fully-passive systems. Here, the motion of the foil is self-induced and self-sustained through the structure's interactions with the fluid, and the two degrees of freedom are not mechanically coupled. That is, the motion is not mechanically constrained or prescribed in any manner. This concept, and its development, is discussed briefly in the following.

It is first important to recall that parametric studies by Kinsey and Dumas [11] [18], and many others, have emphasized the importance of a properly coupling pitch (rotating) and heave (translating) motions in the two degree of freedom system. Indeed, well prescribed kinematics can result in efficiencies as high as 43% [18]. The coupling of motions may be achieved by several means. Explicit control strategies for motion profiles, amplitudes, frequencies and phase lag can be applied to each degree of freedom independently, by direct use of motors. Alternatively, mechanical coupling may be employed to kinematically reduce the system to a single degree of freedom. The motion of single degree of freedom systems can be prescribed, or allowed to oscillate naturally in a flow field, but are still considered constrained systems.

Semi-passive systems, in which the pitching motion is prescribed while the heave motion is unconstrained, have been proposed by several research groups and exhibit reasonable efficiencies [67] [68] [73] [96] [97] [98] [99] [100] [101] [102] [103]. Semi-passive systems of this nature do not require linkages between degrees of freedom, but do require a generator/motor to be attached to the pitching system, in addition to the generator attached to the heave system. It has been shown by Kinsey and Dumas [18] and Zhu [104], however, that the contribution of energy generated by the pitch motion is insignificant in most cases. It is thus sensible to neglect the need for and expense of a pitch motor at the sacrifice of a small drop in overall efficiency.

Semi-passive concepts where the heave motion is prescribed, but pitch is not, have recently been numerically investigated by Boudreau et al. [105]. The motivation for such a design spawns from the idea that a generator is invariably connected to the heave motion for power take-off, and that such a generator may in some portions of a cycle act as a motor to control the heave motion and modify the system's kinematics. The first look at this concept has shown promise, with the turbine reaching efficiencies

up to 45.4%, and provokes further interest.

A simple concept for a fully-passive system has been proposed by Poirel et al. [66], [106], and expanded upon by Veilleux [107]. The concept involves a wing that is elastically mounted in pitch and in heave. The system has no mechanical coupling between degrees of freedom, and no active control system. Instead, the motion of the foil develops freely from the interaction between the flow and the elastic structure to which it is mounted. The design relies on non-linearities in the flow to limit the motion, resulting in self-sustained, limit-cycle oscillations. Specifically, periodic dynamic stalling occurs on the suction side of the foil, resulting in a large leading edge vortex that is shed each half cycle as the foil reverses heave direction. The difficulty of such designs resides in tuning the structural parameters to yield desirable kinematics. Other flutter and limit-cycle oscillation based technologies have been studied by various researchers, including those in references [108] [109] [110] [111] [112] [113] [114], although such systems have not developed the range of kinematics or energy extraction levels associated with peak performance highlighted in the current context.

Boudreau et al. [20] developed a prototype of this style of fully-passive concept based off the optimization performed by Veilleux and Dumas [107], and performed an experimental campaign examining its performance. The results were promising, showing up to 31% efficiency, and the foil reached stable high amplitude motions within a few cycles of being released from equilibrium. This prototype is used as the basis of the current study, and is described in further detail in Section 4.2.1.

By nature of the design, this fully-passive concept relies on a two-way coupled fluid-structure interaction to develop motion profiles leading to useful energy extraction. This leads to a question of how sensitive these designs may be to disturbances in the flow field, where certain flow perturbations may significantly alter the motion of the wing. These designs have no fail-safe for motion, with the exception of physical hard-limits preventing excessive motion amplitudes. Therefore, there is no guarantee that stable and useful motions will develop, or that the system will not get 'stuck' in a motionless equilibrium state.

The current study tests a fully-passive concept experimentally under distinct sets of prescribed flow conditions. These include periodic perturbations from an upstream oscillating foil, high freestream turbulence intensities, and the application of surface roughness elements to the foil's surface. The work intends to provide a baseline to assess the robustness and reliability of the novel technology in *simulated* real-world

environments.

The intention of the study is not to claim that the enclosed experiments are fully representative of generalized, real world operation. The specific conditions in which the experiments are tested may never be realized in the real world. However, the results are useful in assessing the sensitivity of such a design to various disturbances and different inflow environments, of the type which may be similar to those occurring in practical operating environments. The study is performed experimentally, rather than numerically, as the effects of freestream turbulence, transition to turbulence in the boundary layer, and wake dissipation or recovery several chord lengths downstream of the foil, are difficult to accurately model or fully resolve with numerical methods, and come with high computational expense.

4.2 Experimental System

The design of the fully-passive prototype, and the methodology used in its experiments are described in this section. Additional details specific to each subset of experiments are presented later in the appropriate sections.

4.2.1 Fully-passive prototype

The fully-passive turbine in the current campaign is the same physical prototype used in the study by Boudreau et al. [20]. It is strongly suggested that the reader of this manuscript familiarize themselves with this previous work for the full details of the fully-passive design. Only the key parameters of the design are repeated here, out of necessity and for discussion.

A schematic of the two degree of freedom turbine system is shown in Fig. 4.1. The NACA 0015 foil of chord length c is constrained to move only in a linear heave motion ($h(t)$), and a rotational pitch motion ($\theta(t)$) about its pitching axis, located a distance x_p from the leading edge. Both degrees of freedom are elastically mounted, with spring stiffnesses for heave and pitch of k_h and k_θ, respectively. Further, a linear damping is applied independently to the heave and pitch degrees of freedom with values D_h and D_θ, respectively. The sources of damping in the system, which consists of a desirable energy sink used to replicate power take off, and unavoidable friction losses, are discussed in more detail in the following subsection.

An image of the prototype installed in the water channel in which it operated is

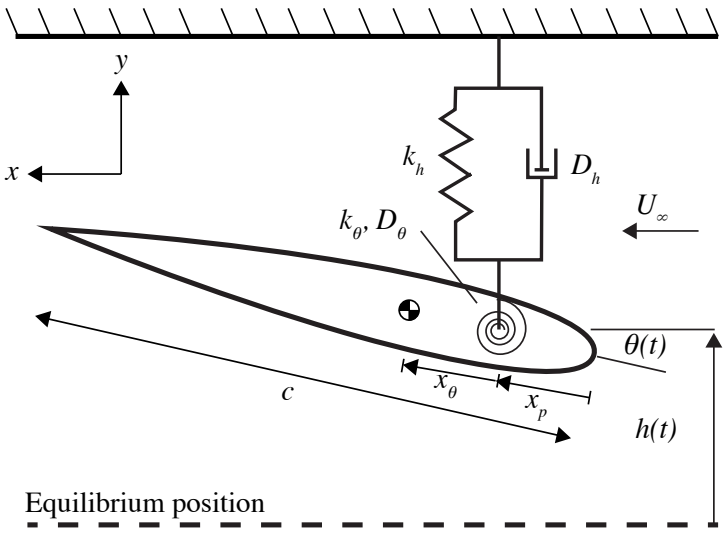

Figure 4.1: Simplified schematic of the fully-passive turbine

provided in Fig. 4.2. The prototype was constructed in a modular manner, allowing many discrete changes to independent variables to be made, facilitating the previous parametric study [20]. In the image, flow is from right to left. The foil was mounted vertically and centrally in the channel. The foil was mounted onto a heave carriage, which itself ran along a linear rail to guide the heave motion. The linear heave position was measured by a rotary encoder, which was connected to the heave carriage by a rack and pinion connection. The heave carriage was connected to several spring mounts, allowing the heave stiffness to be varied by altering the number and stiffness of springs used. An eddy-current brake, seen on the left of the image, provides a linear energy sink used to model power extraction. The brake resistance was controllable, as described in further detail on page 65.

No mechanical coupling is present between degrees of freedom. That is, the heave motion moves freely and independently of the pitch motion, and vice versa. However, it is noted that an inertial coupling between the two degrees of freedom exists, which becomes apparent in the equations of motion, discussed next. A coupling in the hydrodynamic lift force and hydrodynamic moment also relates the degrees of freedom, and is largely responsible for the self-sustained and periodic motions that the turbine develops.

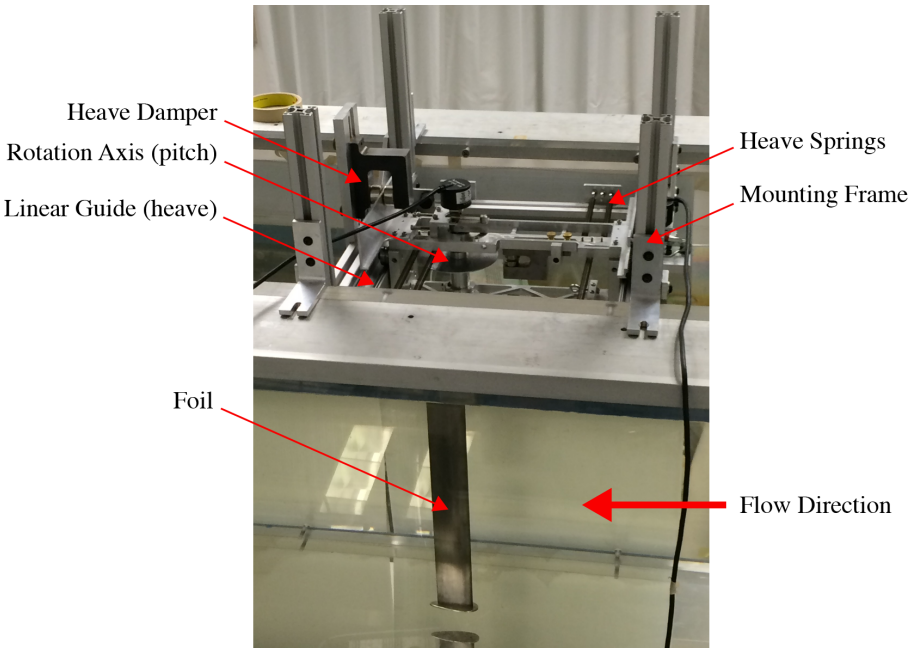

Figure 4.2: View of the turbine prototype installed in the water channel. Water flow is from right to left.

Governing Equations

The governing equations of the turbine system are provided in dimensionless form in Equations 4.1a and 4.1b for the heave and pitch degrees of freedom, respectively. The derivation for the equations may be found in the thesis of Veilleux [115], which follows a Lagrange-type approach. The superscript $(\dot{})$ signifies terms differentiated with respect to time, and $(\ddot{})$ signifies terms twice differentiated. Each equation of motion consists of a hydrodynamic term, inertial term, inertial coupling term, structural terms (damping and spring), and Coulomb friction term.

$$
\begin{aligned}
C_{F_y}/2 &= m_h^* \ddot{h}^* + S^* \left(\ddot{\theta}^* \cos\theta - \dot{\theta}^{*\,2} \sin\theta \right) + D_h^* \dot{h}^* + k_h^* h^* + C_{F_y\ \mathrm{Coulomb}}/2, \quad (a) \\
\underbrace{C_M/2}_{\text{hydrodynamic}} &= \underbrace{I_\theta^* \ddot{\theta}^*}_{\text{inertial}} + \underbrace{S^* \ddot{h}^* \cos\theta}_{\text{inertial coupling}} + \underbrace{D_\theta^* \dot{\theta}^* + k_\theta^* \theta}_{\text{structural}} + \underbrace{C_{M\ \mathrm{Coulomb}}/2}_{\text{Coulomb friction}}, \quad (b)
\end{aligned}
\tag{4.1}
$$

The terms appearing in Equations 4.1a and 4.1b are expanded further in Equations 4.2 through 4.6, and the details of each variable are expressed in Table 4.1.

$$C_{F_y} = \frac{F_y}{0.5\,\rho\,U_\infty^2\,b\,c}\ , \qquad C_{F_y\ \text{Coulomb}} = \frac{F_{y\ \text{Coulomb}}}{0.5\,\rho\,U_\infty^2\,b\,c}\ , \tag{4.2}$$

$$C_M = \frac{M}{0.5\,\rho\,U_\infty^2\,b\,c^2}\ , \qquad C_{M\ \text{Coulomb}} = \frac{M_{\ \text{Coulomb}}}{0.5\,\rho\,U_\infty^2\,b\,c^2}\ , \tag{4.3}$$

$$m_h^* = \frac{m_h}{\rho\,b\,c^2}\ , \quad I_\theta^* = \frac{I_\theta}{\rho\,b\,c^4}\ , \quad S^* = \frac{S}{\rho\,b\,c^3}\ , \tag{4.4}$$

$$D_h^* = \frac{D_h}{\rho\,U_\infty\,b\,c}\ , \quad D_\theta^* = \frac{D_\theta}{\rho\,U_\infty\,b\,c^3}\ , \quad k_h^* = \frac{k_h}{\rho\,U_\infty^2\,b}\ , \quad k_\theta^* = \frac{k_\theta}{\rho\,U_\infty^2\,b\,c^2}\ , \tag{4.5}$$

$$h^* = \frac{h}{c}\ , \quad \dot{h}^* = \frac{\dot{h}}{U_\infty}\ , \quad \ddot{h}^* = \frac{\ddot{h}\,c}{U_\infty^2}\ , \quad \dot{\theta}^* = \frac{\dot{\theta}\,c}{U_\infty}\ , \quad \ddot{\theta}^* = \frac{\ddot{\theta}\,c^2}{U_\infty^2}\ . \tag{4.6}$$

As aforementioned, it is important to note that there is no mechanical coupling between pitch and heave; the motions can move independently and freely. However, analysis of the governing equations reveals that the static moment, S, exists in both equations, and provides an inertial coupling.

The static moment is defined as the product of the pitching mass and the distance between the pitch axis and center of pitch mass. Mathematically, this is expressed as $S = m_p x_\theta$. This product provides a coupling only present when the foil accelerates in either degree of freedom, provided the pitching axis does not coincide with the center of the pitching mass. This creates an important tuning parameter, discussed at length in the work of Veilleux [107] [115]. There, the static moment is highlighted as a critical parameter for classical flutter operation. Classical flutter (often referred to simply as flutter) is an oscillatory, dynamic instability predicted by potential flow theory. The onset and dynamics of classical flutter is also influenced by the relative positions of the elastic axis, of the aerodynamic center, of the center of mass, and the ratio of natural frequencies between degrees of freedom. Importantly, it is noted that classical flutter is the result of negative aerodynamic damping that arises from a well-defined coupling between modes.

The current prototype, however, has been designed and optimized to exploit stall flutter as the primary driving mechanism, which results in well-behaved and repeatable oscillations. In the context of stall flutter, although a structural coupling between degrees of freedom may exist and influence the system dynamics, it is not an essential feature. Rather, in stall flutter the negative aerodynamic damping is due to the

Table 4.1: List of the parameters involved in the equations of motion, adapted from reference [20].

Symbol	Units	Definition
b	[m]	Blade span length
c	[m]	Chord length
ρ	[Kg/m^3]	Water density
U_∞	[m/s]	Freestream velocity
h	[m]	Heave position of the pitch axis (upward positive in Fig. 4.1)
θ	[rad]	Pitch angle (clockwise positive in Fig. 4.1)
t	[s]	Time
x_p	[m]	Distance between the leading edge and the pitch axis
x_θ	[m]	Distance between the pitch axis and the center of mass (defined positive when the pitch axis is upstream of the center of mass)
F_y	[N]	Hydrodynamic force component in the heave (y) direction
M	[N·m]	Hydrodynamic moment about the pitch axis
$F_{y\ \mathrm{Coulomb}}$	[N]	Coulomb friction force component in the heave (y) direction
$M_{\ \mathrm{Coulomb}}$	[N·m]	Coulomb friction moment about the pitch axis
m_h	[Kg]	Mass of all the components undergoing the heaving motion
I_θ	[Kg·m^2]	Moment of inertia about the pitch axis
S	[Kg·m]	Static moment (mass of the components only undergoing the pitching motion times x_θ)
D_h	[N·s/m]	Total linear heave damping coefficient
$D_{h,\mathrm{e}}$	[N·s/m]	Linear heave damping coefficient of the eddy-current brake (desired energy sink)
$D_{h,\mathrm{v}}$	[N·s/m]	Linear heave damping coefficient of the heave bearings
D_θ	[N·m·s/rad]	Linear pitch damping coefficient of the pitch bearings
k_h	[N/m]	Heave stiffness coefficient
k_θ	[N·m/rad]	Pitch stiffness coefficient

hysteresis in the aerodynamic forces and the phase lag between the motion and the forces. Boudreau [20] confirmed that the physical prototype indeed relies primarily on stall flutter/divergence by observing that when preventing heave motion, stable and high-amplitude pitch oscillations developed, indicating that inertial coupling was not fundamental to the motion.

The fully-passive prototype is further characterized by a divergence phenomenon [116], where the elastic restoring moment is sufficiently small to allow the pitch motion to strictly diverge from the equilibrium position under sufficient loading; i.e., above a critical velocity. The energy transfer from flow to structure is limited by non-linearities in the hydrodynamic forces, which develop as the result of deep dynamic stall. The motion that develops results in limit-cycle oscillations (LCO), which are self-excited, cyclic oscillations of limited and fairly consistent amplitudes [117].

Damping and power take-off

Damping was present in the system in the forms of linear viscous damping in the bearings, Coulomb friction in the bearings, and eddy-current braking. Each of the noted sources of damping in the bearings was present in both heave and pitch degrees of freedom, while an eddy brake was used only in heave. The summation of the total linear damping coefficients in heave and pitch are provided in Equations 4.7 and 4.8, respectively. As aforementioned, no eddy brake was used in pitch throughout the experiments as it was observed that even small levels of added damping yielded erratic, low amplitude motions. This result was a consequence of the fact that the cycle-averaged energy output of the pitch degree of freedom was near zero. Small additions of damping in rotation caused the net energy in this degree of freedom to become negative, and therefore the pitch motion could not drive itself and full-amplitude motion was not sustained.

$$D_h = D_{h,\mathrm{e}} + D_{h,\mathrm{v}} \ , \tag{4.7}$$

$$D_\theta = D_{\theta,\mathrm{v}} \ . \tag{4.8}$$

Other sources of damping, such as aerodynamic drag of the turbine's structural

components mounted above the water level, and hydrodynamic drag on the submerged portion of the mounting shaft, were assumed negligible and have been neglected in this analysis. The damping terms associated with the bearings were experimentally determined by a series of free-decay tests. There, one degree of freedom was fixed while the other was displaced from its equilibrium position. Following the displacement, the system was released and the single degree of freedom oscillated until the motion decayed and reached an equilibrium state. This allowed a determination of the damping terms, via the methodology outline in Appendix B of reference [20], which follows the procedure decribed by Feeny and Liang [118]. The bearing damping and frictions were not used directly in the prediction of power extraction efficiencies, but rather were used to quantify additional losses in the system.

The primary energy sink used to quantify power extraction was the eddy-current brake in the heave degree of freedom. The eddy-current brake in the heave axis consisted of a thin aluminum sheet fixed to the prototype's heave carriage, which passed through a narrow magnetic yoke. The relative position of the magnetic yoke to the aluminum plate was adjustable, allowing the amount of damping to be varied. Once more, further details of this design and calibration may be found in reference [20]. Similar designs have been employed in the works of Abiru and Yoshitake [67] [119], and Pigolotti et al. [120], which may interest the reader.

Measurement of the rate at which the aluminum plate passed through the yoke, and knowledge of the calibrated damping value for the yoke's position, allowed the power extraction to be calculated. The estimate for power extraction from the heave motion through the eddy-current brake for a single cycle, $\overline{P_{h,e\,j}}$, was computed as:

$$\overline{P_{h,e\,j}} = \frac{1}{T_j}\int_{t}^{t+T_j} (D_{h,e}\dot{h}^2)dt, \tag{4.9}$$

where T is the oscillation period, the subscript j denotes values from the jth cycle, and other values are listed in Table 4.1. Following, the cycle-averaged efficiency, $\eta_{e\,j}$, and power coefficient, $\overline{C_{P_{h,e\,j}}}$, were computed as:

$$\eta_{\mathrm{e}\,j} = \frac{\overline{P_{h,\mathrm{e}\,j}}}{\frac{1}{2}\,\rho\,U_\infty^3\,b\,d_j}\ , \tag{4.10}$$

$$\overline{C_{P_{h,\mathrm{e}\,j}}} = \eta_{,\mathrm{e}\,j}\,\frac{d_j}{c}. \tag{4.11}$$

Other metrics used in the present work to define performance are the reduced frequency, f^*, phase lag between heave and pitch motions, ϕ, heave amplitude, H_0^*, and pitch amplitude, θ_0, as defined in Equations 4.12 through 4.15

$$f_j^* = \frac{f_j\, c}{U_\infty}\ , \tag{4.12}$$

$$\phi_j = \frac{360^\circ}{T_j}\left(t_{\theta_{\max\, j}} - t_{h_{\max\, j}}\right) \quad , \tag{4.13}$$

$$H_{0\,j}^* = \frac{h_{\max\, j} - h_{\min\, j}}{2c}\ , \tag{4.14}$$

$$\theta_{0\,j} = \frac{\theta_{\max\, j} - \theta_{\min\, j}}{2}\ . \tag{4.15}$$

All values for the previously defined metrics that are presented hereafter have been averaged over 90 oscillation cycles to yield converged statistics.

4.2.2 Flow facility

The experiments were performed in a recirculating water channel with a test area cross section of 45x45 cm and a length of 250 cm. The flow velocity was controlled to a resolution of $0.004\, m/s$, and was measured by particle image velocimetry (PIV). The ambient turbulence intensity of the flow was measured at $< 1\%$ for the range of velocities used.

4.2.3 Quantitative flow imaging

Fluid velocity was measured using high-speed particle image velocimetry. The flow was seeded with tracer particles with a mean diameter of $10\mu m$ that were illuminated by a pulsed Nd:YLF dual diode-pumped laser. The images were processed with Davis LaVision 8.3 software using a multipass cross correlation technique [55]. The field of view of images was $325\, mm$ x$325\, mm$, and the resolution of the image capture was 1024x1024 pixels. The smallest interrogation windows used were 12x12 pixels, yielding a resolution of 0.26 vectors/mm. As a result, the smallest eddy structures that could be resolved from a grid of four vectors was 7.7 mm [82].

4.3 Results

4.3.1 Calibration

The majority of experiments in the current work were performed with the turbine prototype configured with the baseline values used in the previous work of Boudreau et al. [20]. The parameters that are universal to both the previous baseline case by Boudreau and the current study are provided in Table 4.2. They correspond to the structural parameters defining the inertial and elastic terms in the governing equations, which remained unchanged over time, as well as the Reynolds number of the system. Other system values were also held constant, including the depth of the water channel, the use of endplates, and the foil submergence depth. The system was moved 240 mm further downstream in the channel than in the previous work to facilitate additional experimental equipment in the channel, however the change in the boundary layer thickness and turbulence intensity at this location was small, and not accounted for.

An initial set of calibration tests was conducted to quantify any changes in system performance due to increased wear or corrosion since the previous experimental campaign conducted by Boudreau et al. [20], which was performed 24 months prior to the current sets of experiments. The intent of these calibration tests was to assess the changes in motion and performance resulting from potential changes in Coulomb friction and viscous damping in the pitch and heave bearings. Following the calibration, the heave damping could be altered to compensate for the differences in heave bearing friction, to maintain similarity between past and present experiments.

The new damping coefficients for the pitch and heave degrees of freedom were determined from free decay tests performed at the beginning and end of experimentation, to quantify the change in parameters that occurred during testing. The values from the previous work and the current are shown in the bottom of Table 4.2. The values measured before and after experiments are provided in the set of brackets, separated by a comma. The viscous heave damping showed a large percent increase from the values in the previous campaign. On average, between the values recorded before and after experiments, the viscous heave damping approximately doubled. The Coulomb friction in heave was largely unchanged, remaining within the uncertainty range of the previous values. This was also the case for the viscous damping in pitch. Lastly, the Coulomb friction in the pitch axis showed a decrease in magnitude from

the previous experiments. This is attributed to the additional cleaning and lubrication that was added to the system. Of note, there was less variation in values over the course of a day in the current tests than in the previous work, suggesting that wear and corrosion in the bearings stabilized over time.

Table 4.2: Baseline case parameters. Comma-separated values indicated values measured before and after experiments.

Parameter	Constant Value	
Re	21 000	
m_h	3.36 ± 0.05	
I_θ	0.091 ± 0.001	
S^*	0.040 ± 0.001	
k_h^*	1.91 ± 0.03	
k_θ^*	0	
$D_{h,e}^*$	1.23 ± 0.03	
	Current Value	Previous Value [20]
$D_{h,V}^*$	[0.124, 0.115]	$[0.047, 0.074] \pm 0.008$
D_θ^*	[0.004, 0.005]	$[0.003, 0.005] \pm 0.003$
$C_{F_{yCoulomb}}$	[0.058, 0.050]	$[0.07, 0.07] \pm 0.04$
$C_{M_{yCoulomb}}$	[0.008, 0.007]	$[0.015, 0.021] \pm 0.005$

The increase in bearing frictions impacted the performance metrics of the system, as shown in Table 4.3, which provides the performance of the previous baseline case [20], and that of the current test with matching heave eddy-brake damping, and with a corrected heave eddy-brake damping.

Table 4.3: Performance of the baseline case with varied eddy-current dampings.

Metric	Averaged Value		
	Previous [20], $D_{h,e}^* = 1.23$	Current, $D_{h,e}^* = 1.23$	Current, $D_{h,e}^* = 1.17$
f^*	0.133 ± 0.001	0.132	0.133
ϕ	99 ± 3	98.1	96.8
H_0^*	0.891 ± 0.002	0.805	0.881
θ_0^*	$85° \pm 0.9°$	82.9°	84.9°
η_e	$26.8\% \pm 0.7\%$	25.8%	24.9%
$\overline{C_{P_{h,e}}}$	0.68 ± 0.02	0.611	0.631

When the eddy-brake damping was maintained at the value used in previous experiments, the motion amplitudes and oscillation frequency were reduced, and effi-

ciency and power take-off dropped. This result should be expected, where additional energy was lost to the increase in friction. To compensate for this, the damping coefficient was then reduced by adjusting the eddy-current brake, from $D^*_{h,e} = 1.23$ to $D^*_{h,e} = 1.17$. This value corresponded to decreasing the damping in eddy brake by the amount that the heave friction had increased. This adjustment allowed the motion amplitudes to match those in the previous work; at least to within the range of uncertainty of the previous baseline. The efficiency and power coefficient were still lower, directly corresponding to the amount of energy lost to heave friction increases. Regardless, the change in eddy-brake current was seen as important in improving similarity between past and present experiments, and therefore the value of $D^*_{h,e} = 1.17$ was used consistently hereafter. It is worth mentioning that matching the past experiments is not critical for the purposes of the current study, but doing so allows the operation of the current baseline case to be better understood.

4.3.2 Symmetric perturbations

It has been noted by Boudreau et al. [20] and in the current experiments that short, isolated disturbances, such as a single large convecting vortex upstream of the turbine, or physical disturbances applied to the structure itself, provide little effect on long term dynamics of the fully-passive prototype. The instantaneous response of the system is dependent on the specific disturbance, however after the disturbance has convected passed the wing the fully-passive system returns to steady, full-amplitude periodic motion returns within 1 to 3 oscillation periods. In this sense, the system is impressively stable to unsustained disturbances, where momentary losses in performance may occur but the system returns to a stable state rapidly. This scenario was not investigated further.

The response of the system is different for sustained perturbations, of the type that would occur if the fully-passive system was operating in the wake of a bluff body or another upstream turbine. The duration of the disturbances in the inflow conditions leads to a new stable or semi-stable operation state of the fully-passive design. To study this, the fully-passive turbine was subjected to symmetric, periodic large-scale perturbations. This was approached by placing an oscillating-foil turbine with a prescribed motion profile several chord lengths upstream of the fully-passive turbine ($L_x = 6.5c$), as illustrated in the schematic of Fig. 4.3. This arrangement is referred to as tandem alignment [64]. The upstream foil produced a time-averaged

wake with a momentum deficit, as well as an unsteady von Karman vortex street that supplies the dominant perturbations in the wake.

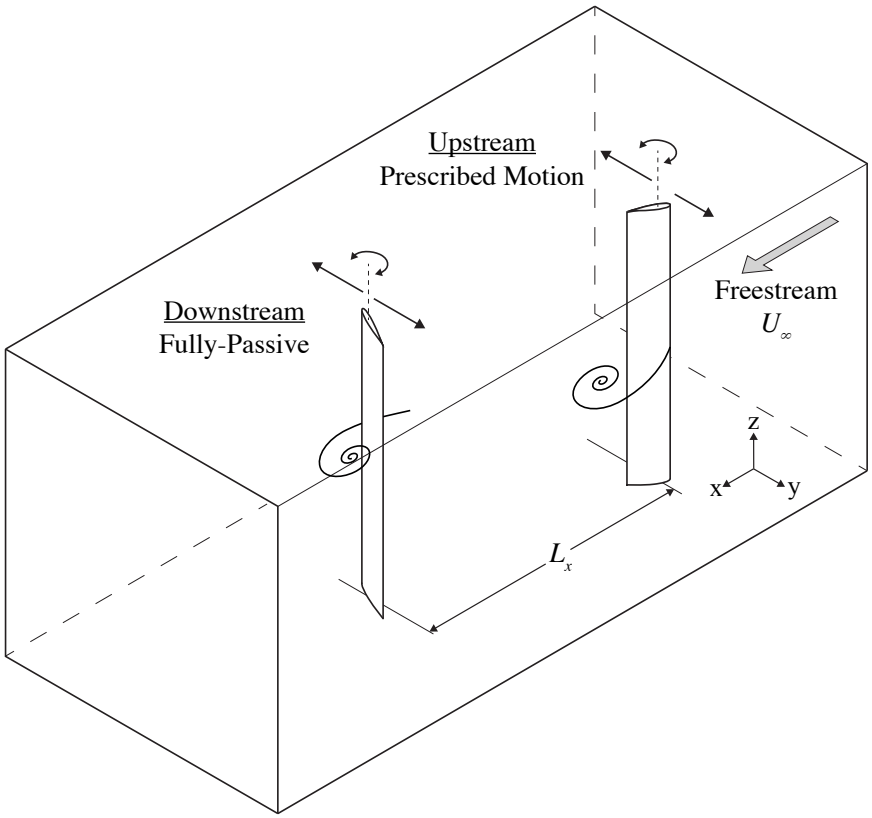

Figure 4.3: Schematic of the tandem turbine apparatus. The upstream foil has prescribed kinematics, while the downstream foil is the fully-passive prototype. The wake structures shown are for illustrative purposes only.

This is a system that may never be fully realized in the practical operation. The scale, blockage effects, and boundary conditions prevent this exact study from being used as a general model. However, the intent of this section of the study is not to prescribe a specific scenario and present it as a general representation of a tandem turbine configuration(the possible parametric space is simply too large for this to occur) but rather to discover some underlying trends in the system's operation.

Tandem NACA 0015 foils of similar arrangement were parametrically studied by numerical 2D methods in the work of Kinsey and Dumas [64]. In some of their tested cases, a similar separation distance of $L_x = 6.4c$ was used, as well as several separations. The study was based on two foils with prescribed motions, and focused on optimizing the combined performance of the tandem system. They showed impressive

net system efficiencies; up to 64%. This value meets the Betz limit for tandem turbines [121] [122], which states the maximum energy extraction theoretically capable. The fact that the simple system reaches the highest theoretical efficiencies renews the controversy associated with applying the Betz derivation for unsteady oscillating-foils. Regardless, the high efficiencies are promising in terms of tandem application, where vortex dynamics can entrain freestream momentum into the wake and exceed the performance of steady systems [123].

The work of Kinsey and Dumas [64] found that the position of the dominant vortex in the upstream wake as it convected into the oscillation plane of the downstream turbine was a key parameter. If the vortex was located in a manner that increased the dynamic pressure locally available to the leading edge of the downstream foil, this benefited performance. In contrast, a vortex that decreased local dynamic pressure yielded lower power extraction. This simple classification was adequate in generalizing the trends seen in the parametric tests.

Importantly, in the constrained motion system that was studied, these vortex interactions could be controlled by tuning the oscillation-phases between turbines, and the separation distance between turbines. These values were grouped together into a parameter referred to as the global phase shift [64]. As far as fully-passive designs are concerned, the global phase shift develops freely and the system designer does not have a means to link the upstream and downstream motions except hydrodynamically. The question, therefore, is if the downstream turbine will naturally tune to a beneficial phase shift and follow the trajectory of high dynamic pressure, or follow regions of low pressure and have poor performance.

Methodology

The foil parameters of the constrained turbine, which hereafter may also be referred to as the upstream turbine because of its location, are listed in Table 4.4. The parameters referring to the upstream foil are denoted with a prime, whereas the parameters of the downstream fully-passive foil bear no superscript. The upstream foil dimensions were nearly identical to that of the fully-passive wing, with the exception of the chord length being 1.4% shorter, and the endplates being somewhat larger than those on the fully-passive wing.

The stated performance metrics of the fully-passive turbine for all tests are presented non-dimensionalized by the freestream velocity, U_∞, measured sufficiently up-

Table 4.4: Parameters associated with the upstream foil turbine.

Parameter	Symbol	Value
Foil shape		NACA 0015
Chord length	$c^{'}$	$50\,mm$
Span	$b^{'}$	$380\,mm$
Pitching axis location	$x_p^{'}$	$1/3\,c^{'}$
Material		Aluminum
Motion profiles		Sinusoidal
Phase offset	$\phi^{'}$	90°

stream of both foils. It would also be possible, although not entirely sensible, to define the characteristic velocity of the downstream foil as the average streamwise velocity component at the location of the fully-passive turbine, in the wake of the upstream foil. This approach could be argued to provide a more physical result, however the average streamwise velocity changes for each of the many tested cases. It was therefore chosen to use the upstream velocity to provide a consistent reference.

The upstream velocity varied by small amounts between each case, since the flume tank motor was held at a constant load, but the resistance provided by the turbines varied from case to case. Although the changes were small, the efficiency and power coefficient were proportional to the cube of this characteristic velocity, and small errors in velocity would lead to larger changes in the power extraction metrics. This was accounted for by recording the freestream velocity for every tested case, as measured by PIV techniques several chord lengths upstream of both foils.

The pitch and heave motions of the upstream turbine were controlled by two independent servo motors. The control system, uncertainties, and apparatus are described in more detail in Section 3.2 of this thesis. To maintain some generality, the upstream foil was prescribed sinusoidal pitch and heave motions throughout all tests, and the phase offset between motions was set to 90°.

The upstream foil was positioned a distance of $L_x = 6.5c$ upstream of the fully-passive turbine, as measured from pitching axis to pitching axis. Further, it was positioned at the same height in the water channel, and was also symmetrically mounted in the centre of the water channel. The separation distance corresponded to the smallest distance that was possible under the given experimental constraints. Interference between mounting equipment for each individual turbine prevented closer positioning.

Results

Several parametric spaces, abbreviated hereafter as 'PSpace', were tested, each of which had the upstream's motion varied. For all cases, the downstream fully-passive's structural parameters were held constant at baseline values, with the exception of changes in pitch stiffness. Table 4.5 lists the parameters associated with each case. There, the value of $k_\theta^* = \infty$ corresponds to the pitch axis being locked, creating a single degree of freedom heave system.

Table 4.5: Parameters unique to each test case in the tandem study.

	Upstream variables		Downstream variable
Name	$H^{*'}$	θ_0'	k_θ^*
PSpace 1	0.90	75°	0
PSpace 2	0.90	85°	0
PSpace 3	1.50	85°	0
PSpace 4	0.90	85°	0.051
PSpace 5	0.90	85°	∞

An example of the type of flow structures developed in the wake of the upstream turbine (thus, imposed on the downstream turbine) is shown in Fig. 4.4. The images are drawn from PSpace2, operating at $f^* = 0.122$. The PIV images were recorded at the midchord plane in the wake of the upstream foil, while the downstream turbine was absent from the channel. The field of view is $6.5c$ by $6.5c$, and flow is from the right. Out-of-plane vorticity contours are shown; red representing clockwise rotation. The vector arrows shown have been downsampled by a factor of 4 for visual clarity. Further, a simple Galilean transformation has been applied to the streamwise component of the velocity, such that the entire flow field has had the convective velocity of the primary leading edge vortex subtracted from the streamwise component of velocity[124]. This was done simply to aid in visualization of the developing vortices.

The location of the upstream foil is shown directly, while the heave plane of the pitching axis of the fully-passive turbine is shown by the large arrow located downstream. The extent of the heave motion is shown approximately, as it varies on a case-by-case basis. Periodic vortices developed in the wake, on the scale of the foil's chord length, either as a result of dynamic stall and the associated leading edge vortex, or a result of shear layer roll-up, depending on the dynamics of the upstream turbine. It is noted that the frequency of the upstream turbine's motion directly corresponds

to the frequency of the perturbation imposed on the downstream turbine; i.e., can be directly interpreted as the frequency of imposed vortices.

According to previous works by Fenercioulu [83] and Kinsey and Dumas [84], which studied the 3-dimensional structures of the near wake of oscillating-foils, the initial dynamic stall vortex is coherent along the span of the foil, decaying somewhat near the tips due to finite aspect ratio effects. Therefore, the images of Fig. 4.4 show a reasonable 3-dimensional representation in the direct vicinity of the foil. However, wake contraction occurs as a result of the chordwise vorticity concentrated near the foil tips, causing the spanwise vortex to breakdown as it convects into the wake [125]. This is evident in the PIV images, where the primary vortex had largely broken down once it convected as far as the downstream turbine.

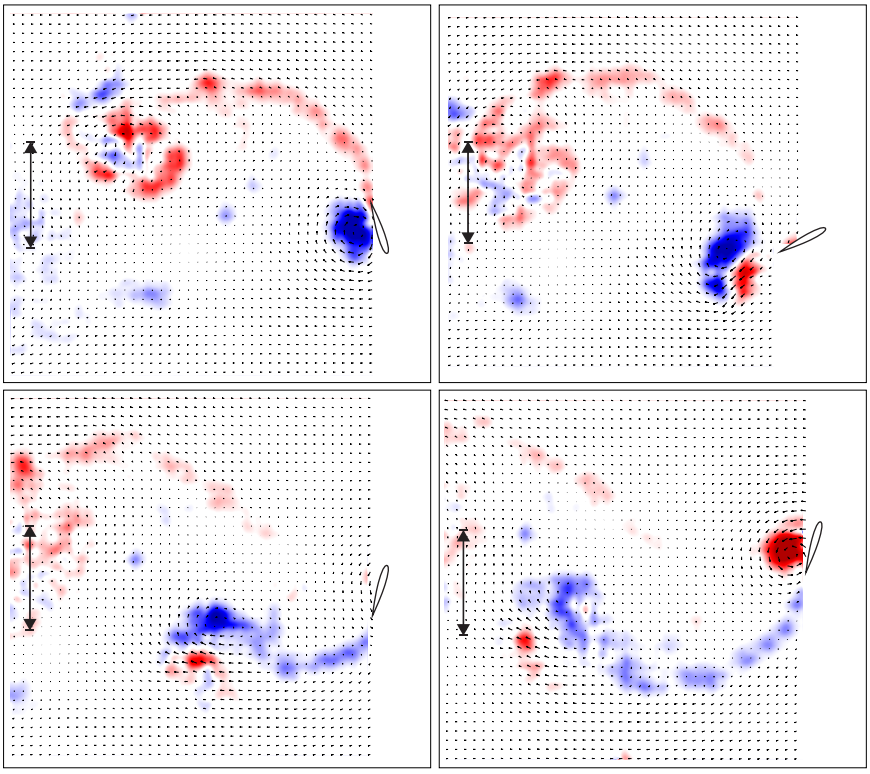

Figure 4.4: Planar PIV images recorded at midchord in the wake of the upstream turbine. Colours indicate out-of-plane vorticity levels (red showing clockwise rotation). Flow is from the right.

The performance of the fully-passive turbine operating in the wake of the upstream turbine at conditions PSpace1 and PSpace2 is shown in Figs. 4.5 and 4.6 respectively. Here, the heave amplitude of the upstream foil was set at $H^* = 0.90$, similar to that

of the fully-passive baseline case in a uniform freestream. The pitch amplitude for the two conditions was set at 75°, and 85°. This variation provided slightly different vortex dynamics in the upstream turbine's wake, as well as different amounts of momentum extraction by the upstream turbine. For both parametric spaces, the reduced frequency was varied in small increments in a range at and below the frequency that the fully-passive turbine operated at in baseline, uniform freestream conditions. Outside this range of frequencies, the fully-passive foil was observed to have poor performance with unstable and non-periodic motions.

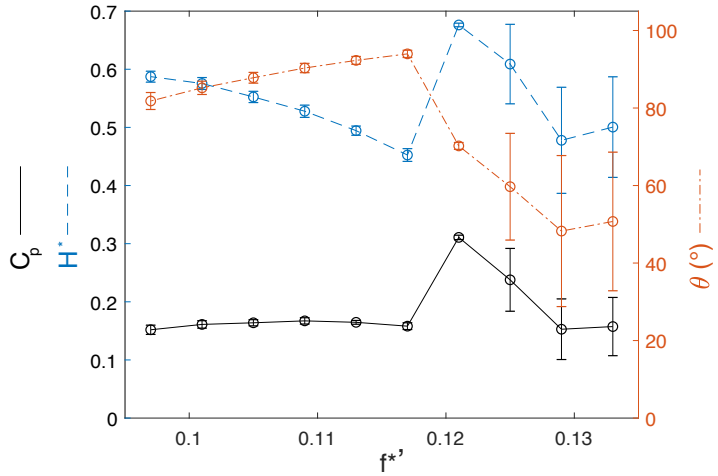

Figure 4.5: Averaged power coefficient, heave amplitude, and pitch amplitude of the fully-passive turbine for PSpace1. $f^{*'}$ is the frequency of the upstream turbine.

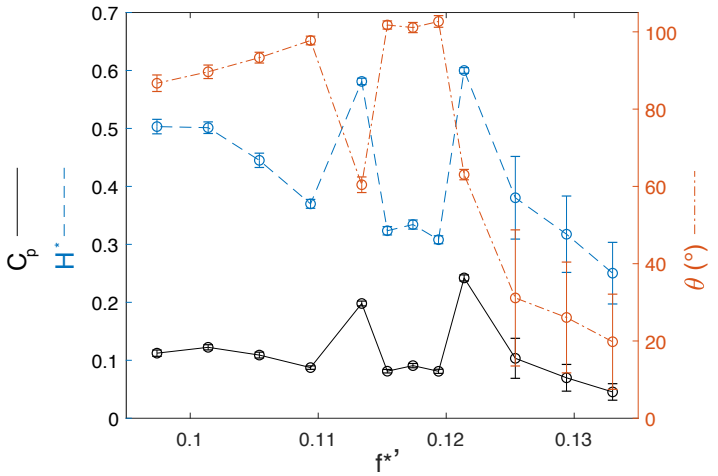

Figure 4.6: Averaged power coefficient, heave amplitude, and pitch amplitude of the fully-passive turbine for PSpace2. $f^{*'}$ is the frequency of the upstream turbine.

The performance of the fully-passive foil is assessed here by the power coefficient, C_p, which unlike efficiency is independent of the heave amplitude, and allows for a clear comparison of power extraction. Figs. 4.5 and 4.6 also show the heave amplitude (H^*) and pitch amplitude (θ_0), providing insight into the motion dynamics. Results were averaged over 90 cycles, and the standard deviation associated with the averaging is shown as error bars centred on the data points in the figures.

In each space tested, the power extraction was significantly lower than that of the baseline case, which had a value of $C_p = 0.62$. This result is not unexpected, considering the momentum deficit in which the turbine operated. Further, there existed only a small region of frequencies where stable oscillations occurred on the fully-passive turbine, which is the range shown in the present results.

Assessing first PSpace1, in Fig. 4.5, it was apparent that the fully-passive turbine operated in several modes depending on the dynamics and time scale of the upstream perturbation. At high frequencies, there was large variations in cycle-to-cycle performance, as indicated by the large standard deviation for each value. It is recalled here that in an undisturbed freestream, the fully-passive turbine with baseline parameters oscillated at $f^{*'} = 0.133$, a frequency which presently shows poor performance.

As the frequency decreased to at and below $f^{*'} = 0.122$ the downstream turbine's oscillations stabilized and became periodic, operating at the frequency of the imposed time scale. There was a notable increase in power output near the threshold at which stable oscillations occurred. Stable oscillations continued as the frequency was decreased further, and power output stabilized at a low value.

The performance metrics of the second parametric space, in which the pitch amplitude of the upstream foil was changed to 85°, are shown in Fig. 4.6. Once more, unstable oscillations were observed above a critical frequency, occurring just above the frequency leading to the highest power extraction. However, in this condition a second high performance case existed at a lower reduced frequency, where heave motion was large.

These observations suggest that the dynamics of the fully-passive turbine can be divided into two regions, those that developed stable periodic oscillations, and those with more erratic motions. For PSpace1 and PSpace2, stable motions resulted in the range $f^{*'} <= 0.125$. At higher frequencies, the motions would briefly resonate with the time scale of the imposed perturbation, before lagging out of alignment. With time, this resonance would briefly occur again. This resulted in a large standard deviation between the collected cycles. This is illustrated in Fig. 4.7, which provides

heave and pitch motion profiles over 12 cycles for various cases. Specifically, the cases with frequencies immediately below the stability boundary, and cases with the frequency immediately above the boundary, are shown.

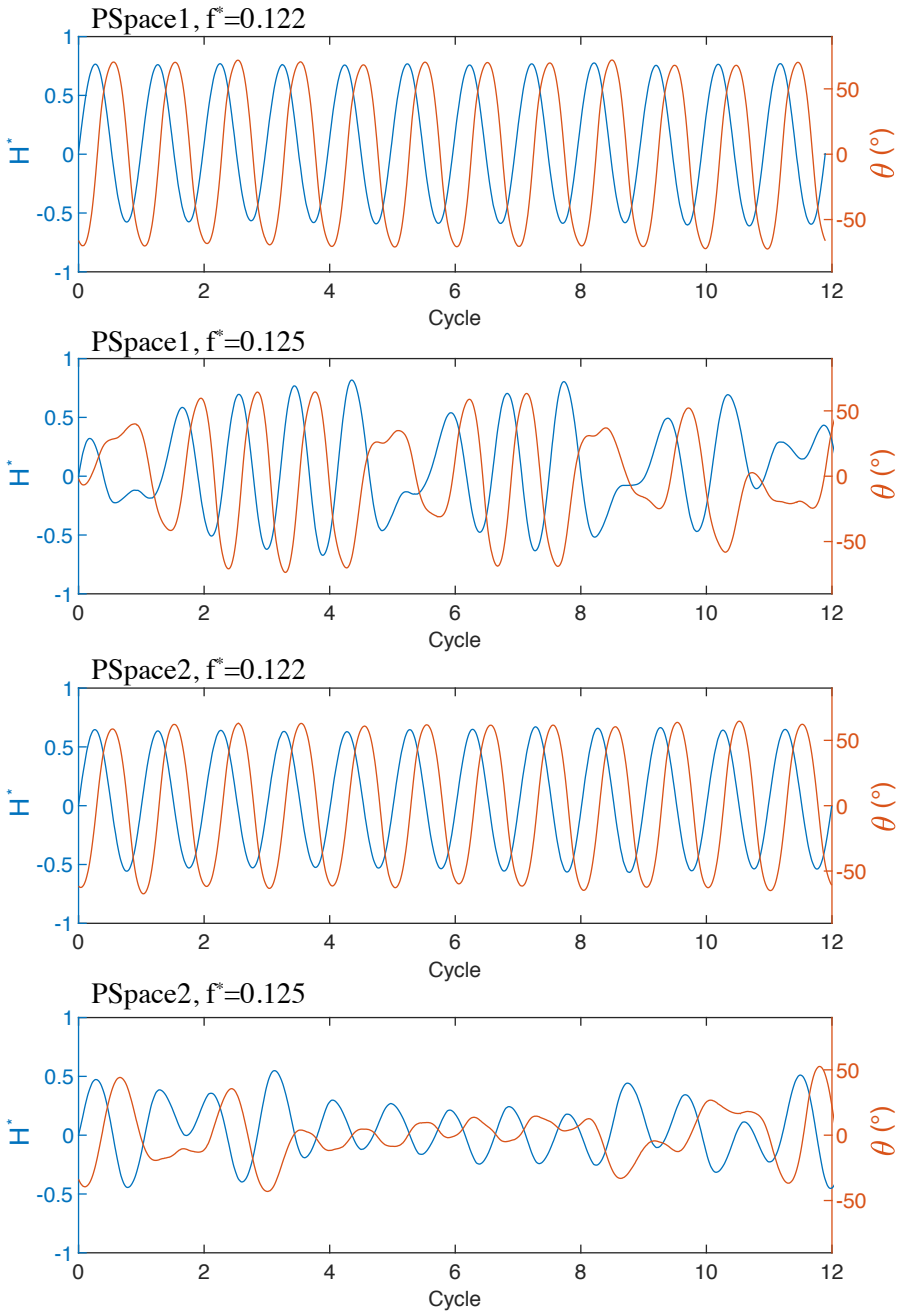

Figure 4.7: Heave and pitch motions over 12 oscillation cycles for selected conditions.

The results of the third suite of tests, PSpace 3, is shown in Fig. 4.8. In this

condition, the heave amplitude of the upstream turbine was increased to $H^* = 1.50$, which increased the width of the wake proportionally. Despite this, the trends were similar to the previous conditions, showing a boundary between regions of erratic motions and stable motions, and a narrow region of peak power extraction. The magnitude of the power coefficient and heave amplitude occurring at the highest extraction point was on the same order as the previous cases.

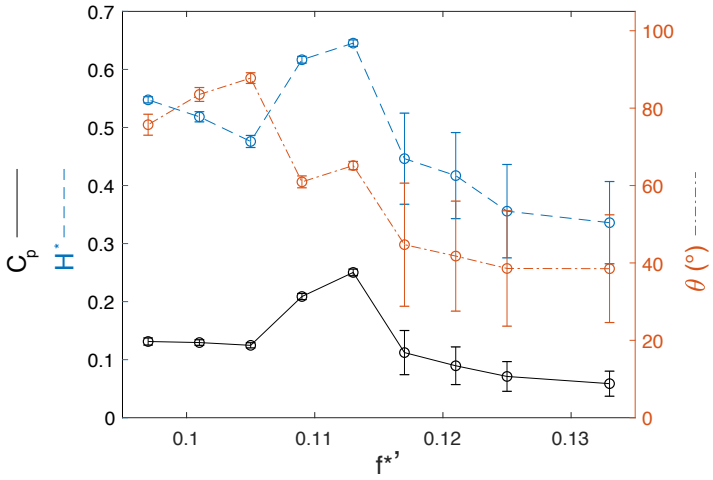

Figure 4.8: Averaged power coefficient, heave amplitude, and pitch amplitude of the fully-turbine for PSpace3.

PSpace4 represents a condition where light pitch springs were added, increasing the stiffness value to $k_\theta^* = 0.051$. The performance of this case is assessed in Fig. 4.9. For all tested frequencies, the resulting pitch amplitude was small, leading to essentially heave-only motion, with low power extraction. The oscillations were stable, though, occurring at the same time scale as the imposed vortices. It was observed later on that the momentum deficit in the wake of the upstream foil caused the flow velocity to be below the critical divergence velocity for the system with this pitch stiffness [115]. That is, from a theoretical perspective the divergence phenomena that drives the motion would not be expected to occur at this reduced velocity.

PSpace5, where the turbine was reduced to heave-only motion, oscillated very similarly to PSpace4, as shown in Fig. 4.10. This indicates that the motion occurred as a result of the low pressure regions associated with the vortices, rather than stall flutter.

It was proposed that the frequency of the perturbation that yielded the highest power extraction in each parametric space was associated with the natural operation

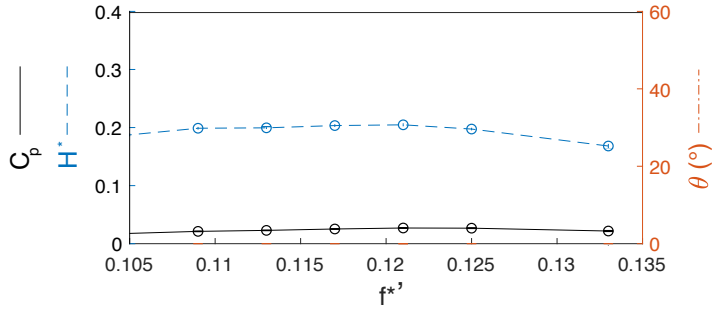

Figure 4.9: Averaged power coefficient, heave amplitude, and pitch amplitude of the fully-turbine for PSpace4.

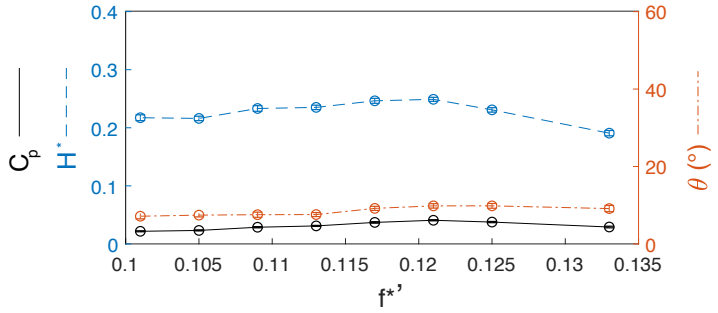

Figure 4.10: Averaged power coefficient, heave amplitude, and pitch amplitude of the fully-turbine for PSpace5.

frequency that the turbine would operate at in a uniform, time-averaged wake. To test this, the time-averaged flow profile behind the upstream turbine was measured with PIV. During these measurements the downstream turbine was removed. Time-averaged images were averaged over 2000 instantaneous recordings, recorded at 50 Hz, such that no aliasing between data acquisition and vortex shedding occurred. An estimate for the average velocity flux through the swept area of the downstream turbine was found by taking 13 planar xy PIV images evenly spaced along the span of the downstream turbine, as shown in the schematic of Fig. 4.11. In each plane, the velocity along the swept length of the downstream turbine's pitch axis was recorded and spatially averaged. The average velocity in the entire swept window of the foil was then estimated by averaging the values at each plane. This averaging approach was applied to four cases, which are listed in Table 4.6. There, the value $V_{reduced}$ represents the temporally and spatially averaged streamwise velocity component normalized by the freestream velocity, as measured by the previously outlined technique.

The time-averaged PIV images recorded on one half of the spanwise heights, for

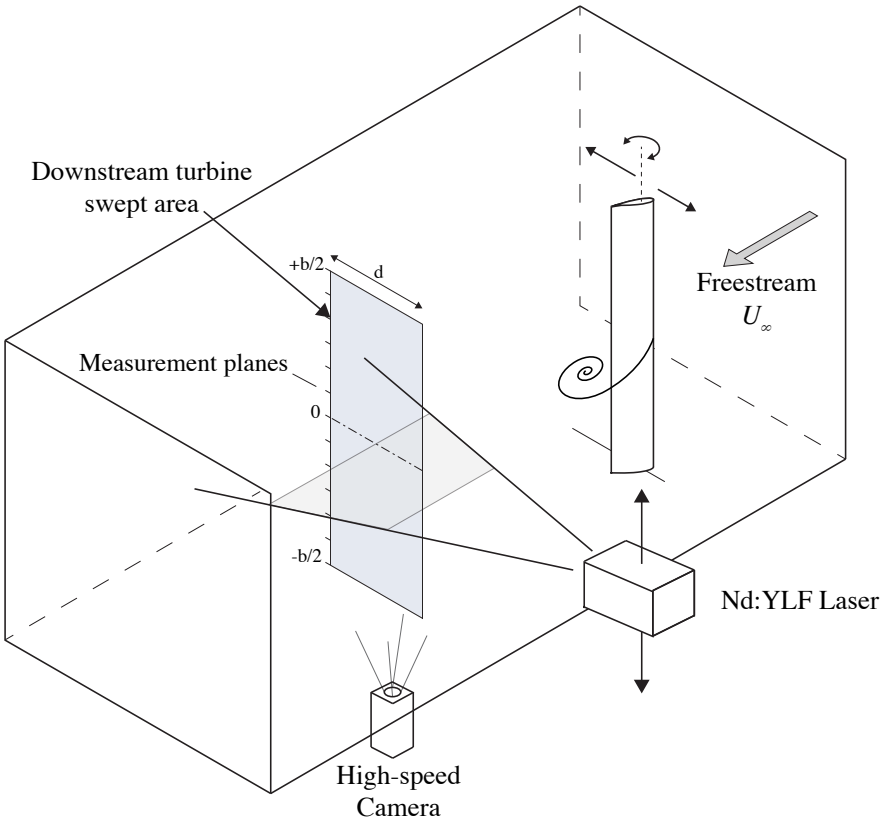

Figure 4.11: Simplified schematic the planar PIV approach.

condition PSpace1 at $f^{*'} = 0.122$ are provided in Fig. 4.12. In those images, the colour scheme shows the streamwise velocity component of flow, where white corresponds to a value equivalent to the freestream flow, U_∞. Regions of red correspond to areas with reduced streamwise velocity, and therefore a velocity deficit. The grey bar shows the approximate location of where the downstream turbine would be located, had it not been removed for the current measurements.

It was clear that the downstream turbine operated in a region with strongly reduced momentum. The momentum reduction was largest near the midspan location, as shown in images at heights $0/12b$, $1/12b$, and $2/12b$. Flow velocity near the ends of the foil was closer to the freestream velocity, a result of wake contraction along the spanwise direction due to finite aspect ratio effects [125].

The performance of the fully-passive turbine operated in the uniform, reduced velocity freestream is compared against the operation in the wake that caused the equivalent momentum deficit. This comparison is made in Table 4.6. To clarify, in a time-averaged sense, the turbine operated in the same energy flux in both conditions,

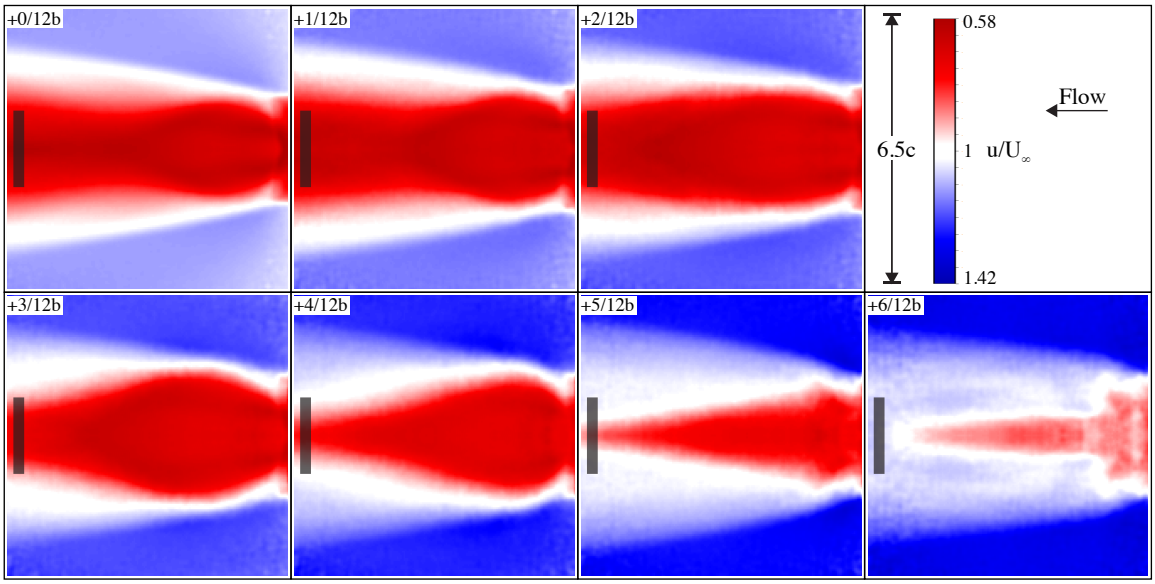

Figure 4.12: Time-averaged PIV images of normalized streamwise velocity in the wake of the upstream turbine. The grey bars represent approximate location of the downstream turbine. Measurement planes correspond to the schematic of Fig. 4.11.

but the instantaneous flow fields were different.

The conditions shown were selected because they represented the reduced frequency at each case that yielded the highest power extraction. It was theorized that this frequency was that at which the fully-passive turbine would naturally oscillate at in the reduced flow condition. This was found not to be the case, with the reduced freestream case showing distinctly lower reduced frequencies.

In contrast with the uniform freestream case, the turbine operating in the wake showed large increases in performance for most of the cases. In the case of PSpace 3, this corresponded to an increase in power extraction of 3.84 times from the uniform inflow case.

Discussion

It was apparent that a natural time scale exists for the dynamic stall event driving the stall flutter on the fully-passive turbine. When this time scale was sufficiently different from the time scale of the imposed perturbations, the periodic motion of the turbine degraded significantly. This likely puts a halt to the hypothesis that imposing a time scale onto the fully-passive turbine could be used to increase its oscillation frequency, in an attempt to reach kinematics that yield higher energy-extraction efficiencies.

Table 4.6: A comparison of fully-passive turbine performance between two cases of equivalent time-averaged velocity.

	Operation in uniform flow			Operation in wake		
Condition	$V_{reduced}$	f^*	$\overline{C_{Puni}}$	$f^{*'}$	$\overline{C_{Pwake}}$	$\Delta C_P = \overline{C_{Pwake}}/\overline{C_{Puni}}$
PSpace1	0.78	0.088	0.107	0.122	0.310	2.90
PSpace2	0.87	0.114	0.263	0.122	0.242	0.92
	0.75	0.081	0.065	0.117	0.090	1.39
PSpace3	0.76	0.081	0.065	0.113	0.250	3.84

These results limit the practicality of using multiple fully-passive turbines in tandem arrangements. First, the range of kinematics of the upstream turbine that produce beneficial wakes for the downstream turbine was very narrow. It is unlikely that a tandem system of this nature would sustain itself in real-world environments where the freestream velocity, and therefore the reduced frequencies of the system, vary with time. Further, the natural frequency of an upstream fully-passive turbine does not correspond to a useful frequency of vortices in the wake for subsequent downstream turbines.

Observation of the wake showed a significant time-averaged momentum deficit in the wake of the upstream turbine. The tandem arrangement used in the current tests had the fully-passive turbine placed directly centred in this momentum deficit, which by definition limits the power extraction capabilities of the turbine. The extraction of energy from the upstream turbine caused a streamtube expansion, where a portion of the freestream flow was accelerated around the wake of the turbine. It would be valuable to test the operation of the fully-passive turbines in a configuration that placed them in these regions of high-momentum. This would occur in a staggered arrangement, where the equilibrium position of the foil is translated in the y-direction (heave direction) to locate it outside the wake. Translation in the spanwise z-direction would also place the turbine into higher velocity regions, as there is significant spanwise contraction of the wake due to finite aspect ratio effects. It would also be interesting to vary the separation distance between the two foils. If the downstream turbine was moved closer to the upstream turbine, this would place it in a region with even lower momentum. However, the vortices from the upstream turbine will be more coherent, and may have more influence on the downstream foil.

A further point worthy of mention relates to the addition of pitch springs to the

system. Recalling that the current turbine relies on a divergence phenomena, there exists a critical velocity at which divergence will occur. Increasing the pitch stiffness proportionally increases the critical velocity. This was observed in the current study, where the addition of light pitch springs prevented large scale motion when operating in the wake. From this perspective, systems with low pitch stiffnesses are seen as beneficial when operating in wakes.

Lastly, it was observed that although the fully-passive turbine had poor performance in the wake of the upstream turbine, the unsteady perturbations in the wake significantly enhanced the motion and performance of the foil compared to equivalent uniform flow conditions. This suggests that viewing the wake in a time-averaged sense is not appropriate, and it is also interesting to see the enhancement in performance from tuning with the perturbations. The power coefficients presented throughout this section used the upstream freestream velocity as the characteristic velocity for consistency. However, if the time-averaged reduced velocity measured in the wake of the upstream foil were used instead, the performance is more impressive. For example, the condition PSpace1 at $f^{*'} = 0.122$ would have a redefined $\overline{C_P}$ of 0.65, which is impressive.

4.3.3 Influence of boundary layer tripping

Previous work, performed in Section 3 of this thesis, has highlighted some of the difficulties associated with experimental campaigns performed in transitional Reynolds numbers; particularly with dynamic stall events. One such difficulty is the transition event occurring within the boundary layers on the foil. In the case of constrained motion profiles, it was observed that applying a thin strip of distributed roughness elements along the foil provide some influence on the performance of the foil; particularly during the periods of motion where the angles of attack were low, and flow separation or reattachment was occurring. These changes in boundary layer dynamics had small influences on systems with constrained motion, but may have larger influences on fully-passive systems where there is a strong two-way coupled fluid-structure interaction (where changes in forces will feed back into the motion of the structure). This is tested within this section by similar means, outlined in the below subsection.

The previous study also highlighted channel confinement as a factor than can influence performance. However, blockage corrections cannot readily be applied or validated for the current fully-passive prototype for two reasons. First, drag, a re-

quired value for the estimation of blockage corrections, is not measured. Second, the proximity of the channel wall changes the effective angle of attack imposed on the foil, which in turns changes the forces on the foil. These effects compound in the two-way fluid-structure interaction, and therefore the changes predicted by the simple blockage correction models are unlikely to account for the coupled dynamics in the turbine system.

Methodology

The influence of boundary layer tripping was tested by applying a strip of distributed roughness elements, $0.08\,c$ wide, along the full length of the blade span at the position of maximum thickness. Roughness was applied on both sides. The roughness physically was a strip of adhesive 40-grit sandpaper, cut to width. Non-dimensionally, this generated a roughness Reynolds number ($Re = u_k k/\nu$) of approximately 600. In this definition of roughness Reynolds number, the characteristic length is the roughness element height above the surface, k, and the characteristic velocity is the velocity of the boundary layer at the roughness height, u_k. These values were determined with the guidelines outline by Braslow and Knox [81]. This value was observed sufficient in previous tests tripping the boundary layer at the current chord-based Reynolds number of 21,000.

As before, the cycle-averaged results presented in this section have been averaged over 90 oscillation cycles. The instantaneous data presented has also been averaged over 90 cycles to filter out fluctuations in cycle-to-cycle motion.

Results

The baseline case, and the baseline case with added pitch stiffness ($k_\theta^* = 0.051$) were tested with and without boundary layer tripping, for a total of four distinct conditions. The metrics associated with each condition are provided in Table 4.7. There, columns headed by the abbreviation 'Std.' correspond to the standard deviation computed over the 90 cycles. For the baseline case, the presence of a surface trip had low influence on system performance. The peak pitch amplitude increased minorly, by 3°, and the phase lag between pitch and heave motions increased by 2°. However, the heave amplitude, and the power output (which is extracted only from the heave motion), were not changed by the presence of a trip. When pitch springs were added to the system, the influence of the trip was still low. Interestingly, the pitch ampli-

tudes decreased by about 3°, but the oscillation frequency increased by 5%. Further, the power extraction efficiency increase by 3%. The standard deviations were not significantly altered by the presence of roughness, indicating that the roughness did not improve or degrade cycle-to-cycle consistency.

Table 4.7: A comparison of turbine performance with untripped and tripped boundary layers.

Performance Metric	Baseline Case				Baseline with $k_\theta^* = 0.051$			
	Untripped		Tripped		Untripped		Tripped	
	Value	Std.	Value	Std.	Value	Std.	Value	Std.
f^*	0.135	0.002	0.135	0.002	0.130	0.003	0.137	0.002
ϕ	94.8°	2.2°	97.9°	2.4°	98.9°	2.6°	95.3°	2.2°
H_0^*	0.857	0.011	0.854	0.011	0.950	0.012	0.945	0.012
θ_0^*	84.7°	0.3°	86.4°	0.2°	73.3°	0.4°	75.3°	0.3°
η_e	0.244	0.005	0.243	0.005	0.262	0.005	0.27	0.006
$\overline{C_{P_{h,e}}}$	0.614	0.015	0.612	0.018	0.690	0.021	0.738	0.023

An instantaneous perspective for both sets of conditions is provided in Fig. 4.13. The figure plots the heave position and pitch position of the turbine over the course of an averaged cycle. In both sets of cases, the heave amplitude was not reasonably affected by the trip at any point in the cycle. The pitch position showed a slight change in both cases as a result of the boundary layer tripping. However, the trend was different between the baseline case and the baseline-with-springs case. In any regard, the difference is small enough that it could be the result of inaccuracies in the data acquisition.

Discussion

As before, the system was largely dependent on robust stall dynamics, of which the roughness had little influence. A more detailed discussion on the matter was presented previously in Section 3. It is difficult to conclude how the roughness influenced the fully-passive system without further, fundamental analysis. It is suggested that because the flow on the boundary layer was separated for a large portion of the oscillation cycle, tripping the boundary layer artificially had little consequence. It is also difficult to draw direct similarities from previous work on boundary layer tripping, where different oscillation dynamics were present, and energy was also extracted from the pitch motion. This previous work suggested that the application of surface roughness

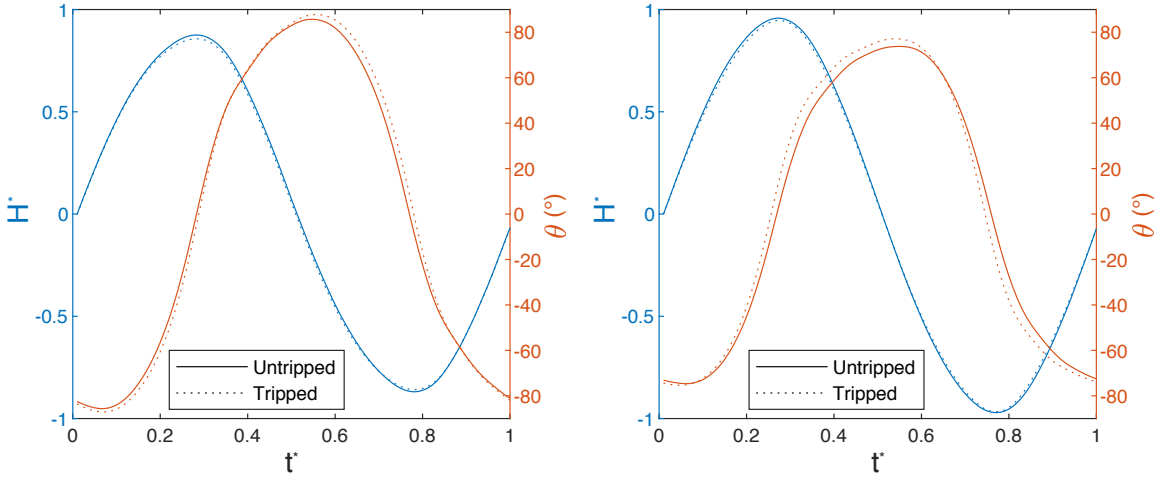

Figure 4.13: Motion profiles of tripped and untripped foils. Left: baseline case. Right: baseline case with $k_\theta^* = 0.051$.

helped improve similarity with higher Reynolds number ($\mathcal{O}$ $(500,000)$). However, this change was only on the order of a few percent in relative efficiency. Provided the small influence in the current results, it is recommended that roughness not be implemented in future experiments in this fully-passive campaign. Some differences in performance with a tripped foil may become more pronounced at other kinematics, but the application of roughness introduces uncertainties, and lessens repeatability between experiments.

4.3.4 Freestream turbulence

Perhaps one of the most relevant condition that exists in many river and tidal sites that is not commonly reproduced in lab environments is high levels of freestream turbulence. Many flow facilities, including the flume tank at the University of Victoria, are designed to minimize turbulent fluctuations and provide near-uniform inflow conditions, typically with turbulent intensities (I) below 1%. In fact, this uniformity of the flow may be viewed as a limitation in experimental capabilities in some instances, should the desire be to replicate real-world operating conditions. In deep and wide rivers, or other flows with low velocity, turbulence intensities may range between $1\% - 5\%$. In faster currents, intensity levels of $5\% - 20\%$ may occur [126] [127] [128].

Freestream turbulence has several implications on the flow dynamics of fully-passive turbines. Turbulence in the freestream produces unsteady fluctuations which

changes the receptivity of the boundary layer [129]. That is, promoting a transition within the boundary layer by bypassing primary modes and creating instabilities causing the boundary layer to quickly become turbulent. The effect of this may be emphasized at transitional Reynolds numbers.

Vortical structures present in the freestream can provide intermittencies in dynamics pressure available to the foil, or otherwise impact the foil by changing instantaneous effective angles of attack. Provided that the turbulent eddies are large enough to break up the coherence of the leading edge stall vortex, it could significantly and chaotically alter the stall dynamics, leading to erratic motion. In this regard, it would be anticipated that turbines with longer span lengths would be less susceptible to such an event, as on average the foil would be subject to a more uniform inflow.

The current subset of experiments subjects the fully-passive turbine to several turbulence intensities, which were generated by a set of rigid fractal grids designed and characterized by Mahfouth [126]. The specifics of the grids are provided in detail in the following subsection. As before, the baseline case is studied in detail, as well as the baseline case with a spring stiffness of $k_\theta^* = 0.051$. A third case was tested, which comprised of the turbine configured to baseline values, but with the freestream velocity increased, changing the Reynolds number from 21,000 to 25,000.

Methodology

The turbulence intensity was increased from ambient channel levels by installing fractal grids at specified lengths upstream of the turbine, in the yz plane. The fractal grids consisted of repeating square patterns at decreasing scales, as shown in Fig. 4.14. The reader is referred to the thesis of Mahfouth [126] for a full discussion on the benefits of fractal grids, opposed to other common turbulence generators. The two grids used are referred to hereafter as Grid N3 and Grid N4, corresponding to the number of fractal iterations on each grid.

Four turbulent conditions were generated by application of different grids, and by varying the location of the grids. The four conditions are stated in the list below, ordered by increasing turbulence intensity. In all cases, the turbine was moved downstream in the water channel an additional $1.5\,m$ from its position in the experiments presented in the previous sections. This resulted in a higher ambient turbulence intensity than the previous tests, so the performance at these new ambient conditions was retested at this location.

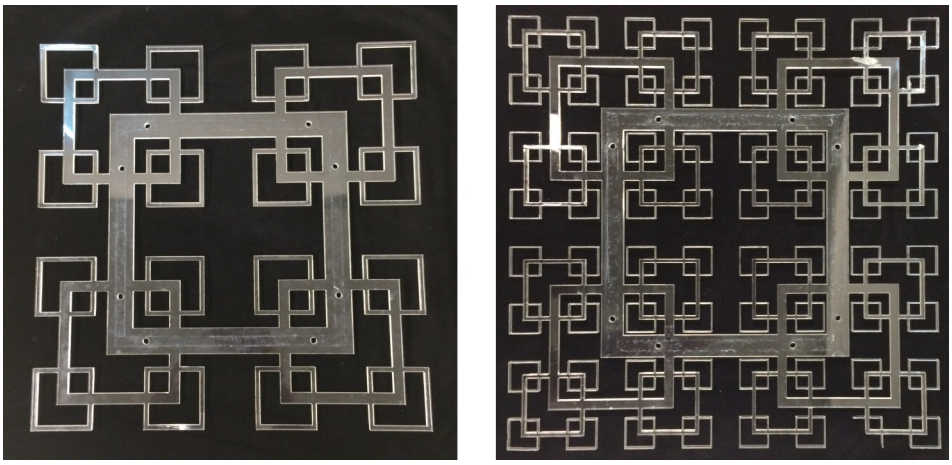

Figure 4.14: Images of the fractal grid turbulence generators. Left: Grid 'N3'. Right: Grid 'N4'.

Turbulence conditions:

- Ambient flow, with no grid
- Grid N4, positioned $1\,m$ upstream of the turbine
- Grid N3, positioned $1.5\,m$ upstream of the turbine
- Grid N3, positioned $0.5\,m$ upstream of the turbine

The turbulence intensity was calculated by dividing the standard deviation (σ_i) of the velocity components by the characteristic velocity, as $I_i = \sigma_i / U_\infty$, where:

$$\sigma_i = \frac{\sqrt{\sum_1^N (u_i - < U_\infty >)^2}}{N-1} \tag{4.16}$$

The velocity components of the flow field were recorded in the xy plane, with a field of view $6c$ x $6c$ centred at the equilibrium position of the fully-passive foil. This allowed the streamwise turbulence intensity component (I_x) and the in-plane normal component (I_y) to be extracted. The out-of-plane component (I_z) was not directly measured, but assumed sufficiently similar to the I_y component that was measured.

The turbulence intensities from 300 PIV images, recorded over a time scale of roughly 20 oscillation cycles at the baseline operating frequency, were averaged to yield representative values.

Results

Typical images of the flow field for each condition at Re = 21,000 are provided in Fig. 4.15. The streamwise component of velocity, u_x, is shown by the colour scale, while the vector arrows show the net in-plane velocity component. The streamwise velocity component has been non-dimensionalized by the freestream velocity following a Galilean transformation, as $u_x^{'} = (u_x - U_\infty)/U_\infty$ [90]. This was performed to aid in the visualization of turbulence. The colour scale is consistent for all images, making the variations in turbulence intensity between conditions evident. The magnitude of the two in-plane components of turbulence intensity, I_x and I_y, are provided in the figures. It is noted that the turbulence intensity varied slightly in the condition where Reynolds number was increased to 25,000; These values are reported later alongside the turbine performance metrics.

The difference in magnitude between the components of turbulence intensity make clear that the turbulence was anisotropic. This is to be expected; a result of the proximity of the turbine to the turbulence generators. The turbine was evidently placed in the production region for all cases, whereas true isotropic and Gaussian turbulence conditions occurred further downstream in the peak and decay regions [130]. However, for the purposes of the study, the current conditions are sufficient in providing the high desired fluctuations necessary in testing the robustness of the turbine.

The grid N3 at $1.0\,m$ distance and the grid N4 at $1.5\,m$ distance generated similar turbulence levels, of $I_x = 10.6$ and $I_x = 10.1$, respectively. In this respect, the two conditions were similar. The maximum eddy size generated by grid N4 was smaller, differentiating the two conditions, although this observation was empirical.

The turbine's performances in each of the three configurations, tested at the four turbulence levels, are provided in Tables 4.8, 4.9, and 4.10. There, the values presented have been normalized by the turbine's performance in ambient conditions to aid in comparison. The primary observation is that under all conditions, the turbine developed stable and periodic motions leading to acceptable performance. This confirmed that the stall flutter event was not significantly impared by flow fluctuations of this scale.

For all of the tested turbine configurations, moderate turbulence levels ($\sim 10\%$) resulted in an increase in power extraction from ambient conditions, with increases in the range of 5% to 13%. The heave amplitudes also increased. This may be the

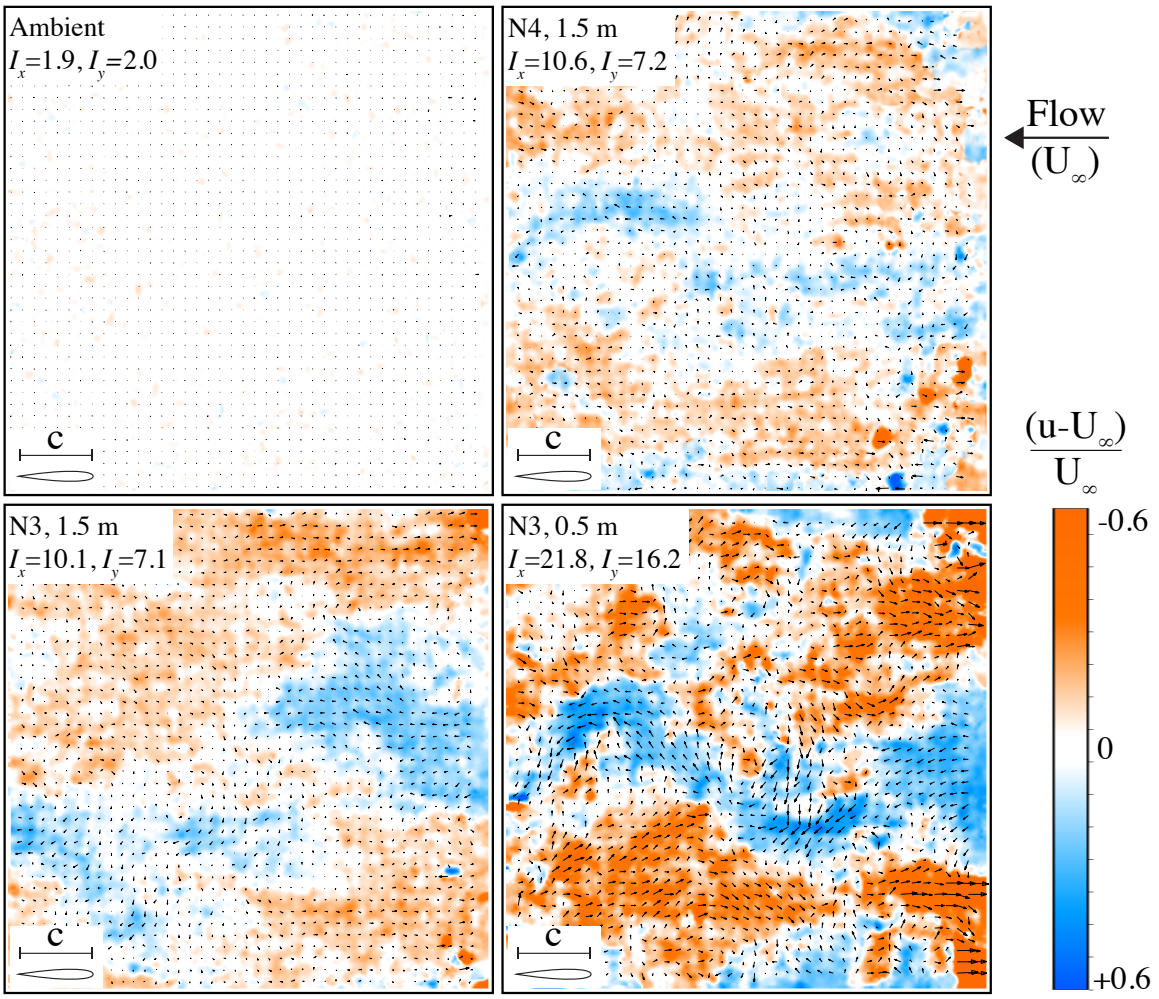

Figure 4.15: Instantaneous PIV images showing typical flow fields for each turbulent condition at Re =21,000

result of turbulence delaying the stall event by increasing momentum transfer into the boundary layer, or breaking the coherence of the primary stall vortex.

At the highest turbulence intensity, created by grid N3 at 0.5 m, the power extraction decreased for the baseline case, and the baseline case with $k^*_\theta = 0.051$. This could have multiple causes; determining which cause was primarily responsible requires further testing. One possibility is that the intermittencies in dynamic pressure in the flow could have been large enough to break down the stable lift generation driving the foil's heave motion. At this turbulence level, the largest scale eddies in the flow were proportionally larger relative to the foil chord and span than in the previous cases, suggesting why this did not occur at the other tested turbulence intensities. Alternatively, the close proximity of the turbine to the grid in this condition

resulted in the turbine being subjected to the large scale periodic vortex shedding that occurred through the central opening in the grid. This shedding is evident in the respective frame of Fig. 4.15. In the other conditions, the turbine was located sufficiently downstream so that the large vortices had decayed to a greater extent and the flow was closer to isotropic turbulence. In a peculiar manner, this same condition of grid N3 at $0.5\,m$ led to a slight increase in power extraction when the turbine was tested at $Re = 25{,}000$. The root cause of this is not known, but it is again possible that the vortices shed from the central opening of the fractal grid may have influence performance.

In any respect, it is likely that there are several factors at play, and it may be folly to strive for single governing conclusions when it comes to turbulence related phenomena. Although the fundamental mechanisms responsible for the changes have not been confirmed, this brief campaign has led to a promising outlook for the robustness of the fully-passive turbine. The turbine did not show drastic changes in operation, even at high turbulence levels. Importantly, the stall flutter events still yielded stable limit-cycle oscillations.

Table 4.8: Performance of the baseline case under varied turbulence intensities.

Case	$I_x(\%)$	C_P	H^*	θ_0	f^*	ϕ
Ambient	1.9	0.658	0.924	83.9	0.129	101
		Normalized Values				
Ambient	1.9	1.00	1.00	1.00	1.00	1.00
N4, 1m	10.6	1.09	1.01	1.01	1.03	0.98
N3, 1.5m	10.1	1.11	1.03	1.01	1.01	1.01
N3, 0.5m	21.8	0.92	0.97	1.01	0.97	1.07

4.4 Conclusions

The fully-passive turbine concept presents an opportunity to reduce the complexity of oscillating-foil turbine technologies, and its energy-extraction capabilities have been proven. Reductions in system complexity and cost would directly impact the practicality of implementing these technologies in real-world applications. The current work has been aimed at assessing the reliability of these technologies. Provided that the systems rely on unsteady fluid mechanics, and a two-way coupled fluid-structure

Table 4.9: Performance of the baseline case with $k_\theta^* = 0.051$ under varied turbulence intensities.

Case	$I_x(\%)$	C_P	H^*	θ_0	f^*	ϕ
Ambient	1.9	0.762	1.029	73.2	0.126	103
		Normalized Values				
Ambient	1.9	1.00	1.00	1.00	1.00	1.00
N4, 1m	10.6	1.13	1.05	1.03	1.01	1.01
N3, 1.5m	10.1	1.05	1.03	1.00	0.98	1.03
N3, 0.5m	21.8	0.82	0.97	0.94	0.91	1.13

Table 4.10: Performance of the baseline case at $Re = 25{,}000$ under varied turbulence intensities.

Case	$I_x(\%)$	C_P	H^*	θ_0	f^*	ϕ
Ambient	2.2	0.649	1.132	84.7	0.115	101
		Normalized Values				
Ambient	2.4	1.00	1.00	1.00	1.00	1.00
N4, 1m	10.0	1.05	0.99	1.01	1.03	0.97
N3, 1.5m	10.5	1.12	1.03	1.00	1.02	0.99
N3, 0.5m	20.3	1.03	1.03	1.00	0.98	1.01

interaction, it was questioned if the design would be inherently sensitive to variations or fluctuations in freestream flow parameters. The reliability of the design was assessed here by subjecting the foil to three distinct sets of disturbances; symmetric vortices from the wake of an oscillating-foil turbine placed upstream, boundary layer tripping in the form of distributed roughness on the surface of the foil, and moderate to high freestream turbulence levels.

When the fully-passive prototype was placed in the wake of an upstream oscillating-turbine, it was observed that the fully-passive turbine was sensitive to the frequency of the imposed vortices in the incoming flow. It developed stable motions with modest energy extraction under only a small range of upstream kinematics. The range of beneficial upstream kinematics were not those that a fully-passive turbine would create if placed upstream, limiting the likelihood that two tandem fully-passive turbines could create a useful system.

However, observations of the wake from the upstream turbine suggested that further experiments would be needed to fully assess the tandem performance. If the

downstream fully-passive device was relocated to a position outside the wake where flow was accelerated, or was moved closer to the upstream turbine where vortices were more coherent, results may be different.

The prototype responded well when it was subjected to the unstructured disturbances of high freestream turbulence intensities, and when surface roughness was applied. Both of these types of disturbances actually increased the power extraction capabilities of the turbine, with a few exceptions where power extraction decreased mildly. A unifying theory describing how these disturbances improved performance was not concluded, as the response of the system varied somewhat between test cases. However, it is suggested that both of these disturbances influenced the boundary layer dynamics on the foil, allowing stall to be delayed to a small extent, increasing instantaneous lift. In any respect, the turbine showed impressively reliable and stable operation, considering that the initial motivation for the study involved concerns for performance degradation.

Chapter 5

Conclusions

Oscillating-foil technologies provide hydrodynamically elegant solutions to both thrust generation and energy-extraction issues. Their use and study is motivated by providing clean energy solutions, either through reductions in energy input, increases in energy output, or other reductions in environmental impact.

The main objective of the thesis was to study methods of reducing system complexity to increase the practicality of oscillating-foil designs, while also providing a comprehensive literature review and outlining avenues for future work.

5.1 Summary of principle results

In the first chapter of this thesis, an overview of the distinguishing kinematics of oscillating-foils in both propulsion and energy-extraction regimes was presented. The motivation to reduce system complexity was outlined. The main body of the thesis consisted of three scientific papers, each representing a chapter from 2 through 4, focusing on a specific topic.

The first paper experimentally investigated the influence of foil flexibility on the propulsive performance of a generic oscillating-foil system. Multiple foils of the same shape but varied construction allowed explicit comparison of the effect of stiffness and inertia, and an array of pitch and heave kinematics was explored. The work expanded upon a previous experimental campaign, now including quantitative flow imaging and a larger parametric space. The angle of the trailing edge of the foil was observed to be the most influential parameter on thrust generation, but it was somewhat insensitive to whether this was achieved by passive foil flexibility, or active pitch control. The

results provide a promising avenue for further research and application.

A basic concern about the fidelity of experiment-scale oscillating-foil turbines was addressed in the second paper. The motivation was drawn from previous observations, both numerical and experimental, that distinct differences in energy-extraction capability and the dominant flow structures that develop will occur when the turbines operate in laminar versus turbulent conditions. It was therefore uncertain if transitional-scale experiments, constrained in size by physical limitations, were representative of the desired high Reynolds number conditions for full-scale turbines. Despite what the quasi-static assumption from the first section of the paper would have predicted, the oscillating-foil turbine at Reynolds numbers 20,000 to 35,000 had similar performance to previous numerical works at a Reynolds number of 500,000. Surface roughness elements, positioned at the position of maximum foil thickness, improved this similarity but only by a few percent. Application of established blockage corrections was appropriate in many cases, but showed some inaccuracies in off-design conditions. Reiterating that discrepancies occurred only for cases with reduced performance, this is not necessarily seen as an issue. In summary, the results provided a reassuring assessment on the fidelity of common experimental campaigns.

Fully-passive turbines, where no active control system is present, and the degrees-of-freedom of the system are not mechanically constrained, provide a promising opportunity to reduce an oscillating-foil turbine's system complexity and cost. The third paper in this thesis addressed the issue of the reliability of the fully-passive concept, by subjecting it to sets of practical and foreseeable disturbances. Specifically, the energy-extraction capabilities and stability of a fully-passive turbine prototype was assessed in the wake of an upstream turbine, in a flow with high freestream turbulence levels, and when roughness elements were applied to the wing's surface. The turbine showed robust operation in the latter two conditions, where it was observed that moderate turbulence and roughness actually benefited the energy-extraction capabilities of the turbine. When operating in the wake of an upstream turbine, the prototype was sensitive to the frequency of the vortices in the wake. A narrow band of frequencies resulted in good energy-extraction and stable oscillations, but performance degraded elsewhere. This was partially attributed to the strong momentum deficit that existed in the wake, where future work could test other multiple-foil arrangements that would position the downstream turbine outside of the main wake.

5.2 Future work

Oscillating-foil technologies are showing rapid advancement thanks to the many research groups actively developing the field. Following the natural progression of the current work, the following may be said about future paths for novel research that will contribute to this developing state of the art.

With respect to foil propulsion, the current work promotes the concept that foil flexibility can be beneficial in not only eliminating the need for an active pitch mechanism, but generally improving the propulsive performance. It would further be beneficial to develop a general relation between the anticipated fluid loading on the foil surface and the structural stiffness of the foil, to be able to design an optimal structure a priori. It would also be beneficial to find a means to generalize the current results, either theoretically or by an expanded data set.

The area of oscillating-foil turbines has exciting room for further research, both with regards to pure fluid mechanics and to applied engineering. In terms of practical implementation, some life-cycle analysis should be performed. Estimates for power extraction throughout a tidal cycle, for example, would be useful in determining an oscillating-foil turbine's overall energy-extraction capability. While it has been recited in literature that these designs can work at lower speeds than conventional rotary designs, this should be confirmed with the current knowledge of optimal turbine kinematics. In an effort to design a practical, environmentally friendly turbine, some other considerations would also need to be studied. For example: will significant sediment erosion occur downstream of a turbine mounted on the river floor or sea floor? Will shallow turbines be susceptible to noisy and damaging cavitation? Will marine growth alter performance? For this latest remark, it is possible that some marine growth could actually be beneficial, acting as surface roughness and delaying stall to higher angles, similar to the increases in performance seen in Section 4.3.3. Of course, such a remark is, at this point, in speculation.

The fully-passive turbine is a promising concept. Its simplicity and reliability may outweigh its modest reduction in power output compared to constrained systems, if the reduction in cost is justified or if net system efficiency increases overall. The cost of the design could be further reduced by replacing the wing with a simple flat plate. This concept was originally proposed and explored by several authors on constrained motion systems, but following the realization that energy-extraction was maximized when stall was suppressed (which is not possible with flat plates), the idea has not

been tested in recent years. That said, the fully-passive turbine relies on stall as the mechanism to produce flutter, making the use of a flat plate feasible. A fully-passive design with a simple elastically mounted flat plate provides a promising design possibility for low-cost applications.

The fact that stall is a requirement for stall-flutter based turbines directly limits the turbine's energy extraction. This follows from the understanding that higher extraction efficiencies may occur when flow remains attached to the foil throughout a cycle and stall is avoided. This motivates an effort to revisit fully-passive turbines with motions driven by classical flutter; a type of flutter that does not necessarily rely on stall, but rather uses a well defined structural coupling to produce the cyclic motion. This could lead to higher performances. It would be recommended that this be approached first theoretically, then numerically, and lastly, with an experimental proof-of-concept and reliability study.

The final recommendation for future work regards developing a unifying non-dimensional space; not a simple task. It has been commonplace to present oscillating-foil turbine performance in parametric maps, where the reduced frequency, heave amplitude, and pitch amplitude represent the defining parameters, upon which the performance metrics are plotted. These parameters are physical representations of the kinematics of the system, but only indirectly describe the direct interaction of the foil and the flow. It may be argued that using the effective angle of attack, and the rate of change of effective angle of attack, would provide a more unifying parametric set. Ideally, one where general limits of various stall regimes could be drawn from fundamental flow interactions. A difficulty with this is that the effective angle of attack may not necessarily be sinusoidal over a cycle, so it could be difficult to include this variation. In fact, if the pitch and heave motions are truly sinusoidal, the effective angle of attack will not be. Related to this, pitch scheduling, the approach of prescribing the effective angle of attack throughout a cycle rather than the pitch and heave motions themselves, may result in higher efficiencies and should be studied in depth.

Bibliography

[1] P. R. Bandyopadhyay, "Swimming and flying in naturethe route toward applications: The freeman scholar lecture," *Journal of Fluids Engineering*, vol. 131, no. 3, p. 031801, 2009.

[2] M. S. Triantafyllou and G. S. Triantafyllou, "An efficient swimming machine," *Scientific american*, vol. 272, no. 3, pp. 64–70, 1995.

[3] J. O. Dabiri, "Optimal vortex formation as a unifying principle in biological propulsion," *Annual review of fluid mechanics*, vol. 41, pp. 17–33, 2009.

[4] W. Shyy, H. Aono, C.-k. Kang, and H. Liu, *An introduction to flapping wing aerodynamics*, vol. 37. Cambridge University Press, 2013.

[5] M. Sfakiotakis, D. M. Lane, and J. B. C. Davies, "Review of fish swimming modes for aquatic locomotion," *IEEE Journal of oceanic engineering*, vol. 24, no. 2, pp. 237–252, 1999.

[6] E. De Langre, "Effects of wind on plants," *Annu. Rev. Fluid Mech.*, vol. 40, pp. 141–168, 2008.

[7] M. W. Kehoe, "A historical overview of flight flutter testing," 1995.

[8] Y. C. Fung, *An introduction to the theory of aeroelasticity*. Courier Dover Publications, 2008.

[9] I. E. Garrick, "Propulsion of a flapping and oscillating airfoil," 1937.

[10] T. Theodorsen, "General theory of aerodynamic instability and the mechanism of flutter," *NACA Thecnical Report*, no. 496, 1935.

[11] T. Kinsey and G. Dumas, "Parametric study of an oscillating airfoil in a power-extraction regime," *AIAA journal*, vol. 46, no. 6, pp. 1318–1330, 2008.

[12] K. D. Jones and M. F. Platzer, "Design and development considerations for biologically inspired flapping-wing micro air vehicles," in *Animal Locomotion*, pp. 237–248, Springer, 2010.

[13] T. C. Corke and F. O. Thomas, "Dynamic stall in pitching airfoils: aerodynamic damping and compressibility effects," *Annual Review of Fluid Mechanics*, vol. 47, pp. 479–505, 2015.

[14] J. J. Rohr and F. E. Fish, "Strouhal numbers and optimization of swimming by odontocete cetaceans," *Journal of Experimental Biology*, vol. 207, no. 10, pp. 1633–1642, 2004.

[15] M. Saadat, F. E. Fish, A. Domel, V. Di Santo, G. Lauder, and H. Haj-Hariri, "On the rules for aquatic locomotion," *Physical Review Fluids*, vol. 2, no. 8, p. 083102, 2017.

[16] A. J. Richards, *Tuning the passive structural response of an oscillating-foil propulsion mechanism for improved thrust generation and efficiency.* PhD thesis, University of Victoria, 2013.

[17] B. J. Simpson, *Experimental studies of flapping foils for energy extraction.* PhD thesis, Massachusetts Institute of Technology, 2009.

[18] T. Kinsey and G. Dumas, "Optimal operating parameters for an oscillating foil turbine at reynolds number 500,000," *AIAA Journal*, vol. 52, no. 9, pp. 1885–1895, 2014.

[19] T. Kinsey, G. Dumas, G. Lalande, J. Ruel, A. Mehut, P. Viarouge, J. Lemay, and Y. Jean, "Prototype testing of a hydrokinetic turbine based on oscillating hydrofoils," *Renewable Energy*, vol. 36, no. 6, pp. 1710–1718, 2011.

[20] M. Boudreau, G. Dumas, M. Rahimpour, and P. Oshkai, "Experimental investigation of the energy extraction by a fully-passive flapping-foil hydrokinetic turbine prototype." to be published in the Journal of Fluids and Structures.

[21] J. Young, J. C. Lai, and M. F. Platzer, "A review of progress and challenges in flapping foil power generation," *Progress in Aerospace Sciences*, vol. 67, pp. 2–28, 2014.

[22] W. Shyy, H. Aono, S. K. Chimakurthi, P. Trizila, C.-K. Kang, C. E. Cesnik, and H. Liu, "Recent progress in flapping wing aerodynamics and aeroelasticity," *Progress in Aerospace Sciences*, vol. 46, no. 7, pp. 284–327, 2010.

[23] F. Fish and G. Lauder, "Passive and active flow control by swimming fishes and mammals," *Annu. Rev. Fluid Mech.*, vol. 38, pp. 193–224, 2006.

[24] G. Iosilevskii and D. Weihs, "Speed limits on swimming of fishes and cetaceans," *Journal of The Royal Society Interface*, vol. 5, no. 20, pp. 329–338, 2008.

[25] F. E. Fish, "Biomechanical perspective on the origin of cetacean flukes," in *The emergence of whales*, pp. 303–324, Springer, 1998.

[26] J. Katz and D. Weihs, "Hydrodynamic propulsion by large amplitude oscillation of an airfoil with chordwise flexibility," *Journal of Fluid Mechanics*, vol. 88, no. 3, pp. 485–497, 1978.

[27] P. R. Bandyopadhyay, "Maneuvering hydrodynamics of fish and small underwater vehicles," *Integrative and Comparative Biology*, vol. 42, no. 1, pp. 102–117, 2002.

[28] F. E. Fish, L. E. Howle, and M. M. Murray, "Hydrodynamic flow control in marine mammals," *Integrative and Comparative Biology*, vol. 48, no. 6, pp. 788–800, 2008.

[29] M. F. Platzer, K. D. Jones, J. Young, and J. S. Lai, "Flapping wing aerodynamics: progress and challenges," *AIAA journal*, vol. 46, no. 9, pp. 2136–2149, 2008.

[30] D. Barrett, M. Grosenbaugh, and M. Triantafyllou, "The optimal control of a flexible hull robotic undersea vehicle propelled by an oscillating foil," in *Autonomous Underwater Vehicle Technology, 1996. AUV'96., Proceedings of the 1996 Symposium on*, pp. 1–9, IEEE, 1996.

[31] G. S. Triantafyllou, M. Triantafyllou, and M. Grosenbaugh, "Optimal thrust development in oscillating foils with application to fish propulsion," *Journal of Fluids and Structures*, vol. 7, no. 2, pp. 205–224, 1993.

[32] F. E. Fish and J. Rohr, "Review of dolphin hydrodynamics and swimming performance," tech. rep., Space and naval warfare systems command, San Diego CA, 1999.

[33] J. C. Liao, D. N. Beal, G. V. Lauder, and M. S. Triantafyllou, "Fish exploiting vortices decrease muscle activity," *Science*, vol. 302, no. 5650, pp. 1566–1569, 2003.

[34] F. E. Fish, P. W. Weber, M. M. Murray, and L. E. Howle, "The tubercles on humpback whales' flippers: application of bio-inspired technology," 2011.

[35] M. Lighthill, "Note on the swimming of slender fish," *Journal of fluid Mechanics*, vol. 9, no. 2, pp. 305–317, 1960.

[36] T. Y.-T. Wu, "Swimming of a waving plate," *Journal of Fluid Mechanics*, vol. 10, no. 3, pp. 321–344, 1961.

[37] J. H. McMasters, "The flight of the bumblebee and related myths of entomological engineering: bees help bridge the gap between science and engineering," *American Scientist*, vol. 77, no. 2, pp. 164–169, 1989.

[38] W. Shyy and H. Liu, "Flapping wings and aerodynamic lift: the role of leading-edge vortices," *AIAA journal*, vol. 45, no. 12, pp. 2817–2819, 2007.

[39] P. Prempraneerach, F. Hover, and M. S. Triantafyllou, "The effect of chordwise flexibility on the thrust and efficiency of a flapping foil," in *Proc. 13th Int. Symp. on Unmanned Untethered Submersible Technology: special session on bioengineering research related to autonomous underwater vehicles, New Hampshire*, vol. 152, pp. 152–170, 2003.

[40] J.-M. Miao and M.-H. Ho, "Effect of flexure on aerodynamic propulsive efficiency of flapping flexible airfoil," *Journal of Fluids and Structures*, vol. 22, no. 3, pp. 401–419, 2006.

[41] H. Dai, H. Luo, P. J. F. de Sousa, and J. F. Doyle, "Thrust performance of a flexible low-aspect-ratio pitching plate," *Physics of Fluids*, vol. 24, no. 10, p. 101903, 2012.

[42] B. C. Egan, C. J. Brownell, and M. M. Murray, "Experimental assessment of performance characteristics for pitching flexible propulsors," *Journal of Fluids and Structures*, vol. 67, pp. 22–33, 2016.

[43] P. Liu and N. Bose, "Propulsive performance from oscillating propulsors with spanwise flexibility," in *Proceedings of the Royal Society of London A: Mathematical, Physical and Engineering Sciences*, vol. 453, pp. 1763–1770, The Royal Society, 1997.

[44] Y.-S. Lin, Y.-T. Tzeng, C.-T. Hsieh, C. C. Chang, and C.-C. Chu, "A mechanism of thrust enhancement on a heaving plate due to flexibility at moderately low reynolds numbers," *Journal of Fluids and Structures*, vol. 76, pp. 573–591, 2018.

[45] H. Park, Y.-J. Park, B. Lee, K.-J. Cho, and H. Choi, "Vortical structures around a flexible oscillating panel for maximum thrust in a quiescent fluid," *Journal of Fluids and Structures*, vol. 67, pp. 241–260, 2016.

[46] S. Vogel, *Life in moving fluids: the physical biology of flow*. Princeton University Press, 1996.

[47] Q. Zhu, "Numerical simulation of a flapping foil with chordwise or spanwise flexibility," *AIAA journal*, vol. 45, no. 10, pp. 2448–2457, 2007.

[48] B. Yin and H. Luo, "Effect of wing inertia on hovering performance of flexible flapping wings," *Physics of Fluids*, vol. 22, no. 11, p. 111902, 2010.

[49] T. L. Daniel and S. A. Combes, "Flexible wings and fins: bending by inertial or fluid-dynamic forces?," *Integrative and Comparative Biology*, vol. 42, no. 5, pp. 1044–1049, 2002.

[50] M. Olivier and G. Dumas, "A parametric investigation of the propulsion of 2d chordwise-flexible flapping wings at low reynolds number using numerical simulations," *Journal of Fluids and Structures*, vol. 63, pp. 210–237, 2016.

[51] A. J. Richards and P. Oshkai, "Effect of the stiffness, inertia and oscillation kinematics on the thrust generation and efficiency of an oscillating-foil propulsion system," *Journal of Fluids and Structures*, vol. 57, pp. 357–374, 2015.

[52] E. Gauthier, T. Kinsey, and G. Dumas, "Impact of blockage on the hydrodynamic performance of oscillating-foils hydrokinetic turbines," *Journal of Fluids Engineering*, vol. 138, no. 9, p. 091103, 2016.

[53] M. Barnsley and J. Wellicome, "Final report on the 2nd phase of development and testing of a horizontal axis wind turbine test rig for the investigation of stall regulation aerodynamics. carried out under etsu agreement e," *Carried Out Under ETSU Agreement No. E. A*, vol. 5, 1990.

[54] F. Hover, Ø. Haugsdal, and M. Triantafyllou, "Effect of angle of attack profiles in flapping foil propulsion," *Journal of Fluids and Structures*, vol. 19, no. 1, pp. 37–47, 2004.

[55] M. Raffel, C. E. Willert, F. Scarano, C. J. Kähler, S. T. Wereley, and J. Kompenhans, *Particle image velocimetry: a practical guide*. Springer, 2018.

[56] Q. Xiao and Q. Zhu, "A review on flow energy harvesters based on flapping foils," *Journal of fluids and structures*, vol. 46, pp. 174–191, 2014.

[57] A. Conlisk, "Modern helicopter rotor aerodynamics," *Progress in aerospace sciences*, vol. 37, no. 5, pp. 419–476, 2001.

[58] W. McKinney and J. DeLaurier, "Wingmill: an oscillating-wing windmill," *Journal of energy*, vol. 5, no. 2, pp. 109–115, 1981.

[59] Z. Peng and Q. Zhu, "Energy harvesting through flow-induced oscillations of a foil," *Physics of fluids*, vol. 21, no. 12, p. 123602, 2009.

[60] K. Lindsey, *A feasibility study of oscillating-wing power generators*. PhD thesis, Monterey, California. Naval Postgraduate School, 2002.

[61] K. D. Jones, K. Lindsey, and M. Platzer, "An investigation of the fluid-structure interaction in an oscillating-wing micro-hydropower generator," 2003.

[62] M. S. Campobasso, A. Piskopakis, J. Drofelnik, and A. Jackson, "Turbulent navier–stokes analysis of an oscillating wing in a power-extraction regime using the shear stress transport turbulence model," *Computers & Fluids*, vol. 88, pp. 136–155, 2013.

[63] M. S. Campobasso and J. Drofelnik, "Compressible navier–stokes analysis of an oscillating wing in a power-extraction regime using efficient low-speed preconditioning," *Computers & Fluids*, vol. 67, pp. 26–40, 2012.

[64] T. Kinsey and G. Dumas, "Optimal tandem configuration for oscillating-foils hydrokinetic turbine," *Journal of fluids engineering*, vol. 134, no. 3, p. 031103, 2012.

[65] T. Kinsey and G. Dumas, "Computational fluid dynamics analysis of a hydrokinetic turbine based on oscillating hydrofoils," *Journal of fluids engineering*, vol. 134, no. 2, p. 021104, 2012.

[66] D. Poirel, Y. Harris, and A. Benaissa, "Self-sustained aeroelastic oscillations of a naca0012 airfoil at low-to-moderate reynolds numbers," *Journal of Fluids and Structures*, vol. 24, no. 5, pp. 700–719, 2008.

[67] H. Abiru and A. Yoshitake, "Study on a flapping wing hydroelectric power generation system," *Journal of Environment and Engineering*, vol. 6, no. 1, pp. 178–186, 2011.

[68] P. E. Sitorus, T. Q. Le, J. H. Ko, T. Q. Truong, and H. C. Park, "Design, implementation, and power estimation of a lab-scale flapping-type turbine," *Journal of Marine Science and Technology*, vol. 21, no. 1, pp. 115–128, 2016.

[69] B. J. Simpson, F. S. Hover, M. S. Triantafyllou, *et al.*, "Experiments in direct energy extraction through flapping foils," in *The Eighteenth International Offshore and Polar Engineering Conference*, International Society of Offshore and Polar Engineers, 2008.

[70] K. Lu, Y. Xie, D. Zhang, and G. Xie, "Systematic investigation of the flow evolution and energy extraction performance of a flapping-airfoil power generator," *Energy*, vol. 89, pp. 138–147, 2015.

[71] I. Fenercioglu, B. Zaloglu, J. Young, M. Ashraf, J. Lai, and M. Platzer, "Flow structures around an oscillating-wing power generator," *AIAA Journal*, vol. 53, no. 11, pp. 3316–3326, 2015.

[72] F. F. Siala, A. D. Totpal, and J. A. Liburdy, "Characterization of vortex dynamics in the near wake of an oscillating flexible foil," *Journal of Fluids Engineering*, vol. 138, no. 10, p. 101202, 2016.

[73] D. Kim, B. Strom, S. Mandre, and K. Breuer, "Energy harvesting performance and flow structure of an oscillating hydrofoil with finite span," *Journal of Fluids and Structures*, vol. 70, pp. 314–326, 2017.

[74] L. Ericsson, "Moving wall effects in unsteady flow," *Journal of Aircraft*, vol. 25, no. 11, pp. 977–990, 1988.

[75] W. Swanson, "The magnus effect: A summary of investigations to date," *Journal of Basic Engineering*, vol. 83, no. 3, pp. 461–470, 1961.

[76] W. J. McCroskey, "Unsteady airfoils," *Annual review of fluid mechanics*, vol. 14, no. 1, pp. 285–311, 1982.

[77] K. McAlister, S. Pucci, W. McCroskey, and L. Carr, "An experimental study of dynamic stall on advanced airfoil section. volume 2: Pressure and force data," 1982.

[78] P. O. Bowles, *Wind tunnel experiments on the effect of compressibility on the attributes of dynamic stall*. University of Notre Dame, 2012.

[79] L. W. Carr and M. Chandrasekhara, "Compressibility effects on dynamic stall," *Progress in Aerospace Sciences*, vol. 32, no. 6, pp. 523–573, 1996.

[80] S. Heathcote and I. Gursul, "Flexible flapping airfoil propulsion at low reynolds numbers," *AIAA journal*, vol. 45, no. 5, pp. 1066–1079, 2007.

[81] A. L. Braslow and E. C. Knox, "Simplified method for determination of critical height of distributed roughness particles for boundary-layer transition at mach numbers from 0 to 5," 1958.

[82] L. S. Davis, "7.0 user manual," 2004.

[83] İ. Fenercioğlu, *Experimental investigation of flow structures around an oscillating airfoil in steady current*. PhD thesis, 2010.

[84] T. Kinsey and G. Dumas, "Three-dimensional effects on an oscillating-foil hydrokinetic turbine," *Journal of fluids engineering*, vol. 134, no. 7, p. 071105, 2012.

[85] M. Drela, "Xfoil: An analysis and design system for low reynolds number airfoils," in *Low Reynolds number aerodynamics*, pp. 1–12, Springer, 1989.

[86] M. Drela and M. B. Giles, "Viscous-inviscid analysis of transonic and low reynolds number airfoils," *AIAA journal*, vol. 25, no. 10, pp. 1347–1355, 1987.

[87] J. Tank, L. Smith, and G. Spedding, "On the possibility (or lack thereof) of agreement between experiment and computation of flows over wings at moderate reynolds number," *Interface focus*, vol. 7, no. 1, p. 20160076, 2017.

[88] T. J. Mueller and S. M. Batil, "Experimental studies of separation on a two-dimensional airfoil at low reynolds numbers," *AIAA journal*, vol. 20, no. 4, pp. 457–463, 1982.

[89] W. McCroskey, "A critical assessment of wind tunnel results for the naca 0012 airfoil," tech. rep., NATIONAL AERONAUTICS AND SPACE ADMINISTRATION MOFFETT FIELD CA AMES RESEARCHCENTER, 1987.

[90] R. Adrian, K. Christensen, and Z.-C. Liu, "Analysis and interpretation of instantaneous turbulent velocity fields," *Experiments in fluids*, vol. 29, no. 3, pp. 275–290, 2000.

[91] J. Jeong and F. Hussain, "On the identification of a vortex," *Journal of fluid mechanics*, vol. 285, pp. 69–94, 1995.

[92] M. Z. Jacobson, "Review of solutions to global warming, air pollution, and energy security," *Energy & Environmental Science*, vol. 2, no. 2, pp. 148–173, 2009.

[93] M. Ragheb and A. M. Ragheb, "Wind turbines theory-the betz equation and optimal rotor tip speed ratio," in *Fundamental and advanced topics in wind power*, InTech, 2011.

[94] Q. Xiao, W. Liao, S. Yang, and Y. Peng, "How motion trajectory affects energy extraction performance of a biomimic energy generator with an oscillating foil?," *Renewable Energy*, vol. 37, no. 1, pp. 61–75, 2012.

[95] T. E. B. Limited, "Stingray tidal energy device - phase 3," no. WO2012040834A1, 2005.

[96] J. Deng, L. Teng, D. Pan, and X. Shao, "Inertial effects of the semi-passive flapping foil on its energy extraction efficiency," *Physics of Fluids*, vol. 27, no. 5, p. 053103, 2015.

[97] M. D. Griffith, D. L. Jacono, J. Sheridan, and J. S. Leontini, "Passive heaving of elliptical cylinders with active pitching–from cylinders towards flapping foils," *Journal of Fluids and Structures*, vol. 67, pp. 124–141, 2016.

[98] E. Shimizu, K. Isogai, and S. Obayashi, "Multiobjective design study of a flapping wing power generator," *Journal of Fluids Engineering*, vol. 130, no. 2, p. 021104, 2008.

[99] L. Teng, J. Deng, D. Pan, and X. Shao, "Effects of non-sinusoidal pitching motion on energy extraction performance of a semi-active flapping foil," *Renewable Energy*, vol. 85, pp. 810–818, 2016.

[100] J. Wu, Y. Qiu, C. Shu, and N. Zhao, "Pitching-motion-activated flapping foil near solid walls for power extraction: A numerical investigation," *Physics of Fluids*, vol. 26, no. 8, p. 083601, 2014.

[101] J. Wu, Y. Chen, and N. Zhao, "Role of induced vortex interaction in a semi-active flapping foil based energy harvester," *Physics of Fluids*, vol. 27, no. 9, p. 093601, 2015.

[102] J. Zhan, B. Xu, J. Wu, and J. Wu, "Power extraction performance of a semi-activated flapping foil in gusty flow," *Journal of Bionic Engineering*, vol. 14, no. 1, pp. 99–110, 2017.

[103] Y. Chen, J. Nan, and J. Wu, "Wake effect on a semi-active flapping foil based energy harvester by a rotating foil," *Computers & Fluids*, vol. 160, pp. 51–63, 2018.

[104] Q. Zhu, "Optimal frequency for flow energy harvesting of a flapping foil," *Journal of fluid mechanics*, vol. 675, pp. 495–517, 2011.

[105] M. Boudreau, K. Gunther, and G. Dumas, "Investigation of the energy-extraction regime of a novel semi-passive flapping-foil turbine concept with a prescribed heaving motion and a passive pitching motion." In review.

[106] D. Poirel and W. Yuan, "Aerodynamics of laminar separation flutter at a transitional reynolds number," *Journal of Fluids and Structures*, vol. 26, no. 7-8, pp. 1174–1194, 2010.

[107] J.-C. Veilleux and G. Dumas, "Numerical optimization of a fully-passive flapping-airfoil turbine," *Journal of Fluids and Structures*, vol. 70, pp. 102–130, 2017.

[108] P. Šidlof, V. Vlček, and M. Štěpán, "Experimental investigation of flow-induced vibration of a pitch–plunge naca 0015 airfoil under deep dynamic stall," *Journal of Fluids and Structures*, vol. 67, pp. 48–59, 2016.

[109] X. Amandolese, S. Michelin, and M. Choquel, "Low speed flutter and limit cycle oscillations of a two-degree-of-freedom flat plate in a wind tunnel," *Journal of Fluids and Structures*, vol. 43, pp. 244–255, 2013.

[110] N. A. Razak, T. Andrianne, and G. Dimitriadis, "Flutter and stall flutter of a rectangular wing in a wind tunnel," *AIAA journal*, vol. 49, no. 10, pp. 2258–2271, 2011.

[111] *Low Speed Flutter and Post-Critical Behaviour of Flat Plate and NACA0018 Section Models in a Wind Tunnel*, 2016.

[112] Y. Yu, X. Amandolese, C. Fan, and Y. Liu, "Experimental study and modelling of unsteady aerodynamic forces and moment on flat plate in high amplitude pitch ramp motion," *Journal of Fluid Mechanics*, vol. 846, pp. 82–120, 2018.

[113] T. O'Neil and T. W. Strganac, "Aeroelastic response of a rigid wing supported by nonlinear springs," *Journal of Aircraft*, vol. 35, no. 4, pp. 616–622, 1998.

[114] J. Song, T. Kim, and S. J. Song, "Experimental determination of unsteady aerodynamic coefficients and flutter behavior of a rigid wing," *Journal of Fluids and Structures*, vol. 29, pp. 50–61, 2012.

[115] J.-C. Veilleux, "Numerical study of self-sustained pitch-heave oscillations of an elastically supported airfoil," Master's thesis, Dept. of Mechanical Engineering, Laval University, Quebec, Canada, 2014.

[116] E. H. Dowell, H. C. Curtiss, R. H. Scanlan, and F. Sisto, *A modern course in aeroelasticity*, vol. 3. Springer, 1989.

[117] G. Dimitriadis and J. Li, "Bifurcation behavior of airfoil undergoing stall flutter oscillations in low-speed wind tunnel," *AIAA journal*, vol. 47, no. 11, pp. 2577–2596, 2009.

[118] B. Feeny and J. Liang, "A decrement method for the simultaneous estimation of coulomb and viscous friction," *Journal of Sound and Vibration*, vol. 195, no. 1, pp. 149–154, 1996.

[119] H. Abiru and A. Yoshitake, "Experimental study on a cascade flapping wing hydroelectric power generator," in *ASME 2011 Power Conference collocated with JSME ICOPE 2011*, pp. 537–543, American Society of Mechanical Engineers, 2011.

[120] L. Pigolotti, C. Mannini, G. Bartoli, and K. Thiele, "Critical and post-critical behaviour of two-degree-of-freedom flutter-based generators," *Journal of Sound and Vibration*, vol. 404, pp. 116–140, 2017.

[121] B. Newman, "Multiple actuator-disc theory for wind turbines," *Journal of Wind Engineering and Industrial Aerodynamics*, vol. 24, no. 3, pp. 215–225, 1986.

[122] A. Betz, "Schraubenpropeller mit geringstem energieverlust," *Gottinger Nachrichten*, pp. 193–213, 1919.

[123] J. O. Dabiri, "Renewable fluid dynamic energy derived from aquatic animal locomotion," *Bioinspiration & biomimetics*, vol. 2, no. 3, p. L1, 2007.

[124] S. Kline and S. Robinson, "Quasi-coherent structures in the turbulent boundary layer. i-status report on a community-wide summary of the data," *Near-wall turbulence*, pp. 200–217, 1990.

[125] M. Boudreau and G. Dumas, "Vortex dynamics in the wake of three generic types of freestream turbines," *Journal of Fluids Engineering*, vol. 140, no. 2, p. 021106, 2018.

[126] A. Mahfouth, *Fractal grid-turbulence and its effects on a performance of a model of a hydrokinetic turbine*. PhD thesis, University of Victoria, 2016.

[127] R. George, R. E. Flick, and R. Guza, "Observations of turbulence in the surf zone," *Journal of Geophysical Research: Oceans*, vol. 99, no. C1, pp. 801–810, 1994.

[128] V. Nikora and G. Smart, "Turbulence characteristics of new zealand gravel-bed rivers," *Journal of Hydraulic Engineering*, vol. 123, no. 9, pp. 764–773, 1997.

[129] W. S. Saric, H. L. Reed, and E. J. Kerschen, "Boundary-layer receptivity to freestream disturbances," *Annual review of fluid mechanics*, vol. 34, no. 1, pp. 291–319, 2002.

[130] D. Hurst and J. Vassilicos, "Scalings and decay of fractal-generated turbulence," *Physics of Fluids*, vol. 19, no. 3, p. 035103, 2007.